ЕЛЕКТРОТЕХНИЧКИ ФАКУЛТЕТ
УНИВЕРЗИТЕТА У БАЊАЛУЦИ

FACYLTY OF ELECTRICAL ENGINEERING
UNIVERSITY OF BANJALUKA

ЕЛЕКТРОНИКА
ELECTRONICS

YU ISSN 1450-5843

ГОДИШТЕ 4, БРОЈ 1, НОВЕМБАР 2000. • *VOLUME 4, NUMBER 1, NOVEMBER 2000.*

F A C U L T Y O F E L E C T R I C A L E N G I N E E R I N G
B A N J A L U K A

Address: Patre 5, 78000 Banjaluka, Republic of Srpska, Bosnia and Herzegovina
Phone: +387 51 211 408,   +387 51 212 002
Fax: +387 51 211 408

E L E C T R O N I C S

Editor: Prof. Branko L. Dokić Ph. D.
Faculty of Electrical Engineering, University of Banjaluka
Republic of Srpska
e-mail: *bdokic@etf-bl.rstel.net*

Secretary: Petar Matić, M. Sc., Faculty of Electrical Engineering
University of Banjaluka, Republic of Srpska
e-mail: *pero@etf-bl.rstel.net*

Language editor: Milena Mandić

Publisher:
Faculty of Electrical Engineering, University of Banjaluka, Republic of Srpska
Address: Patre 5, 78000 Banjaluka
Phone: +387 51 211 408,   +387 51 212 002
Fax: +387 51 211 408

Printed in:
MATIĆ GRAF, Banjaluka
Number of printed copies: 200

BIOGRAPHY OF Prof.Dr. VLADIMIR KATIĆ

Prof. Vladimir A. Katić was born in Novi Sad, Yugoslavia in 1954. He received B.Sc. degree from University of Novi Sad in 1978, and M.Sc. and Ph.D. degrees from University of Belgrade in 1981 and 1991, respectively, all in electrical engineering. From 1978 he is with Institute for Power, Electronics & Communication Engineering of Faculty of Technical Sciences, University of Novi Sad, where he is currently Associated Professor. From 1991 he is the Head of Power Electronics and Converters Group. He was Director of the Institute for Power, Electronics & Communication Engineering (1993-98) and from 1998 he is the Vice-Dean of the Faculty of Technical Sciences.

The main areas of scientific interest and research of Prof. Katić are power quality, modelling of power electronics converters and standardization in electrical engineering. He is the author of 143 scientific papers published in international and national monographs, journals or conferences proceedings. He is also reviewer, member of international programme committees and session chairmen of many international or national journals and conferences. Prof. Katić was head, main researcher or researcher of 2 international and 25 national scientific projects or studies.

He is the author of the "Power Electronics - Worked Problems" and "Power Electronics – Practicum of Laboratory Exercises", books, which are used in teaching at University of Novi Sad.

From 1994 he annually organize scientific gathering "Developments Trends - TREND" on different topics, while from 1995 biannually, together with Prof. Vučković, international symposium on Power Electronics – Ee. He is founder and president of the Power Electronics Society, which has the aim of promoting, organizing symposiums and publishing publications in area of power electronics and adjacent fields.

Prof. Katić is member of IEEE – Power Electronic Society, IEEE - Induatrial Electronics Society, IEEE - Industrial Application Society, International and National Committees of CIGRE and National Committee of CIRED.

PREFACE

Editor of the highly respected international journal »Electronics« and Dean of the Faculty of Electrical Engineering Prof. Dr. Branko Dokić honored me and at the same time, give me the responsible duty by inviting me to present, as the guest-editor, the most interesting papers from the 10th Symposium on Power Electronics – Ee´99. This is a part of very succesfull collaboration between Faculty of Electrical Engineering in Banja Luka and Faculty of Technical Sciences in Novi Sad in several fields and particulary in organiazation of two related international conferences – International Conference on Industrial Electronics - INDEL, organized by Faculty of Electrical Engineering in Banja Luka and Symposium on Power Electronics – Ee, co-organized by Faculty of Technical Sciences in Novi Sad.

10th Symposium on Power Electronics – Ee´99 (Energetska elektronika – Ee´99) was held in Novi Sad from October 14-16, 1999. It was co-organizad by Power Electronic Society sited in Novi Sad, Faculty of Technical Sciences – Institute for Power, Electronics and Communication Engineering from Novi Sad, Institute "Nikola Tesla" from Belgrade and Novi Sad Fair. It was sponsored by Ministry of Science and Technology of Republic of Serbia, Federal Ministry for Science, Development and Environment, Serbian Academy of Science and Art (SANU) and Institute of Electrical and Electronic Engineers (IEEE)-YU Section.

The preparation and organization of the event was disrupted by the unfortunate occurrences, which struck my country during 1999 – NATO bombing and agression, massive distruction, communication difficulties, external sanctions, recession etc. However, a strong will, high spirit and inside strenght of my collegues scientists, researches and engineers and friends from abroad enable succesful completition of the symposium preparation and the symposium itself.

The symposium presented 82 papers from 18 institutions of 9 countries (U.K, Germany, Holland, Canada, Romania, Czeck Republic, Macedonia, Republic of Srpska and Yugoslavia) and gethered around 200 participants. All paper are published in proceedings both in the hard copy form (591 pages) and in the electronic form (CD-ROM). CD-ROM also contains multimedial presentations of the organisators and commercial sponsors, facts about Power Electronic Society, as well as complete list of papers from all symposiums on Power Electronics (19973-1999).

Beside the symposium Annual Meeting of the Power Electronic Society was held, while parallel to the symposium the 8th International Fair »Electronics« enable the participats to meet the latest design and realizations of devices, systems, hardware and software in the field of electronics, telecommunications and computer industry.

The symposium highlighted the problems and practical or virtual solution from many fileds. Four topics are put forward: Power converters, Electrical drives, Electrical machines and Control & measurement in power engineering. The most interesting contribution discussed the areas of modeling of power electronics components, improved power electronic converters, power quality (harmonics, filters…), vector controlled induction machines, sensorless AC motor drives, new concepts of electrical machine modeling, electrical machines construction, measurement in power engineering, new control methods (neural networks and fuzzy logic for control of drives), robust control, education in power electronics etc.

The selection of papers presented in this issue is only one of several possible to represent the 10th Symposium on Power Electronics - Ee'99. I would like to emphasize my thanks to the authors who have accepted my choice for promt respons and fast adaptation of the papers to journal requirements.

I would also like to invite all readers of the »Electronics« journal to take active participation by submitting the papers or attending the next 11th Symposium on Power Electronics – Ee2001, which will be organized in NOVI SAD, YUGOSLAVIA in October/November, 2001.

Guest Editor

Prof. Dr. Vladimir Katić

ESTIMATION OF HARMONIC LEVELS IN MV SYSTEMS USING SIMULATION AND MEASUREMENT

Jürgen Schlabbach, Vladimir Katić*
University of Applied Sciences, Bielefeld, Germany
**Faculty of Engineering, Novi Sad, Yugoslavia*

Abstract: *Prior to installation of a large harmonic load it is necessary to conduct a harmonic analysis using computer simulation in order to predict possible negative effects of harmonics. The problem is that many parameters are unknown and need to be assumed. One of these are existing or background harmonic levels. Tthe paper describes the results of harmonic measurements as an indication of existing harmonic levels. A calculation for the connection of a high power converter-fed induction furnace to a MV system is presented as an example. The results indicated the specific needs for data collection, especially load data and the requirement. Furthermore it is pointed out, that calculation give only a tentative hint on the harmonic propagation, but measurement is an indispensable part for the analysis of harmonic propagation in power systems.*
Keywords: *Harmonic analysis, harmonic measurement, induction furnace, voltage quality.*

1. INTRODUCTION

Voltage quality in electrical power systems is of increasing importance due to the increased number of electronic equipment (increase of emission level) and the reduced sensitivity level of control circuits and other sensible consumers (decreasing withstand capability). Out of other phenomena, such as voltage fluctuations, voltage drops and unsymmetry, the harmonics (and interharmonics) are the most important disturbances to be regarded with respect to voltage quality [1]. Prior to connecting high-power harmonic producers, such as converter-fed induction furnaces or motor drives to the MV system, an assessment of the expected harmonic levels is necessary, which need to be carried out in accordance with the various parts of IEC 61000 [2,3]. As extensive measurements can only be carried out after commissioning of the equipment, simulation analysis by means of computer programmes are required. A major problem in this respect is the knowledge of power system data, which are normally not documented in the relevant information files of the utilities, such as inductive and capacitive part of loads, peak and low load conditions and variation of short-circuit power at the point of connection. This is due to the fact, that the problem of voltage quality nowadays mainly is regarded in LV and MV systems only, as most of the consumers, causing disturbance emissions and which are affected by the disturbances are connected to these voltage levels. The impact of significant parameters and the problems comparing measurements and calculations are analysed and explained below.

2. GENERAL

2.1 Harmonic calculation:

The simulation shall be carried out based on the method of single-phase linear harmonic analysis, which assumes linear, balanced and stationary network elements, the loads are simulated with their non-linear characteristic. Harmonics generated loads are modelled by their harmonic current with impedance in parallel. The advantage of using the linear harmonic analysis is the simple representation of the equipment, which are carried out with the same details and extend as used for load-flow and short-circuit analysis.

Harmonics are forming positive, negative or zero sequence systems depending on their order, whereas the zero sequence system is only present for harmonics which are multiples of three-times the fundamental frequency. Other harmonics are forming zero sequence parts only in those cases, where the system is not balanced. In medium voltage systems, the zero sequence system can be neglected normally for the harmonic analysis. Furthermore it should be recognized, that the interaction between the generated harmonic currents and the distorted voltage could be neglected for systems with comparatively low voltage distortion.

2.2. Measurement of harmonics:

Measurement of harmonics shall be carried out with measuring equipment according to IEC 61000-4-7 [2] for a typical load period, which is normally one week. By this, all probable load conditions, especially the reduced system load at weekends and existing (background) harmonic levels originating from other equipment, are covered by the measuring period. Harmonics up to the order of 40 shall be analysed with respect to their r.m.s. value and their phase-angle. In order to assess and evaluate measurement values a statistical analysis is necessary. The results are then compared with the compatibility levels according IEC 61000-2-4 [3], The compatibility level is defined as that level for which the disturbance will be lower for 95% of the measuring period, i.e. for 5% of the time, the disturbance level may exceed the compatibility level. It is therefore reasonable to determine the 95%-probability of the measuring values, which shall than be compared with the compatibility level.

2.3. Existing or background harmonic levels

Connection of a new large harmonic source at MV industrial bus presents a special problem and requires a careful harmonic assesment. IEC 61000 Standards [2,3], IEEE Standard 519 [4] or Australian Standard AS 2279-1991[5] issue several steps procedure, where the measurement of existing harmonic levels of the system present an important step. Such measurement shall be carried out before installation or with the of the large harmonic source out of operation.

The results obtained during harmonic measurements in Vojvodina, at medium and low voltage buses of "Elektrovojvodina", the power distribution company sited in Novi Sad, are similar to ones presented in other reports from Europe or U.S.A. [6]. Therefore they can be used for harmonic assesment or in harmonic analysis.

The results show that current harmonics are often above limits, specially in residential areas or at large industrial loads. High values of THDI, the 3[rd] and the 5[th] current harmonics indicate possibility of occurrence of some of the negative harmonics effects. Fortunately, the voltage harmonics are usualy much lower. Fig. 1 shows overall averaged spectrum values of all voltage harmonics measurement results at different loads (residential, commercial, industrial, rural etc) presented as 5% probability, mean values, 95% probability, maximum values and compared with IEEE-519 limit. It can be seen that all harmonic levels are below limits, but harmonic capacity of network is already consumed in a certain percentage. These values can be assumed as existing harmonic levels and can be used in calculations.

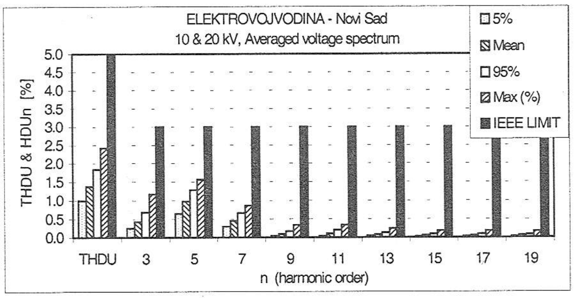

Fig. 1. *Averaged voltage spectrum recorded at 10 & 20 kV.*

3. SIMULATION EXAMPLE

3.1 Investigated power system

The 30 kV system normally operated as a meshed system, fed from the 110 kV system by two independent substations A and B, as indicated in Fig.2, are investigated. The connection of a frequency converter for the supply of an arc furnace (2.9 MVA; 12-pulse) connected to a 30 kV industrial power system (location D) was analysed. Further load is supplied from the other 30 kV substations. The 110 kV-system, consisting of cables and overhead lines, is operated in a meshed mode as well. In case of emergencies, the 30 kV system can be operated as radial system, whereas parts or whole of the system will then be fed either from substation E or C. One important parameter for the assessment of harmonics is the short-circuit power at the point of common connection (PCC). For the determination of short-circuit power the impedances at the 110 kV substations A and B and the coupling impedance between them can be calculated as:

$$X_A = \frac{1.1U_n^2}{S''_{kA}} \cdot \frac{S''_{kA}(1+V)^2 - S''_{kB}}{S''_{kA}(1+V)^2 - S''_{kB}(1+V)} \quad (1)$$

$$X_B = \frac{1.1U_n^2}{S''_{kB}} \cdot \frac{S''_{kA}(1+V)^2 - S''_{kB}}{S''_{kA}V(1+V)} \quad (2)$$

$$X_{AB} = X_B \cdot V \quad ,V = \frac{u_{B(kA)}}{110\% - u_{B(kA)}} \quad (3)$$

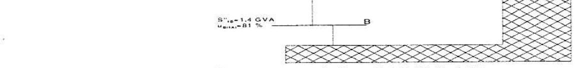

Fig.2 *Single-line diagram of the 110/30-kV-system under investigation*

For actual system parameters, the short-circuit power at the connection point D is calculated for the different operating conditions as: meshed operation - S''_k = 513 MVA, fed through C - S''_k = 322 MVA, fed through E - S''_k = 217 MVA.

3.2. Resonance

Besides the short-circuit power, the frequency dependent impedance at PCC, which is location D (Fig. 2) is necessary to know. Analysing the power system as seen from the PCC, the capacitance of the 30-kV-cables C_{30} is parallel to the reactance of the feeding system, which is the series circuit of the transformer reactance X_T parallel to the capacitance of the 110 kV cables C_{110} in series with the reactance of the 110 kV infeed XQ as indicated in Fig. 3. The impedance can be calculated as:

$$Z_{PCC}(\omega)=\frac{\omega[L_T(1-\omega^2 L_Q C_{110})+L_Q]}{1-\omega^2 C_{110} L_Q-\omega^2 C_{30}[L_T(1-\omega^2 L_Q C_{110})+L_Q]} \quad (4)$$

This analysis does not take into account the load in the 30 kV system, which is seen in parallel to the capacitance of the 30 kV cables. It should be noticed, that the reactance of the feeding transformer, the reactance of the 110 kV infeed (short-circuit power) as well as the capacitances in the 30 kV and 110 kV system change due to the different operating condition of the power system as mentioned above.

In case of meshed system operation, the parallel resonance frequencies are at 570 Hz and 810 Hz, serial frequency is at 750 Hz. In case of radial system operation (fed from substation C, cables switched-off at E), the parallel resonance frequencies are shifted to 660 Hz and 860 Hz, the serial resonance frequency remains at 750 Hz. The damping however is 2.5 times lower than for meshed system operation.

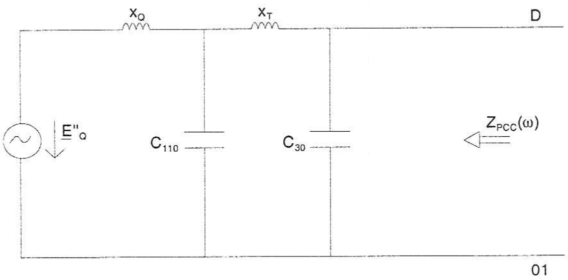

Fig.3. *Equivalent circuit diagram of 110/30-kV-system at PCC*

3.3. Assessment of measurement:

Measurements were carried out for the period of one week with different switching (operating) conditions of the 30-kV-system. The results of measurement assessment for the characteristic and non-characteristic harmonics, as Fig. 4 indicates, show that the most important difference in the level of the harmonics is while operating the power system open at location E (cables switched-off at E) as compared with the normal meshed system operation. This effect is most severe for harmonics of the order 11 until 19.

3.4. Results of calculations

Calculations have been carried out to simulate the harmonic propagation in the system and to verify the results of measuring. First simulation runs indicated comparatively poor correspondence with the measuring results. Harmonic levels were more than two times higher. Generally, higher harmonic levels were recognised for the case with cables switched-off at location E as compared with meshed system operation. The results are outlined in Table 1. The general tendency for the different operating conditions however is obtained by the calculations as well.

In order to determine the reason for the differences between measurement and calculation, a parameter study was carried varying the input parameters such as:

- short-circuit power in 110-kV-system
- load level in the system
- basic harmonic level
- power factor of the loads.

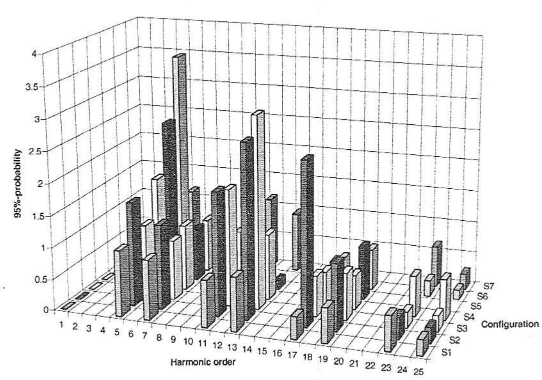

Fig.4. *95%-probability of selected harmonics for different operating conditions*

Table 1. *Comparison of calculation and measurement of harmonics for different operating conditions (95%-probability)*

	Order of meshed operation		Cables switched-off E	
Harm. order	Calc. [%]	Measur. [%]	Calc. [%]	Measur. [%]
5	1.75	1.05	2.89	1.65
7	1.69	0.95	2.93	1.35
11	1.93	0.75	4.2	1.95
13	1.49	0.85	3.73	2.75
17	1.27	0.65	3.24	2.55
19	1.12	0.55	2.41	1.5
23	0.57	0.55	0.97	0.35
25	0.43	0.25	0.71	0.25

All other system data were kept constant for the parameter study. The variation of the short-circuit power in a reasonable range (70% ... 100%) has only small influence on the harmonic level, as the short-circuit power in the 30-kV-system is mainly determined by the impedance voltage of the feeding transformers. Variation of the load between 80% and 120% of the initial value, as per Fig. 2, has only an influence on the damping, the resonant frequencies remain constant. The influence on the harmonic level is below 30% as the results for 80% and the 120% load are compared.

The basic harmonic level in the system normally is very difficult to represent in calculations, as this requires measurements without the dominant harmonic load in operation taking account well defined system load, which is hardly to be realised. The influence of the basic harmonic level is given by the amplitude and the phase angle. Table 2 indicates the results, if the basic harmonic level e.g. for 250 Hz is modified in magnitude and phase angle, causing identical resulting level in magnitude but different phase angle; the level caused by the harmonic load is assumed to be 1.75%,70o).

Table 2. *Correspondence between phase angle and magnitude of basic harmonic level BHL and resulting level RHL*

BHL		RHL	
Uh [%]	angle [deg]	Uh [%]	angle [deg]
0.73	-80.0	1.3	39.0
3.0	-119.5	1.3	-96.0
2.15	-157.0	1.3	148.0

Finally the variation of the power factor of loads in the range of +/-5% of the basic value, while the apparent power is kept constant will cause only negligible changes in the harmonic level.

4. DISCUSSION OF RESULTS

An indispensable precondition while carrying out calculation of harmonic propagation in power systems is the good knowledge of the system parameters. It is obvious that the parameters of feeding transformers as well as the parameters of cables and lines in the system are known exactly. The load in the system however is subject to changes and cannot be represented exactly in calculations. Nevertheless the variation of load, which is normal in power systems, is seen as an important part in the analysis. The only way to represent this influence is by means of an parameter study. The most important influence however is the knowledge of the basic harmonic level. The magnitude and the phase angle of the basic harmonic level need to be measured under different load conditions.

5. CONCLUSION

The comparison of measurement and simulation results indicated for some configurations only a poor correspondence. As most essential aspect for the quality of the simulation, the precise knowledge of the data of equipment in the power system were indicated. Especially data of the loads with their capacitive and inductive parts are an indispensable presupposition for a good simulation as well as the amplitude and the phase angle of the basic harmonic level. These data are difficult to obtain from utilities, in some cases it is nearly impossible to receive the data.

As overall conclusion it can be stated that thorough modellisation and simulation shall only be interpreted as tentative indicator for the expected harmonic levels in the power system due to the limited extend of data needed for the modelisation. Simulation does not release the utility and the plant owner from measurements of harmonics. These measurements must take into account different operating and load conditions. The extend of measurements may be reduced in those cases, when the behaviour of the system is well known with respect to harmonics.

6. REFERENCES

[1] R.Dugan, M.McGranaghan, H.Beaty, Electrical Power Systems Quality, McGraw-Hill, New York, 1996.

[2] IEC Standard 61000-4-7 (1991-08) – Electromagnetic compatibility (EMC), Part 4: Testing and measurement techniques, Section 7: General guide on harmonics and interharmonics measurements and instrumentation, for power supply systems and equipment connected thereto, IEC, Geneve, 1991.

[3] IEC Standard 61000-2-4 (1994-02) - *Electromagnetic compatibility (EMC), Part 2: Environment Section 4: Compatibility levels in industrial plants for low-frequency conducted disturbances*, IEC, Geneve, 1994.

[4] IEEE Standard 519-1992, *"IEEE Recommended Practices and Requirements for Harmonic Control in Electrical Power Systems"*, IEEE Industry Application Society, New York, 1992.

[5] Australian Standard AS 2279-1991, *"Disturbances in mains supply networks"*, Standards Australia, Sydney, 1991.

[6] V.Katić: "Power Quality Monitoring for Improving Utility-Customer Relations", *V DistribuTECH DA/DSM Europe Conference*, London (U.K.), Oct.1998, (published & distributed on CD-ROM).

AC/DC CONVERTER WAVEFORMS ANALYSIS USING WAVELET TRANSFORM

J. Knežević, V. Katić, D. Graovac,
Institute for Power, Electronics and Telecommunications Engineering
Faculty of Engineering - Novi Sad, Yugoslavia

Abstract: *Fourier transform is the most widely used tool for voltage and current waveform analysis. Nevertheless, it has certain drawbacks for time varying signals analysis. Therefore, a need for another analysis technique appears. The aim of this paper is to present the Fourier transform drawbacks and to introduce a novel technique, namely the Wavelet transform, which could improve accuracy of voltage and current waveshapes investigation*
.

Key words: *Fourier transform, Wavelet transform*

1. INTRODUCTION

During last decade great attention have been paid on power quality problems [5]. Some of these problems are widely caused by the power electronics converters. Size and power of power electronics devices is increasing and their share in electric power consumption is growing. Nearly ideal sinusoidal current and voltage wave-shape of precise amplitude and/or frequency at power electronic converters input is desired. However, inherent non-linearity of the power electronics devices influences the current and voltage wave-shape.

The most common tool, used up to day for wave-shape analysis, has been the Fourier Transform. [7]. It transforms a signal into fundamental and high-order harmonic components. Harmonics are sinusoidal components of the signal whose frequency is the integer multiple of the fundamental frequency. Fourier Transform, or its discrete version, which has been developed for computer application (Fast Fourier Transform), has some disadvantages, such as: aliasing, spectral leakage, picket fence effect etc. [1, 2, 3, 7] .

Fourier Transform gives exact frequency spectrum of stationary and periodical signals. However, in modern controlled drives changes in developed torque and angular velocity are often required. In the case of non-stationary and transient signals, information about appearance of certain harmonics is missing. To cover this problem, the Windowed Fourier Transform or Short-Time Fourier Transform has been developed. It decomposes the signal in smaller parts of exact length firstly, and then applies the Fourier Transform. It solves the initial problem, but several disadvantages remains: the signal is assumed periodical, stationary in the window.

In the last ten years the *Wavelet* Transform has been introduced as a new approach in signal analysis [1, 2, 3, 4]. The *wavelet* theory says that a signal can be represented by superposition of some special signals. These special signals can be *wavelets*. *Wavelets* are waves of limited duration, whose average value is zero. Apart from Fourier Transform, where a signal is represented by superposition of only one fundamental function (sine or cosine), W*avelet* Transform has unlimited number of fundamental functions.

Wavelet Transform is similar to of finite response filters, so it does not transform signal in discrete harmonics but in frequency bandwidths. But, these bandwidths cover all significant harmonics. Wavelet Transform eliminates drawbacks of Windowed Fourier Transform and is able to track fast amplitude variations of certain harmonics. This feature is enabled by its characteristics of having a narrow window for higher frequencies, and wider window for lower frequencies.

The paper will firstly represent the Fourier Transform, the Windowed Fourier Transform and the Wavelet Transform in brief, in order to present differences in signal analysis. After that, the harmonic analysis of line current of two kinds of AC/DC converters (line commutated and PWM) using Wavelet Transform will be presented.

2. FOURIER TRANSFORM

In this part, the *Fourier Transform (FT)* will be presented, as the one of the most frequently used techniques for signal analysis [7]. Fourier Transform *X(f)* of continuous signal *x(t)* is defined as::

$$X(f) = \int_{-\infty}^{\infty} x(t)e^{-j2\pi ft}dt \qquad (2.1)$$

$$x(t) = \frac{1}{2\pi}\int_{-\infty}^{\infty} X(f)e^{j2\pi ft}df \qquad (2.2)$$

Continuous function *X(f)* represent the signal *x(t)* in frequency domain, obtained by summing of infinite number of complex addend. Inverse Fourier Transform is represented by (2.2).

The periodical nature of electrical power supply as well as the use of digital signal processing lead to use of discrete Fourier transform as a convinient tool. Discrete Fourier transform *X(f)* of sampled signal *x[n]* can be obtained in following manner:

$$X[k]=\sum_{n=0}^{N-1}x[n]e^{-j\frac{2\pi kn}{N}} \qquad (2.3)$$

where $x[n]$ is sampled eqiuvalent of continuous signal $x(t)$:

$$x[n]=x(nT) \quad n=0,1,2,...,N-1 \qquad (2.4)$$

and T is the sampling period.

Inverse of discrete Fourier transform equals:

$$x[n]=\frac{1}{N}\sum_{k=0}^{N-1}X[k]e^{j\frac{2\pi kn}{N}} \qquad (2.5)$$

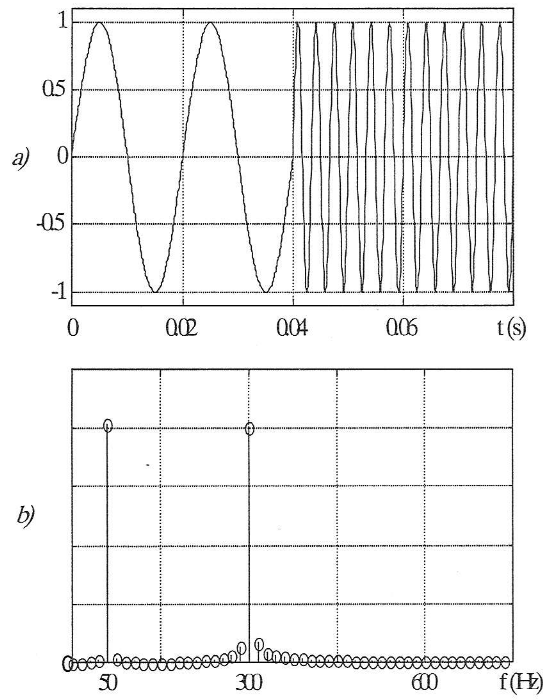

Fig. 1a and 1b – Stationary signal and its frequency spectrum

Figs. 1 and 2 represent two signals with similar frequency spectrum, but with same frequency. The first signal consists of two components of different frequencies, while the second of one frequency at the beginning and of the other at the end.

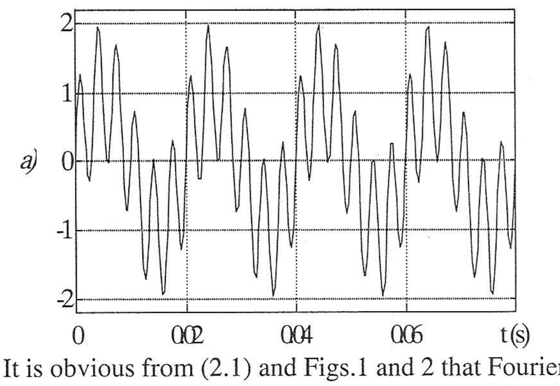

It is obvious from (2.1) and Figs.1 and 2 that Fourier Transform gives exact frequency spectrum of signal, but it does not tell where these frequencies are located in time.

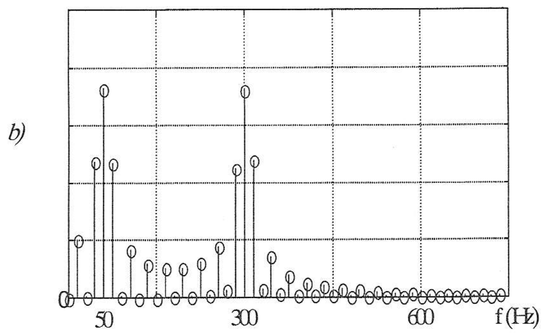

Fig. 2a and 2b – Non-stationary signal and its frequency spectrum

This problem is specialy underlined when transient states signal are to be analized. Some improvements are obtained by use of the *Windowed Fourier Transform or Short-Time Fourier Transform.*

3.WINDOWED FOURIER TRANSFORM

To overcome before mentioned Fourier transform drawbacks in transient signal analysis, it is necessary to perform certain modifications. Some improvements are obtained by use of the *Windowed Fourier Transform or Short-Time Fourier Transform.* It is similar to Fourier Transform, but input signal *w(t)* is multiplied with windowed function whose position is translated in time for τ:

$$WFT(f,\tau)=\int_{-\infty}^{\infty}x(t)w(t-\tau)e^{-j2\pi ft}dt \qquad (3.1)$$

or in the discrete version:

$$WDFT=\sum_{n}x[n]w[n-m]e^{-j\frac{2\pi kn}{N}} \qquad (3.2)$$

For every window $w_{m_0}=w[n-m_0]$, *WDFT* gives a collection of complex numbers *WDFT[k, m_0], k*=0,1,...*N-1*, whose amplitudes are equal to discrete frequencies, who are content of input signal $x[n]$. The simplest window is rectangle one, which gives a value 1 for whole width of window. There are other windows like *Hamming, Bartlett* and so on...

The example signal processed by windowed Fourier transform is presented in the next figure:

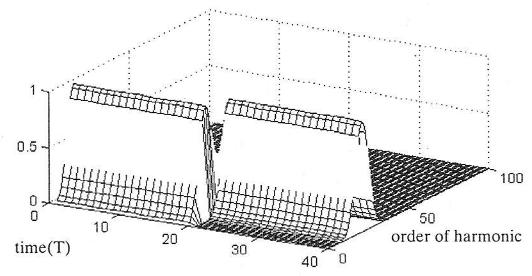

Fig. 3 – Example from fig. 2 using WFT

Inspection of the fig. 3 shows that WFT follows a frequency change during observation time. However, WFT shows unsatisfactory performace when frequency change appear inside the time window.

4. WAVELET TRANSFORM

Wavelet Transform (*WT*) of continuous signal can be :

$$WT(a,b) = \frac{1}{\sqrt{a}} \int_{-\infty}^{\infty} x(t) g(\frac{t-b}{a}) dt \qquad (4.1)$$

Similar to *WFT,* a signal $x[t]$ is transform with function $g(\frac{t-b}{a})$, analogue to $w(t-\tau)e^{-j2\pi ft}$ at *WFT.*

Function $g(t)$, which is used for signal $x(t)$ analysis, is not limited with complex exponent, as in case of Fourier Transform. Its limitations are: it must be of short duration, oscillatory, with the mean value equal to zero and fast decreasing to zero at the ends of interval. These limitations provide that integral (4.1) is final. Function $g(t)$ is called *mother wavelet.* Fig. 4 presents some of the most applied basic *wavelet* functions. The names are given according to scientists who have invented them. The number beside the name represents the number of filter coefficients.

The next characteristics of *WT,* is existence of the parameter *a,* which performs scaling in time. It does not exist at the WFT. Time bandwidth of *wavelet* $g(\frac{t-b}{a})$, which is expanding or contracts depending whether $a>1$ or $a<1$. If value of parameter is $a>1$ (or $a<1$) than g(t) is expanding (or contracting) in time, i.e. frequency is decreasing (or increasing). The Wavelet Transform begins with setting the parameter "a" at $a=1$, and then by increasing the input signal is focusing in time.

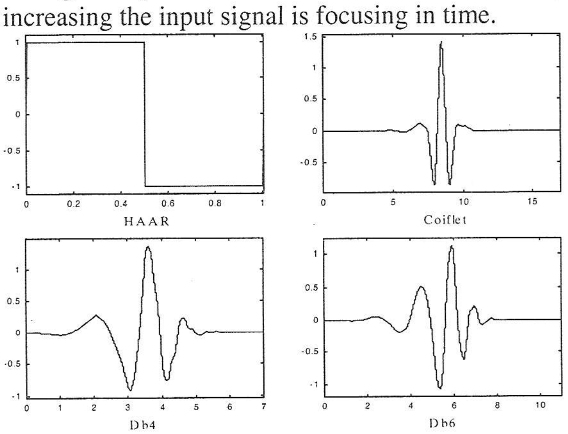

Fig. 4 - Basic wavelets

As the Fourier Transform, the *WT* has its discrete representation (*DWT*), defined as:

$$DWT[m,k] = \frac{1}{\sqrt{a_0^m}} \sum_n x[n] g\left[\frac{k - n a_0^m}{a_0^m}\right] \qquad (4.2)$$

where g[n] is basic *wavelet,* while scaling and translating parameters *a* and *b* are function of integer parameter *m.*

$$a = a_0^m \qquad (4.3)$$

$$b = n a_0^m \qquad (4.4)$$

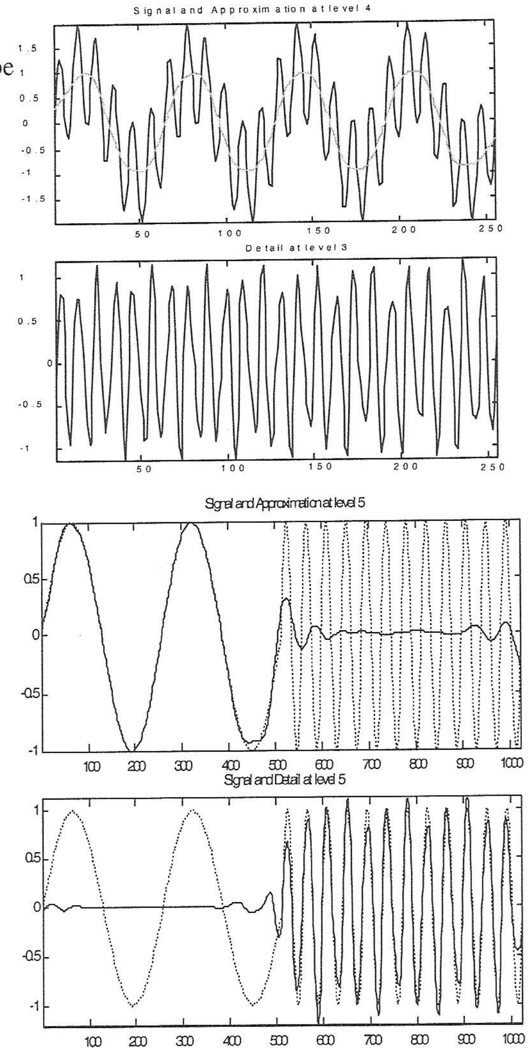

Fig. 5. – Wavelet transform examples

In contrast to Fourier Transform, which gives uniform distribution of frequencies, *wavelet* transform gives logarithm distribution, which is direct consequence of application of the above equations (Fig. 2).

Fig. 5. presents previous example to note that *WT* separates different frequency banwidths. Also, it can be seen that *WT* follows changes of signal when some of the harmonics appears and continue to be present into signal.

5. AC/DC CONVERTER CURRENT WAVEFORMS ANALYSIS

Figs. 6. and 7. show decompositions of input current waveshape of phase controlled and PWM rectifier by application of WT, as well as theirs FT. It is the case of rectifier input currents in steady state. A high harmonic distortion, specialy in case of

PWM rectifier, can be seen. Due to limited space, a transient current case is not presented.

As it was mentioned earlier, WT does not transform signal into harmonics, but it decompose it into subbandwidth i.e. scales. The width of the bandwidth depends on sampling frequency. In Fig. 6 scale a5 represents the fundamental harmonics bandwidth, scale d4 represents the 5th harmonics bandwidth and so on. Comparison of this signal with its FT (Fig. 6 – down) shows that amplitudes of harmonics are the same.

Fig. 7 shows that sampling frequency must be higher due to higher frequency of carier signal. Therefore decomposition can be performed in more bandwidths or scales.

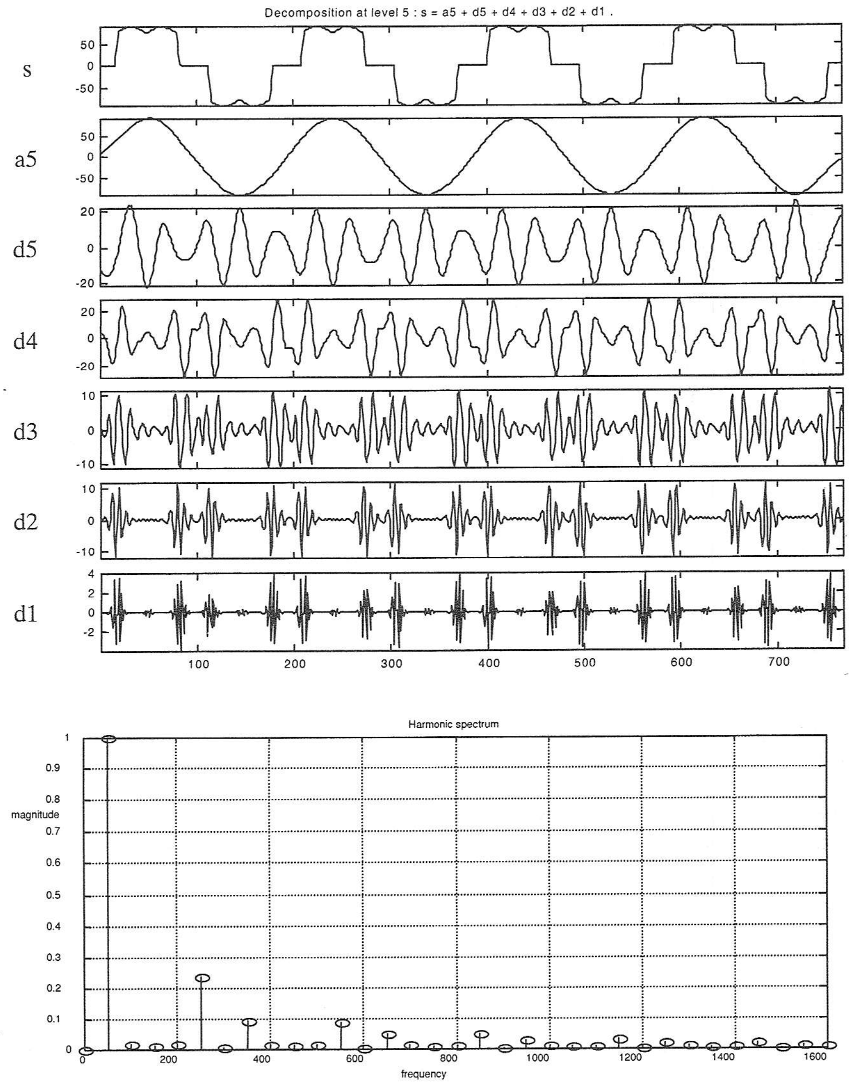

Fig 6. WT i FT of line commutated converter

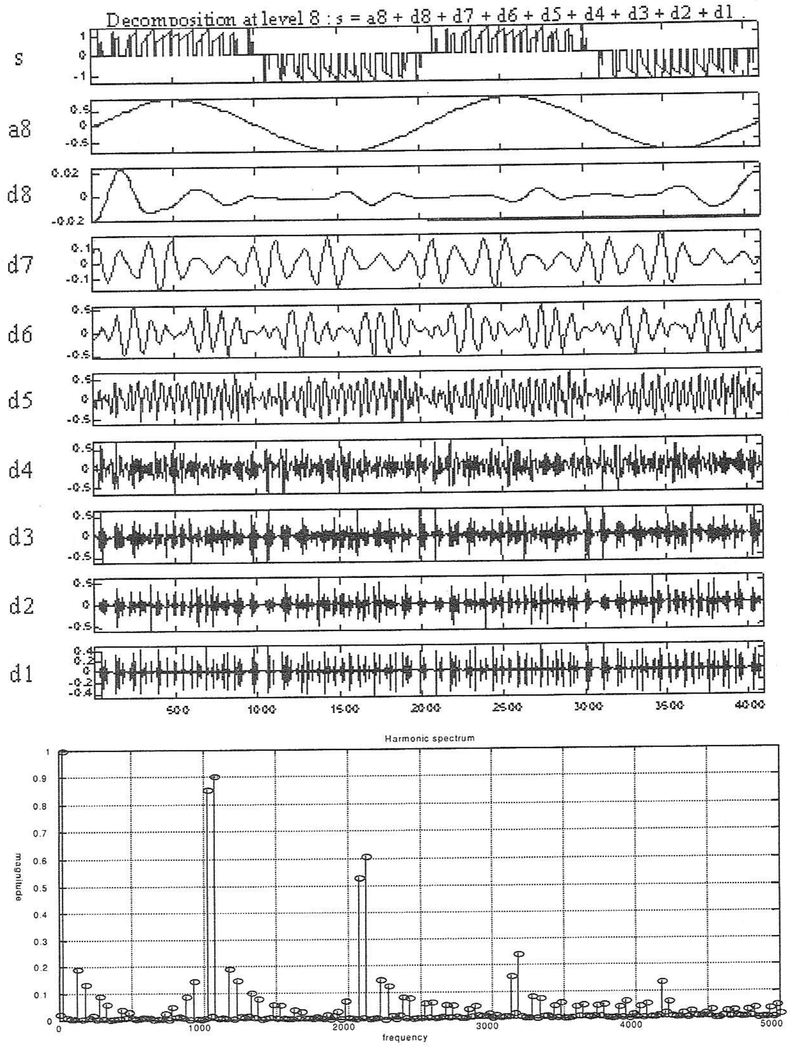

Fig 7. WT i FT in the case of PWM controlled current source converter

6. CONCLUSION

Wavelet Transform is a powerfull tool in signal analysis, which is suitable for harmonic analysis of current and voltage waveforms of modern power electronic devices. It eliminates certain drawbacks of the Fourier Transform as it has more narow window for harmonics and has more precise following of signal variation. The results presented in this paper prooved its advantages. The authors are expected that such analysis will be more widely applied in future, especially for transient signal analysis.

7. REFERENCE

[1] A.W. Galli, G.T.Heydt, P.F. Ribeiro: *Exploring the Power of Wavelet Analysis,* IEEE Computer Application in Power, October 1996, pp. 37-41.

[2] P.F. Ribeiro: *Wavelet Transform: An Advanced Tool For Analyzing Non-Stationary Harmonic Distortions in Power Systems,* Proceedings of *IEEE ICHPS VI,* Bologna, September 1994, pp. 365-369.

[3] D.C. Robetson, O.I. Camps, J.S. Meyer, W.B. Gish: *Wavelets and Electromagnetic Power System Transients,* IEEE Transactions on Power Delivery, Vol. 11, No. 2, April 1996, pp. 1050-1058.

[4] A. Graps: *"An Introduction to Wavelets"* IEEE Computational Sciences and Engineering, Volume 2, Number 2, Summer 1995, pp 50-61

[5] V. Kati}: *Analiza uticaja energetskih pretvara~a na kvalitet elektri~ne energije,* Savremeni aspekti elektroenergetike, Novi Sad 1995, pp.169-199. (in Serbian)

[6] A. Fournier: *Introduction,* Wavelets and their Applications in Computer Graphics, SIGGRAPH 1995 Course notes.

[7] A.W.M. vanden Enden, N.A.M. Verhoeckx: *Discrete-time signal processing,* Prentice Hall, New York 1989.

MOS CONTROLLED THYRISTOR MODEL FOR PSPICE SIMULATION

Goce L. Arsov

Faculty of Electrical Engineering, St. Cyril and Methodius University, 1000 Skopje, P.O.Box 574, Republic of Macedonia
tel. ++ 389 91 399105, fax. ++ 389 91 364262, e-mail: g.arsov@ieee.org

Abstract: *A simple PSpice model for the P-type MOS controlled thyristor (MCT) consisted of two sections is proposed. Its SCR section is based on the thyristor model proposed by Giacolletto [4]. The gate control section (MOSFET) is used for turning the MCT on and off. The proposed model represents the device characteristics during the turn-on and turn-off, as well as the breakdown and breakover characteristics of the SCR section. The parameters of the equivalent circuit can be calculated from the manufacturer data sheets and some simple measurements. The model has passed all performed tests and can be used to analyze various types of MCT power converters.*

Keywords: *PSpice/Simulation/Modeling/MOS Controlled Thyristor/Power Semiconductor*

1. INTRODUCTION

The MOS Controlled Thyristor (MCT) is a new power semiconductor device having several advantages compared with other devices. The MCT has a main thyristor section, and a gate control section for turning it on and off. Since the integration of the MCT is complex, it is very difficult to obtain an exact circuit model for the device. A complex model of the MCT has been developed by Harris Semiconductor [1]. A simpler model for the MCT would help to keep the simulation time and effort minimal. Such a model has been proposed in [2], but it seems that it does not simulate all the MCT characteristics properly (such as: SCR breakdown and breakover, turn-on spike voltages...). Its improved version is presented in [3].

This paper presents a simple circuit model for the P-type MCT suitable for analysis of MCT power converters, even with the student versions of PSpice. The model represents the characteristics of the MCT during turn-on and turn-off, as well as the breakdown and breakover characteristics of the SCR section. The model parameters can be obtained from the specifications contained in the manufacturer's data sheets and some simple measurements as described in [2] and [4]. Extensive simulations have been performed in order to test the proposed model characteristics. The model has passed all performed tests and can be used to analyze various types of MCT power converters. The static *I-V* characteristic and the simulation results of an MCT phase-controlled rectifier and a static AC switch using the proposed model are shown below.

2. CIRCUIT MODEL FOR THE P-TYPE MCT

The PSpice model for the P-type MCT is derived from the transistor level equivalent of MCT shown in Fig. 1. Its SCR section is developed by expanding the thyristor model presented in [4]. The gate control section consisting of a PMOS and an NMOS is modeled using simple *RC* circuit for the controlling of the turn-on and turn-off times and with simple diodes (D_{PMOS} and D_{NMOS}) to isolate the operation of the MOSFET's in such a manner that the triggering pulse of one polarity activates only one process of the MCT (either turn-on or turn-off).

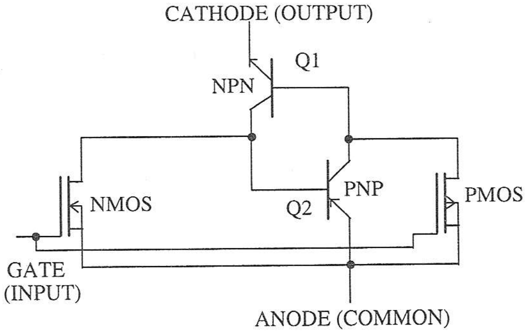

Fig. 1. *Transistor level equivalent circuit of the MCT*

The complete PSpice model is shown in Fig. 2 and the complete list of the PSpice statements for the subcircuit description of the proposed MCT model is presented in the appendix. The parameters of the MOSFET section can be calculated according the method presented in [2], and the parameters for the SCR section according the procedure explained in [4].

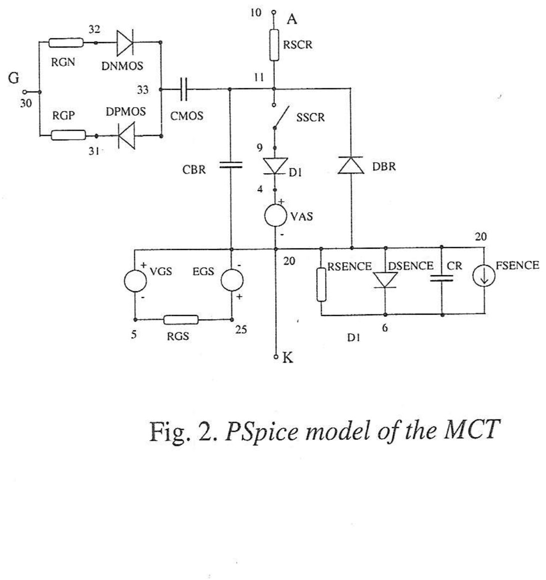

Fig. 2. *PSpice model of the MCT*

When a negative pulse is applied to the gate of the PMOS, the capacitor C_{MOS} charges up. The voltage across C_{MOS} increases the current through V_{GS} and consequently the value of F_{SENCE} which charges the capacitor C_R. The switch will be closed and the MCT in the ON state. Once the MCT is turned on, the current through V_{AS} will keep the device in the on state.

Once a positive pulse is applied to the gate, the capacitor C_{MOS} charges in the opposite direction, the E_{GS} reverses its direction and so does the current from F_{SENCE} The voltage across C_R changes its direction. The switch will turn off. The MCT is in the off state. The behaviour of the SCR section of the model is explained in [4]. The diode D_{BR} is included to ensure the breakover and breakdown capabilities of the MCT model, while the capacitor C_{BR} is added to provide the proper dv/dt characteristics.

3. SIMULATION RESULTS

Extensive simulations have been performed in order to test the proposed model characteristics. The model has passed all performed tests and can be used to analyze various types of MCT power converters. The static *I-V* characteristic of the MCT model given in Fig. 2, with the parameters defined by the statements in the appendix, is given in Fig. 3. The breakover and breakdown characteristics are clearly displayed.

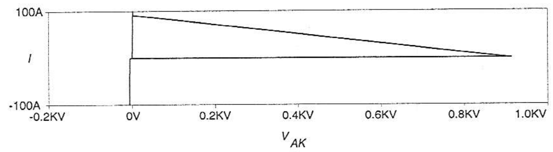

Fig. 3. *Static I-V characteristic of the PSpice model for the MCT given in Fig. 2*

The simulation results for the complete circuit of an MCT phase-controlled rectifier, shown in Fig. 4, are presented in Fig. 5. The converter uses a diode bridge to rectify the input ac voltage. The MCT is used as a phase-controlled switch to control the flow of power from the ac source. The diode D_m provides the freewheeling action. The waveforms of the input voltage, load voltage and gate pulses are shown in Fig. 5. Comparing them with the experimental waveforms shown in [2] it can be seen that the simulated waveforms agree very well with the experimental ones.

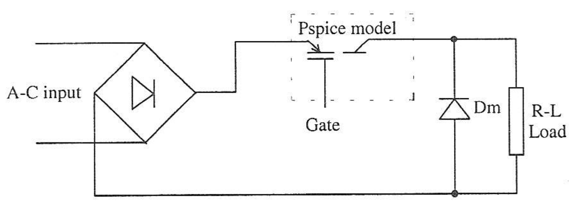

Fig. 4. *Power circuit of the MCT phase-controlled rectifier*

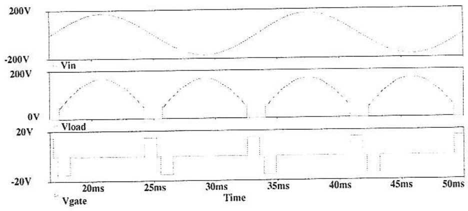

Fig. 5. *Simulated MCT converter waveforms*

The successful simulation results have been obtained for other circuits. Some tests described in [1] have been successfully passed. For example, in Fig. 7 we present the simulation results for an AC switch using two MCTs with common gate circuit (Fig. 6). It can be seen that they correspond very well with the experimental waveforms given in [1] (Fig. 6.4.2). The comparative simulations have been performed using the P-type MCT models developed in [2] and [3], and the MCT model developed by Harris Semiconductor (MCTV75P60E1), available on Internet. The simulation times were shorter, in average, by 15%, comparing with those obtained with the model from [3], and by 33 % than those obtained using the HARRIS Semiconductor model. All simulations have been performed using the PSpice Evaluation version 5.0a.

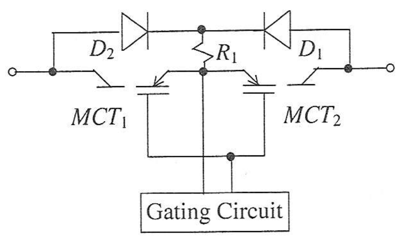

Fig. 6. *AC switch using two MCTs with common gate circuit*

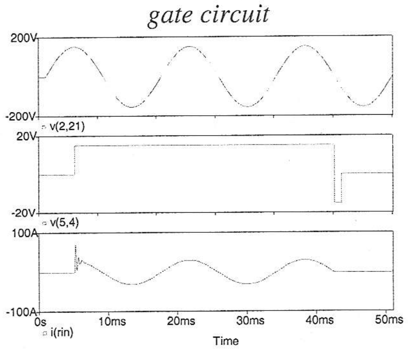

Fig. 7. *Simulation waveforms or the AC switch of Fig. 6: upper trace – input voltage; middle trace – gate control voltage; lower trace – load (5 Ohms, 20 μF) current. Closing at zero, opening near mid-cycle;*

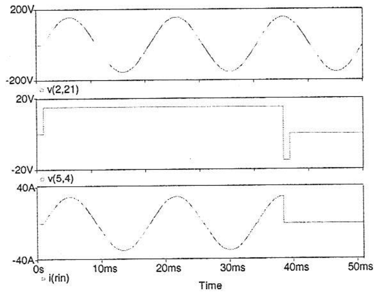

Fig. 7. *Simulation waveforms or the AC switch of Fig. 6: upper trace – input voltage; middle trace – gate control voltage; lower trace – load (5 Ohms, 20 μF) current.*

closing at mid-cycle, opening near zero

4. CONCLUSION

The paper presents a simple PSpice model of the MCT. The model has a thyristor section and one section, combining two MOSFET's, for turning the MCT on and off. The model is simple and it represents the characteristics of the MCT during turn-on and turn-off, as well as the breakdown and breakover characteristics of the SCR section. The extensive simulations performed show very good behaviour of the proposed model. The simulation results are compared with those presented in [2] and [3], and also with the results obtained using the MCT model developed by Harris Semiconductor and available on Internet. The proposed model needs less memory requirements, and the simulation times were shorter by 15% to 33% comparing with the other available models.

5. REFERENCES:

[1] MCT User`s Guide, Harris Semiconductor Corporation, 1995

[2] S. Yuvarajan and D. Quek, "A PSPICE Model for the MOS Controlled Thyristor" *IEEE Trans. Ind. Electron*, Vol. 42, No 5, pp 554-558, 1995.

[3] G. L. Arsov and Ljupco P. Panovski, "An Improved PSpice Model for the MOS Controlled Thyristor", *IEEE Trans. Ind. Electron.*, Vol. 43, No. 2, pp 473-477, 1999

[4] L. J. Giacoletto, "Simple SCR and TRIAC Computer Models, *IEEE Trans. Ind. Electron*, Vol. 36, No 3, pp 451-455, 1989.

APPENDIX

<u>*Subcircuit description of the MCT*</u>

```
*MCT model

.SUBCKT MCT 10 20 30
*--------------------A  K  G
RGP      30   31   5
RGN      30   32   8.33
CMOS     33   10   18.92N
DPMOS    33   31   D
DNMOS    32   33   D

*SCR SECTION
EGS      25     20     TABLE {V(33,10)}  +(-
100,-100) (-.15,0) (.15,0) (100,800)
RGS     25    5    1
VGS     20    5    0
RSCR    10    11   .005
SSCR    11     9    6   20   SSCR
D1       9     4    D


.MODEL  D     D(N=.1)
VAS    4    20    0
.MODEL       SSCR    VSWITCH(RON=.0125
+  ROFF=103000 VON=1 VOFF=0)
FSENSE   20     6     POLY(2)  VGS  +  VAS
-.05   55   11
DSENCE 20    6    DS
.MODEL   DS     D(RS=.05)
RSENSE  6    20     1
CR         6    20    5U
CBREAK  11     4     18P
DBREAK  4     11     DBR
.MODEL   DBR      D(BV=900 N=6 +  IS=1E-
14)
.ENDS
```

C-V Characteristics of VDMOSFET with Degraded Oxide

Predrag Habaš [1), 2)], Miloš Živanov [2)] and Saša Mileusnić [2)]

1) Philips Semiconductors, Dev. Eng. Dept., MOS4, Gerstweg 2, 6534 AE Nijmegen (NL)
2) Faculty of Technical Sciences, Univ. of Novi Sad, Fruškogorska 11, 21000 Novi Sad (Yu)

Abstract: *C-V characteristics are studied as a potential tool for reliability assessment of power VDMOSFETs. In particular, split C-V characteristics of VDMOST are evaluated. The study focus on uniform and non-uniform degradation of gate oxide of irradiated VDMOST. A technique has been proposed for separate measurements of gate oxide damage in the channel and the epitaxial region. Two-dimensional numerical analysis confirms the applicability of the technique, showing its advantages and limitations. Examples of power VDMOSFETs damaged by Fowler-Nordheim gate injection, as well as irradiated with Cs^{137} are given.*

I. INTRODUCTION

Damage of gate oxide in VDMOSFET may occur by hot-carrier injection, irradiation and gate-bias stress.

Recently, **hot-carrier injection** is found to be of concern in LDMOSFETs, particularly those made as high-voltage planar devices in IC technology [1,2,3]. In power VDMOSFETs under normal operating conditions hot-carriers are of minor concern, because lateral electric fields (carrier heating) are relatively small due to relatively large channel lengths and moderate voltage drop in the channel. This may further change when scaling channels of power VDMOSFET into submicrometer region.

Gate-bias stress may result in avalanche multiplication in the oxide, leading eventually to destructive oxide breakdown. At lower gate biases, Fowler-Nordheim injection occurs, which degrades the oxide, and also leads to catastrophic breakdown when Q_{BD} (injected charge to breakdown) is exceeded. For t_{ox}=100nm gate-oxides of VDMOS-FETs used in this study (EFN1N10/EFA1N15/20 made by Ei-Microelectronics, Niš), significant FN injection occurs for V_{GS}>60-70V. This degradation mode is not relevant for practice, because operating gate biases are much lower for power VDMOSFETs. Eventually, a significant gate-bias stress may occur during ESD (electrostatic discharge) event, which may cause fail of VDMOSFET [4].

The most studied degradation of power VDMOS-FETs is that caused by **irradiation**. It is typically studied in relation with aerospace and cosmic applications, were power MOSFETs can be irradiated significantly. VDMOSFETs used as switches in high-frequency power supplies in satellites are exposed to such high cosmic radiation that they absorb an ionisation dose of up to 50krads during 10 years of satellite mission [5]. Commercial power VDMOS-FETs cannot provide sufficient hardness against radiation and special hardening techniques are required (gate-oxide grown). In order to characterize response of VDMOSTs to irradiation, the following methods have been used in research and production:

1) I-V methods, and
2) charge pumping [6,7].

There are two groups of I-V methods. The first group of I-V methods focus on characteristics I_D vs. V_{GS} above threshold; they are based on surface mobility change and threshold voltage shift after irradiation. Both quantities are affected by charge in interface traps created by irradiation ΔN_{it} and by charge trapped in gate oxide ΔN_{ox}. Monitored experimental quantities are either drain current [8], gain β [9,15] or MOSFET transconductance g_m [10]. These methods deal exactly with the quantities in the bias region that is of major importance for VDMOS operation. For mobility-degradation the related charge in interface traps ΔN_{it} is a "sum" of concentration of positively and negatively charged sites $\Delta N_{it}^{+\&-}$. For threshold voltage shift the related charge ΔN_{it} is a net charge $\Delta N_{it}^{\pm}$ and its relation to the total number of interface traps depends on the nature of traps. The nature of interface traps is, however, not clarified in scientific community. We do not know whether $\Delta N_{it}^{+\&-}=\Delta N_{it}^{\pm}$ holds; the relationship that has been *a priori* assumed in the derivation of the method [9]. These I-V methods are not directly applicable, if trap density varies significantly across the energy close to the band edge, because they implicitly assume that ΔN_{it} does not change with V_{GS} and Fermi level at the interface. All methods for the extraction of ΔN_{ox} and ΔN_{it} that are based on the drain current, gain and mobility change after irradiation strongly rely on (unknown) model coefficients for the strength of the impact of N_{ox} and N_{it} on surface mobility.

Second group of I-V methods deal with subthreshold characteristics: subthreshold slope [5], threshold-voltage shift [5] and mid-gap method [10,11]. The related interface trap density in the individual methods is: the total trap density for subthreshold slope method ($N_{it}^{+\&-}$), and the net charge in interface traps $N_{it}^{\pm}$ for ΔV_{th} and mid-gap methods. The net charge depends on the nature of traps (donor-like or acceptor-like, and their distribution across the gap). Assuming acceptor-like nature of interface traps in the upper half and donor-like in the lower half of the band gap enables separation of ΔN_{ox} and ΔN_{it} in the mid-gap method. This assumption originates from the common believe that most traps at SiO_2/Si interface are Pb centres (free dangling bonds ≡Si•), which should be amphoteric [16]. In that case, $N_{it}^{+\&-}=N_{it}^{\pm}$ holds. It is not clarified yet, whether all, most or some radiation-induced or hot-carrier induced interface traps are Pb centres. For these techniques the relevant energy portion of the band gap is from intrinsic level (neutral point) (or eventually valence band-edge, if not all traps are Pb centres), up to $2\varphi_B$ (double Fermi barrier for threshold onset). Traps between $2\varphi_B$ and conduction band edge affect device characteristics above threshold, but they are not sensed by the subthreshold methods. The mid-gap method faces difficulties for trap distribution localized in the energy space: the extrapolation towards mid-gap point may be inaccurate.

All I-V methods measure the effective charge trapped in the gate oxide ΔN_{ox} and interface trap density ΔN_{it} build-up in the channel close to the source after irradiation. They do not sense the gate oxide damage in the epitaxial (epi) region.

Recently, charge pumping (CP) has been applied to separate ΔN_{ox} and ΔN_{it} in irradiated VDMOSFETs [6,7]. The related ΔN_{it} is the total concentration of interface traps, irrespective of their nature. Extracted value of trapped charge ΔN_{ox} depends on assumed nature of interface traps. If ΔN_{ox} >> ΔN_{it} holds, the measurement of ΔN_{ox} is accurate. If concentration ΔN_{it} is comparable to ΔN_{ox}, the extracted ΔN_{ox} depends on the trap nature. The CP is only capable to characterize oxide and interface above the epitaxial region and in a part of the channel at the drain side, but not in the channel close to the source. Note that the channel at the source-side of the channel determines V_{th} and I_D of VDMOSFET in the whole.

These I-V and CP methods are adopted from numerous studies of uniform degradation of standard MOSFETs. Some methods known in MOS studies have not been used for power VDMOSFETs yet: noise, gate-current characteristics and various C-V techniques.

Although highly developed for MOS capacitors and standard MOSFETs, the C-V techniques have not been used in reliability study of power VDMOSFETs yet. Recently, a detailed study of the gate total capacitance and split C-V characteristics of VDMOS structure is made by means of numerical simulations and experiments by these authors [12]. Study [12] provides understanding of the split C-V characteristics of virgin (non-irradiated) VDMOSTs, and sets a basis for the potential application of the method to measure the oxide damage in irradiated devices [13].

This paper analyses the applicability of split C-V technique to characterize oxide damage ΔN_{ox} and ΔN_{it} in irradiated power VDMOSTs. We focus on the damage separation in the channel and epitaxial region. The split C-V characteristics of fresh VDMOST are recapitulated in Section II. C-V characteristics of irradiated devices are explained in Section III, where results of numerical-modelling studies are given. Section III presents a new method for the separation of damage ΔN_{ox} and ΔN_{it} in VDMOSTs. Experimental characteristics are shown in Section IV for devices subjected to gate-stress and radiation.

II. C-V CHARACTERISTICS OF VDMOST

Gate capacitance characteristics C_g vs. V_g of n-channel VDMOSFET [17] shows a complex structure that is a superposition of the contributions of [12]:

1) epitaxial region (standard C-V characteristics for uniform n-bulk MOS devices),
2) laterally nonuniform channel (strongly deformed C-V characteristics with stretched depletion and a very smooth electron inversion), and
3) n+ source part (nearly constant capacitance).

Gate capacitance $C_g(V_g)$ is a mixture of contributions due to electron and hole inversion, depletion and accumulation in the epi region (n^-) and channel (p^-). Contrary to $C_g(V_g)$, in the split C-V characteristics $C_{gs}(V_g)$ and $C_{gd}(V_g)$ these contributions are separated. A complete explanation of the structure of the gate capacitance and the split C-V characteristics of VDMOST is presented in [12], where extensive numerical modelling and various experiments are employed. In summary: one part of characteristics $C_{gs}(V_g)$ is solely determined by hole inversion in epi region; the other part is solely determined by the depletion of p^- region of the channel. For $C_{gd}(V_g)$, one part is solely determined by the epi-region depletion, while the other part is solely affected by inversion in the channel (starting from the drain channel-side).

On power VDMOSFETs the split C-V characteristics are measured like on conventional bulk MOSFETs. The experimental set-up is show in Fig.1: it is identical with set-up used for standard split C-V measurements. However, the interpretation of the characteristics $C_{gs}(V_g)$ and $C_{gd}(V_g)$ is more complex, as it involves overlapping contributions from three interface regions 1)-3) [12]. Like for conventional MOSTs, it holds $C_g(V_g)=C_{gs}(V_g)+C_{gd}(V_g)$ for VD-MOSFETs as well, as shown on measured characteristics in Fig.2.

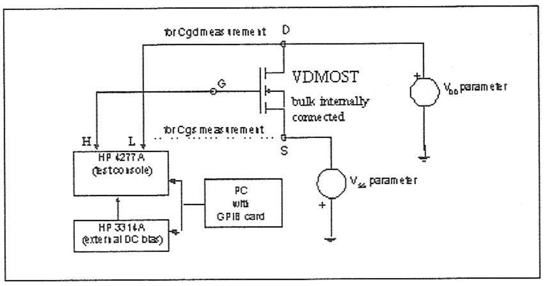

Fig.1: Experimental set-up for our split C-V measurements on power VDMOSFETs. Important for the interpretation of the split C-V signals is that p-diffused region is internally connected to n^+ source (n-channel). Voltage sources V_{DD} and V_{SS} provide V_{DS} bias in measurements of C_{gs} and C_{gd}, respectively.

Applying drain-source bias V_{DS} enhances separation of the particular components of the epi-interface and the channel. With $V_{DS}>0$ hole inversion at the epi interface is further separated from the depletion in the epi and p^- regions, as demonstrated on the measured characteristics in Fig.3. A detailed experimental and modelling study of the V_{DS}-effect on split C-V curves is given in [12]. For the study in this paper, it is essential that V_{DS} bias improves the separation of the parts of the characteristics determined by the channel from that determined by the epi region only, thus enabling better separation while extracting oxide damage ΔN_{ox} and ΔN_{it} in these regions.

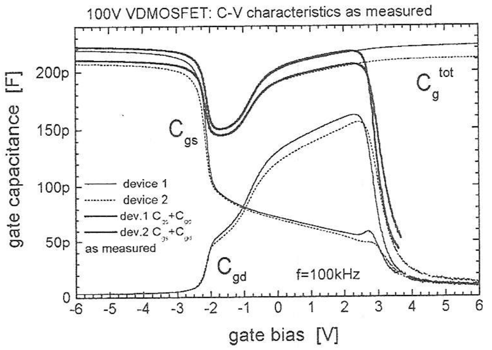

Fig.2: Total gate capacitance and split C-V characteristics measured on two 100V VDMOSFETs. The sum of the split C-V components C_{gs} and C_{gd} equals to the total gate capacitance for V_g below threshold V_{th}. Above V_{th} the split C-V are not valid.

III. CHARACTERISTICS OF DEGRADED VDMOST: MODELLING

Changes in C-V characteristics of VDMOSFETs after gate-oxide damage are studied by means of numerical modelling. The rigorous 2D numerical model is the same as explained in [12]. It applies small signal ac analysis with MINIMOS-6. In order to study devices that are close to reality, input doping profiles are obtained by process simulation MUSIC-2, starting from the full process flow [14]. Oxide damage is assumed in form of fixed oxide charge (trapped charge sheet) N_{ox} and interface traps N_{it}. Interface traps are modelled either as acceptor-like across the whole band gap or as amphoteric (acceptor-like in upper and donor-like in lover half of the gap). For simplicity, constant trap density is set across the band gap. Traps are fully accounted for the dc modelling of the device operation point. They are also included in quasi-static (QS) simulation of the gate-capacitance components (Fig.4). They are, however, omitted from the small signal ac system of semiconductor equations, i.e. interface traps are assumed to be inert to applied ac signal (Fig.5). Therefore, the calculated inter-terminal capacitances by means of the ac model are high-frequency (HF) with respect to traps.

In first model-study spatially uniform damage after irradiation is assumed: $\Delta N_{ox}=8\times10^{11}cm^{-2}$ (trapped holes), $D_{it}=3\times10^{11}cm^{-2}eV^{-1}$ (uniform, with different trap nature). Fig.4 shows numerically calculated quasi-static gate capacitance components that originate from individual VDMOST regions: epi-interface C_g^{n-}, channel C_g^{p-} and source region C_g^{n+}. While oxide trapped charge only induces a parallel shift in the C-V characteristics of all interface parts, traps stretch-out the characteristics by changing dc operation point and by adding their own capacitate component. Characteristics of the epi layer C_g^{p-} exhibits an "ideal" C-V behaviour like for MOS structure with n-type uniform bulk doping. Channel shows strongly deformed C-V characteristics due to laterally non-uniform profile.

When amphoteric interface traps are assumed, for both, epi and channel region, the C-V characteristics exhibits a parallel shift with respect to those for acceptor-like traps, Fig.4. Therefore, like in any MOS system, the trap nature cannot be determined without exact knowledge of the value of fixed charge N_{ox}.

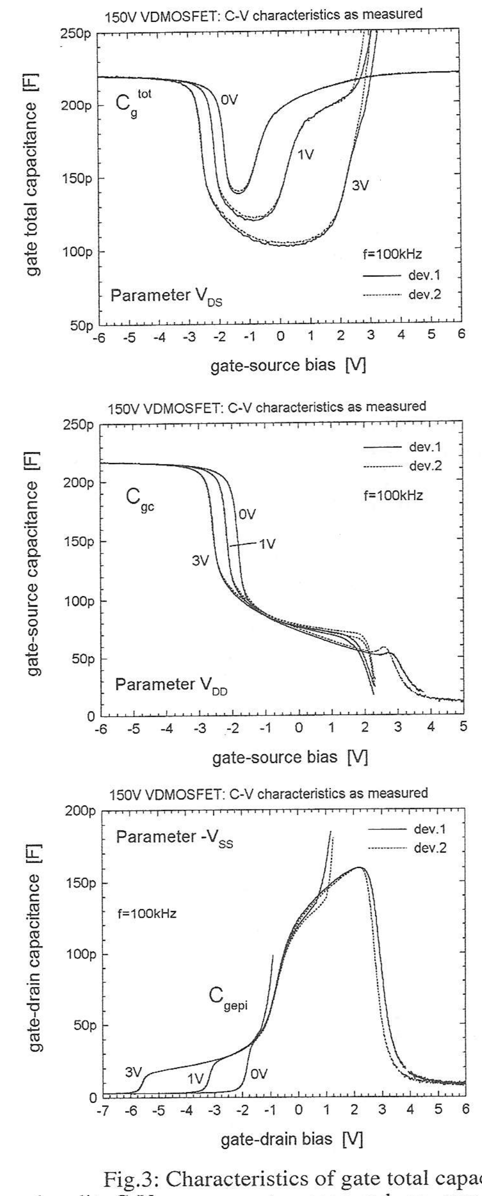

Fig.3: Characteristics of gate total capacitance and split C-V components measured on two 150V (fresh) devices with drain-source bias V_{DS} as parameter. Applying V_{DS} enhances the separation of the contributions of the channel and the epi region.

In the part where hole inversion takes place at the epi interface (V_g<-5V in Fig.4 for "irradiated" devices), there is a small effect due to hole accumulation-depletion in the p- channel, but the major component of C_g^{tot} is due to C_g^{n-}. In this region, C_g^{n-} is divided in split C-V measurements into pure hole inversion component C_{gs} and electron depletion component C_{gd}. Equivalent analysis holds for electron inversion in the channel (V_g>-3V in Fig.4).

The calculated split C-V components that correspond to model-experiment in Fig.4 are shown in Fig.5. The shift and distortion of $C_{gd}(V_g)$ and $C_{gd}(V_g)$ are due to ΔN_{ox} and ΔN_{it} generated in stress, respectively. On the split C-V characteristics the damage in the channel can be distinguished from the damage in the epi region, because different segments of the curves are affected by these damages.

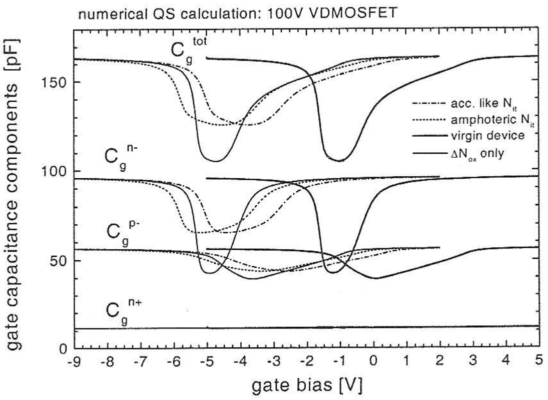

Fig.4: Calculated quasi-static gate capacitance components due to epi-interface C_g^{n-}, channel C_g^{p-} and source region C_g^{n+} in a VDMOSFET (MINIMOS6). Assumed damage: ΔN_{ox}=8x10^{11}cm^{-2} (holes trapped), D_{it}=3x10^{11}cm^{-2}eV^{-1} (uniform) – different trap nature.

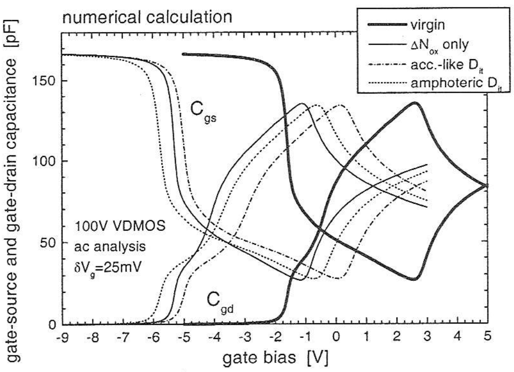

Fig.5: Simulation of changes in high-frequency (HF) inter-terminal capacitances of VDMOSFET from Fig.4 (model of HF split C-V measurements; small signal ac analysis with MINIMOS-6 employed).

The possibility to separate damage in different oxide regions is demonstrated by the following model-experiments. Numerically calculated split C-V curves of a 100V VDMOST are shown in Fig.6 for different amounts of trapped holes ΔN_{ox} in the oxide above the epi region and the channel. For simplicity, there is no increase in interface trap density. The specific segments of split C-V components are shifted by a constant voltage of q· $\Delta N_{ox}/C_{ox}$, exactly according to the assumed different ΔN_{ox} amounts in the epi region and the channel. In study in Fig.6 components are additionally separated by applying V_{DS}=2V.

The effect of different interface trap densities in different interface regions of VDMOST is also analysed by using numerical modelling with MINIMOS-6. The results are shown in Fig.7 for V_{DS}=0V and Figs.8 for V_{DS}=2V. In these studied the amount of trapped holes is fixed to ΔN_{ox}=2x10^{11}cm^{-2}, while different density of acceptor-like interface traps is assumed in the channel and the epi region. The shift in characteristics is caused by charge in interface traps, while the charge is dependent on surface Fermi level, i.e. gate bias, which results in distortion. Density of interface traps may be extracted from C-V characteristics by standard Terman's (HF) method. Particular interface regions only affect specific segments of the split C-V characteristics.

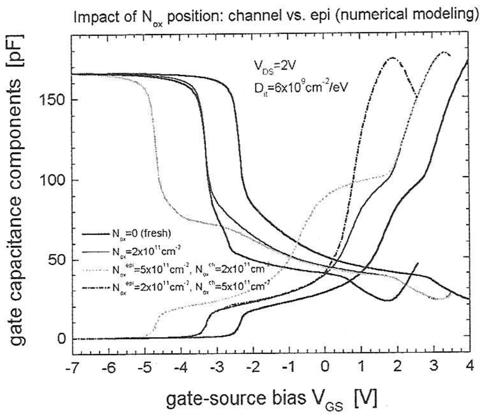

Fig.6: Calculated changes in HF inter-terminal capacitances of a VDMOSFET after "irradiation". Assumed oxide damage in form of trapped holes uniformly distributed, and with different densities in the channel N_{ox}^{ch} and epi region N_{ox}^{epi}.

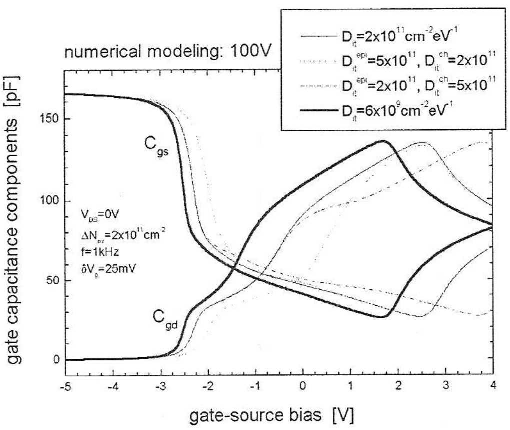

Fig.7: Calculated changes in HF inter-terminal capacitances of a VDMOSFET after "irradiation". Assumed oxide damage in form of acceptor-like interface traps with different densities in the channel D_{it}^{ch} and epi region D_{it}^{epi}. Uniform distribution in energy and position space. Vanishing drain-source polarisation.

For example: the segment of the characteristics C_{gd} from –2.3V to –1.3V in Fig.7 (the curve without damage, i.e. for D_{it}=6x10^9cm^{-2}eV^{-1}) is determined by electron depletion in the epi region. In characteristics of degraded devices the corresponding (shifted) segment is affected by traps on the epi interface only, and is independent of trap density in the channel. For this segment a rough application of Termans's method

$$D_{it}(E_F) = -\frac{C_{ox}}{e\cdot(1-C_G^{QS}/C_{ox})}\cdot\frac{\partial(\Delta V_{GB})}{\partial V_{GB}} \qquad \text{Eq.(1)}$$

results in values of $\Delta D_{it}=1.7\text{x}10^{11}$ and $4\text{x}10^{11}\text{cm}^{-2}\text{eV}^{-1}$ which are close to values $1.94\text{x}10^{11}$ and $4.94\text{x}10^{11}$ used as input in numerical calculation.

The modelling-studies show that the damage in channel and the epi region can be extracted from the same characteristics measured on the same degraded VDMOSFET. For the charge separation between ΔN_{ox} and ΔN_{it} in particular regions, standard CV techniques may be applied, involving, however, all known model assumptions and measurement limitations of them (trap nature, the position of the neutral point and the response of some traps to HF signal are some well known). Note that further modelling work is required to study the accuracy of the ΔN_{it} extraction in the channel region of VDMOSFET.

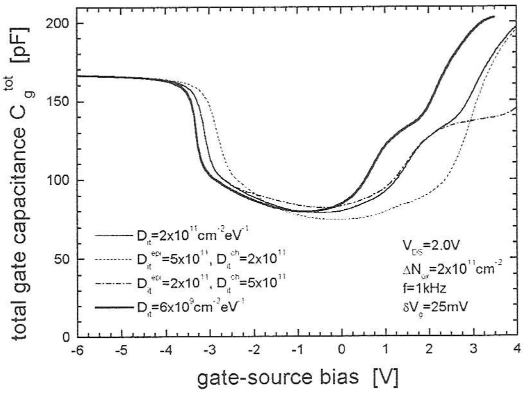

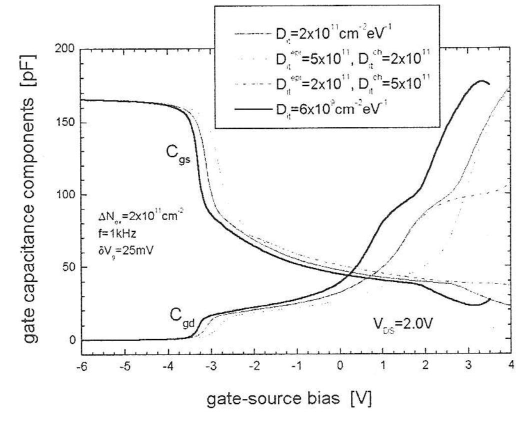

Figs.8: Calculated changes in HF gate total capacitance and inter-terminal capacitances of a VDMOSFET after "irradiation". Conditions as for Fig.7, but with V_{DS}=2V.

IV. EXPERIMENTAL STUDIES

In the first set of experiments VDMOSFETs are electrically stressed by applying gate-bias stress. Positive high DC voltage $+V_G$ is applied on gate, while source and drain are set on ground potential. For high positive V_G the channel is inverted, and the epi-interface is strongly accumulated. In spite of laterally non-uniform doping profile along the interface, which induces spatial variations in surface potential, electric field in the oxide is almost constant across the whole gate area because of high $+V_G$. Electrons tunnel from the silicon-substrate towards the gate by Fowler-Nordheim effect. If the oxide thickness is spatially uniform, FN current with constant area-density is injected into the gate oxide. For the same oxide quality near the edges of the hexagonal gate cells as in the middle of the cells, the overall gate oxide is degraded uniformly.

From the total gate area of $A_g=A_{gcell}\cdot N_{cell}$ (A_{gcell} is the gate area per one cell, and N_{cell} number of VDMOS cells in power VDMOST die), the measured injection current I_g and injection time t_{inj}, it follows the injected charge: $Q_{inj}=I_g\cdot t_{inj}/A_g$ [C/cm^2]. In stress: I_g=11.4nA, A_{gcell}=663μm^2, N_{cell}=860, t_{inj}=100s, and J_{inj}=2μA/cm^2, which results in injected charge Q_{inj}=0.2mC/cm^2. This is far bellow Q_{BD} (charge to breakdown) value, but is sufficient to significantly damage the oxide. The applied electric field during injection was in the range 6-7MV/cm. The measured I-V characteristics of VDMOST before and after injection are shown in Figs.9-10. Discussion of I-V methods is out of scope of this paper. Here we only point out that neglecting the effect of the series resistance of ammeter used for measurements (common Keithley 617 applied for Figs.9-10) may result in improper characteristics in the linear region above threshold due to variable V_{DS} (Fig.9-upper). Correct measurements should apply an adaptive drain voltage source V_{DD} that forces a constant V_{DS}. The correct curves in Fig.9-lower deviate remarkably from the original in Fig.9-upper. In the measurements, ammeter is placed in the source branch; the extracted series resistance of the instrument is 0.8Ω in the mA range.

FN injection induces negative shift in I-V characteristics by amount of 1.17V at the midgap current level I_{Dmg}, as shown in subthreshold characteristics in Fig.10. This shift corresponds to $\Delta N_{ox}=2.5\text{x}10^{11}\text{cm}^{-2}$ (trapped holes). The mid-gap method, including the current at the threshold onset I_{Dth}, provides trap density of $\Delta N_{it}=3.5\text{x}10^{10}\text{cm}^{-2}$. After 48h room-temperature anneal the characteristics slightly change resulting in: $\Delta N_{ox}=2.8\text{x}10^{11}\text{cm}^{-2}$, $\Delta N_{it}=6\text{x}10^{10}\text{cm}^{-2}$.

C-V characteristics of VDMOST that is stressed by FN injection are shown in Figs.11. Data is presented before stress (fresh VDMOST) and immediately after stress, while the data after 48h is omitted. Characteristics are measured for different drain-source biases (0, 1 and 2V).

After the stress characteristics $C_{gd}=C_{gepi}$ show relatively constant negative shift on V_G-axis, that corresponds to about $6.7\text{x}10^{11}\text{cm}^{-2}$ net positive charge. The shift is the same for segments of the characteristics influenced by epi only or by channel only, which reflects a uniform damage across the interface. The characteristics $C_{gs}=C_{gc}$ (gate-channel) shows a negative shift after stress. The shift is bias-dependent. The C_{gs} curves are more stretched-out due to interface traps than the curves for C_{gd}. The total net positive charge extracted from characteristics $C_{gs}(V_g)$ varies from $5.5\text{x}10^{11}$ to $6.8\text{x}10^{11}\text{cm}^{-2}$, for both epi region and the channel.

These values are much larger than the values extracted for the same device from subthreshold I-V characteristics in Fig.10.

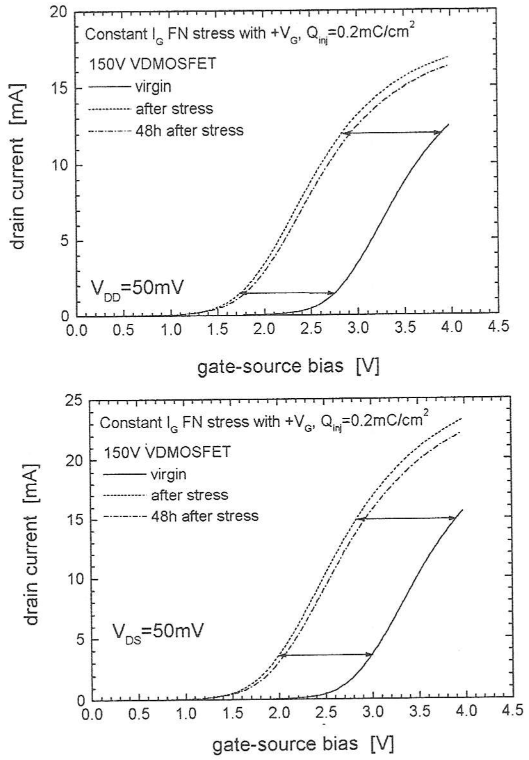

Figs.9: Measured drain current in the linear region on a VDMOST before stress, after FN-injection stress and 48h after stress. Upper figure: drain is biased by constant voltage source of V_{DD}=50mV. Lower figure: V_{DD} is adapted that V_{DS}=50mV is constant.

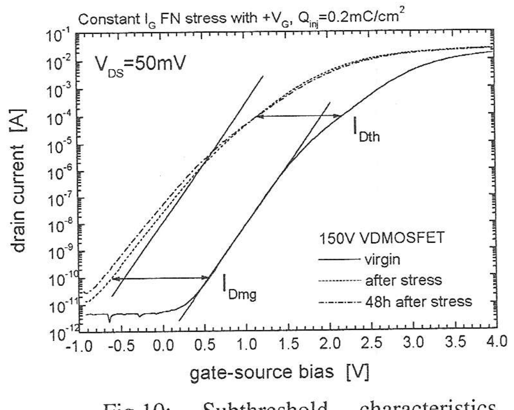

Fig.10: Subthreshold characteristics of VDMOST from Fig.9. Mid-gap current I_{Dmg} and threshold voltage current I_{Dth} are denoted.

A comment is made on resulting positive net oxide charge in the FN stress. FN injection typically results in positive charge (trapped holes) short time interval after applying the gate bias. For longer stress times negative charge (electron trapping) predominates, as a consequence of the generation of neutral electron traps in oxide, and electron trapping on these and native centres. In our FN stress the injection level is low: 1.25×10^{15}electrons/cm^2, and the oxide field is relatively low. In these conditions the positive oxide charge due to anode-hole-injection predominates long initial period of stress.

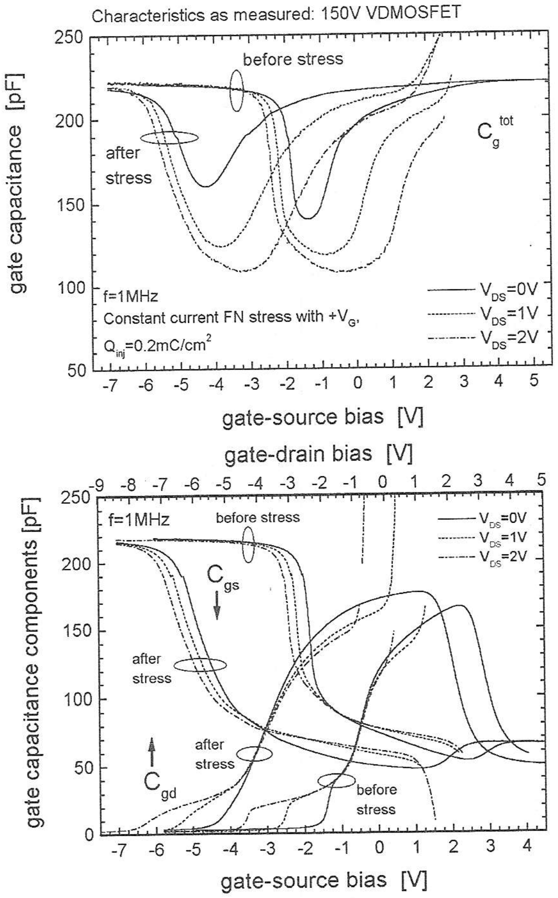

Figs.11: Experimental gate total and split C-V characteristics measured on a 150V VDMOSFET before and after uniform constant current FN gate oxide injection with $+V_G$ and Q_{inj}=0.2mC/cm^2 (t_{ox}=100nm). The shift and distortion of $C_{gd}(V_g)$ and $C_{gd}(V_g)$ are due to ΔN_{ox} and ΔN_{it} generated in stress.

In the second set of experiments VDMOSFETs are irradiated by exposing them to Cs_{55}^{137} γ-source. In radiation and post-radiation relaxation the device was not biased. Results of irradiation of a 200V VDMOS-FET, combined with room and high-temperature anneal (110°C) are shown in Figs.12. After irradiation a spatially nearly uniform positive charge is observed. After 24h room-T relaxation, very slight changes due to small ΔN_{it} are found. Anneal at 100°C, applied after 24h in duration of 8h, results in significant increase in ΔN_{it}.

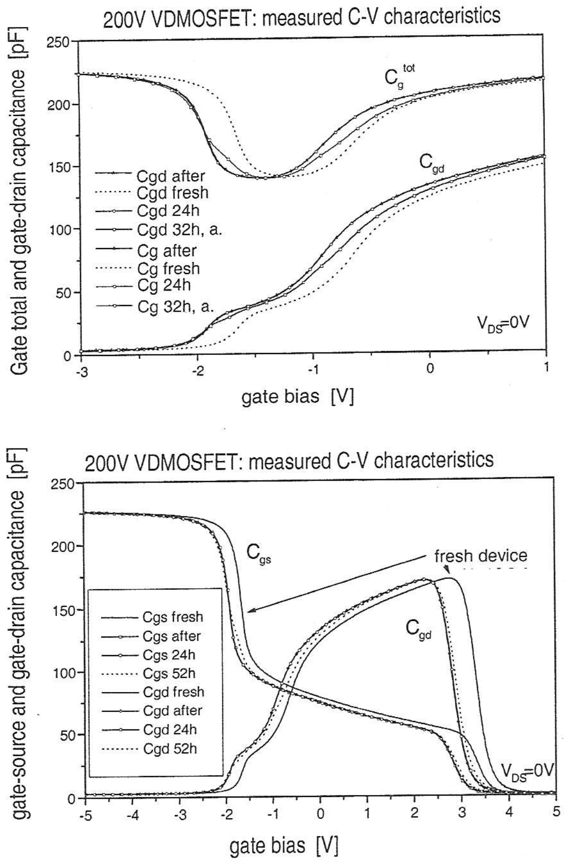

Figs.12: Measured gate total capacitance and split C-V characteristics of a 200V VDMOSFET. Device is irradiated with Cs^{137} -source in dose of 3krad, with dose rate 50rad/h. The characteristics are shown for virgin (fresh) device, immediately after irradiation, 24h after irradiation (room temperature), 32h after irradiation where anneal at 110°C in performed from 24h to 32h, and 54h after irradiation (room temperature).

REFERENCES:

[1] R.Versari, A.Pieracci, S.Manzini, C.Contiero and B.Riccò, "Hot-Carrier Reliability in Submicrometer LDMOS Transistors," IEDM Techn.Dig., 371, 1997.

[2] E.Vandenbossche, C. DeKeukeleire, M. De Wolf, H.Van Hove and J.Witters, "Modelling and simulation of hot-carriers degradation of high voltage floating lateral NDMOS transistors," Microelectronics Rel. 38, 1097, 1998.

[3] A.Pieracci and B.Riccò, "A New Characterization Method for Hot-Carrier Degradation in DMOS Transistors," IEEE Tr.ED 45(8), 1855, 1998.

[4] G.Biermann, "A statistical method for the detection of gate oxide breakdown due to fast EOS events, such as ESD, on power DIMOS devices," EOS/ESD Symp., 143, 1993.

[5] T.Sakai and T.Yachi, "Effects of gamma-ray irradiation on thin-gate-oxide VDMOSFET characteristics," IEEE Tr.ED 38, 1510, 1991.

[6] P.Habas, Z.Prijic and D.Pantic, "The application of charge-pumping technique to characterize the SiO_2/Si interface in power VDMOSFETs," Proc. INFOS, 171, 1995.

[7]

[8] P.Habas, Z.Prijic, D.Pantic and N.Stojadinovic, "Charge-Pumping characterization of SiO_2/Si interface in virgin and irradiated power VDMOSFETs," IEEE Tr.ED 43, 2197, 1996.

[9] D.Župac, K.F.Galloway, R.D.Schrimpf and P.Augier, "Effects of radiation-induced oxide-trapped charge on inversion-layer hole mobility at 300 and 77K," Appl.Phys.Lett.60(25), 3156, 1992.

[10] S.Dimitrijev and N.Stojadinović, "Analysis of CMOS transistor instabilities," Solid-St. Electr.30 (10), 991, 1987.

[11] P.McWhorter and P.Winokur, "Simple technique for separating the effects of interface traps and trapped-oxide charge in metal-oxide-semiconductor transistors," Appl.Phy.Lett 48, 133, 1986.

[12] J.R.Schwank, et al., "A critical comparison of charge-pumping, dual transistor and midgap measurement techniques," IEEE Tr.NS 40, 1666, 1993.

[13] P.Habaš, S.Mileusnić and M.Živanov, "Characterization of Power VDMOSFETs by Split C-V Measurements," in Proc. of MIEL, 339, 2000.

[14] P.Habaš, S.Mileusnić and M.Živanov, "Split C-V Measurements: a new Approach to Characterize Oxide Degradation in Power VDMOSFETs in Radiation Environment," in booklet of RADECS, 1999.

[15] P.Habaš, D.Pantic, Z.Prijic and N.Stojadinovic, Technology CAD of low-power VDMOSFETs," in Proc. of CAS Sinaia (R), 501, 1994.

[16] N.Stojadinovic et al., "Analysis of gamma-irradiation induced degradation mechanisms in power VDMOSFETs," Microel.Reliab.35, 587, 1995.

[17] P.Habas and N.Stojadinovic, „Failure Mechanisms in Power MOSFETs in Radiation Environment," in Proc. INDEL, 1998. Published in Electronics 3(1), p.2, 1999.

[18] M. de la Bardonnie et al., "Characterization Method for Ionizing Radiation Degradation in Power MOSFETs," in Proc. of RADECS, 1995.

PROGRAM FOR SOFT START SQUIRREL CAGE INDUCTION MOTOR DRIVE SIMULATION

Zdravko Andonov, Teodor Dimitrov, Slobodan Mircevski
Faculty of Electrotechical Engineering, Karpos II b.b., P.O.B. 574, Macedonia
Phone: +389 91 399 149; Fax: +389 91 364 262
e-mail: zandonov@cerera.etf.ukim.edu.mk

Abstract: *Start-up process of induction squirrel cage motors can produce many problems to the working mechanism and to the other consumers. The easiest way for understanding start-up transients and examine the way how they could be suppressed is with computer simulation program. In the presented simulation program for education purposes start-up process with linear voltage change and voltage change with SCR are analyzed.*

Keywords: *induction motor start-up, soft start, simulation program*

INTRODUCTION

Start-up process of squirrel cage induction motor (SCIM) drive is very interesting specially because of transients which are happened in the machine and their influence to other electric energy consumers nearby. Start-up current is about (4 - 7) I_n and energy consumption due the start-up transients is also larger than steady state energy consumption. Oscillations and large starting values of electromechanical torque produce significance mechanical stresses in the machine and working mechanism.

Because of all this reasons implementation of soft start systems for SCIM electric drive is necessary. The term soft start means start-up of SCIM drive using some system which can deal voltage during the start-up in the way to limit starting current and motor torque.

For the better understanding and visualization of start-up process without and with soft starter is developed a school version of simulation program for squirrel cage induction motor drive soft start. The program is developed for Windows environment with VISUAL BASIC programming package. With this program can be calculated and SCIM drive characteristics can be shown in the desired period up to 5 min, what is very difficult to be done in a another way.

Induction motor model

For a correct dynamic simulation of SCIM electric drive start-up correct dynamic motor representation must be used. The most used is reference arbitrary frame theory of electrical machines. In this theory are make transformations of real three phase stator and rotor parameters (voltages, currents impedances, fluxes etc.) to their two phase representatives which are attached to axis with arbitrary speed of rotation.

When all induction motor currents, voltages resistances and reactances are transformed in two phase system the system of equations is:

$$\begin{bmatrix} v_{qs} \\ v_{ds} \\ v_{0s} \\ v'_{qr} \\ v'_{dr} \\ v'_{0r} \end{bmatrix} = \begin{bmatrix} r_s+\frac{p}{\omega_b}X_{ss} & \frac{\omega}{\omega_b}X_{ss} & 0 & \frac{p}{\omega_b}X_M & \frac{\omega}{\omega_b}X_M & 0 \\ -\frac{\omega}{\omega_b}X_{ss} & r_s+\frac{p}{\omega_b}X_{ss} & 0 & -\frac{\omega}{\omega_b}X_M & \frac{p}{\omega_b}X_M & 0 \\ 0 & 0 & r_s+\frac{p}{\omega_b}X_{ls} & 0 & 0 & 0 \\ \frac{p}{\omega_b}X_M & \left(\frac{\omega-\omega_r}{\omega_b}\right)X_M & 0 & r'_r+\frac{p}{\omega_b}X'_{rr} & \left(\frac{\omega-\omega_r}{\omega_b}\right)X'_{rr} & 0 \\ -\left(\frac{\omega-\omega_r}{\omega_b}\right)X_M & \frac{p}{\omega_b}X_M & 0 & -\left(\frac{\omega-\omega_r}{\omega_b}\right)X'_{rr} & r'_r+\frac{p}{\omega_b}X'_{rr} & 0 \\ 0 & 0 & 0 & 0 & 0 & r'_r+\frac{p}{\omega_b}X'_{lr} \end{bmatrix} \begin{bmatrix} i_{qs} \\ i_{ds} \\ i_{0s} \\ i'_{qr} \\ i'_{dr} \\ i'_{0r} \end{bmatrix} \quad (1)$$

Where:

- v_{qs}, v_{ds}, $v_{0s,}$ v'_{qr}, v'_{dr}, and v'_{0r} are the stator and rotor voltages in the arbitrary reference frame respectably.
- i_{qs}, i_s, $i_{0s,}$ i'_{qr}, i'_{dr} and i'_{0r} are the stator and rotor currents in the arbitrary reference;
- ω_b is base angular speed;
- p is diferencing element;
- X_{ss} is represented as $\mathbf{X_{ss} = X_{ls} + X_M}$
- X_{ss} is represented as $\mathbf{X'_{rr} = X'_{lr} + X_M}$
- X_{ls} and X'_{lr} are stator and rotor leakage reactances and;
- X_M is magnetizing reactance.

When stator and rotor current and fluxes are known motor electromagnetic torque T_e could be calculated as:

$$T_e = \left(\frac{3}{2}\right) p\, M \left(i_{qs} i'_{dr} - i_{ds} i'_{qr}\right)$$

where: p is number of pole pairs, M is mutual inductance and i_{qs}, i_{ds}, i_{qr} and i_{dr} are instantaneous currents in arbitrary reference frame.

When the equation of rotating movement is incorporated in the overall equations set than electric drive is possible to be simulated:

$$\frac{d\omega_r}{dt} = \frac{1}{J}\left(\frac{P}{2}\right)\left(T_e - T_l\right)$$

where T_l is load torque and J is drive inertia.

The equation set is consist of few non linear differential equation so the easiest way for their solution is implementation of one numerical methods. In our case is used fourth order Kunge-Kutta method.

Description of simulation program

Simulation program for squirrel cage induction motor drive soft start is developed for PC and it can be run under Windows 3.11 or higher. The program is developed using MS Visual Basic. The program is created to guide user to all needed data. For example if the user forget to choose load torque when he start the simulation, the screen with possible load torque appears before the simulation screen.

For the calculation in the program must be entered motor catalogue data and its resistances and reactances. Entered data could be saved for another simulation sessions.

In the simulation program there are following possibilities:

1. Different load torque: $M_l=0$; $M_l=const$; $M_l=k*n$; $M_l=k*n^2$; $M_l=k(n+c)$;
2. Value of load inertia and its real speed;
3. Starting method with starting value of voltage and its increasing time: direct start of drive; soft start with semi-controlled three phase SCR-diode bridge; soft start with full-controlled three phase SCR bridge and soft start with SCR bridge only in the one phase (unsymmetrical soft start);
4. Reference-frame angular speed (zero, rotor speed and flux speed);
5. Integration step and simulation time.

Motor drive setting

In the beginning, from menu, option for catalogue data must be chosen. The screen for manipulation with motor catalogue data is shown in ***Figure 1*** There are options for saving , editing and deleting of the catalogue data.

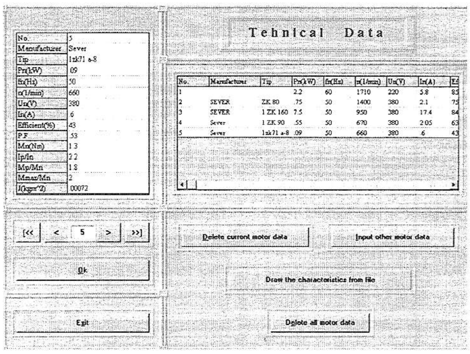

Figure 1. Input screen for a induction motor catalogue data

The next step is choice of load torque. Like the previous step, you can choose that option with simple click on the menu bar. After that you can see options for load torque selection and input screens for its arguments.

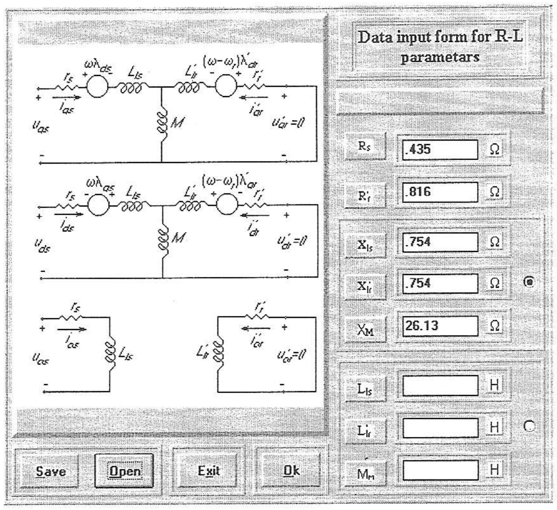

Figure 2. Input screen for equivalent circuit parameters

After that, the way of starting and the starting arguments must be chosen, if direct start is not simulated.

In the next step, optional, reductor parameters can be chosen. If there is no values for a reductor, program will imply that load is directly connected to rotor and it will warn it.

The last step is inputting the parameters of equivalent circuit. Input screen is shown in Figure 2. Equivalent circuit parameters could entered as inductance's or reactances and program automatically convert values. The equivalent circuit data can saved for a later use. With this motor drive setting are finished.

Simulation parameters setting

After, already described steps have to be set simulation parameters. When simulation button is clicked, simulation parameters input screen is shown in ***Figure 3***.

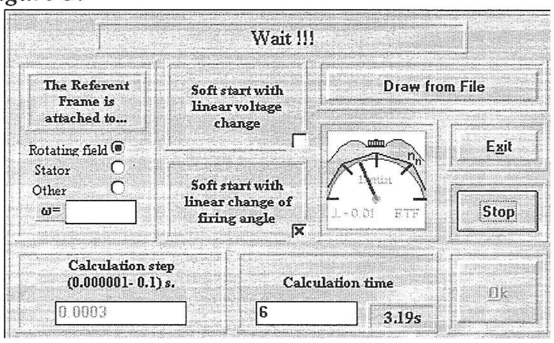

Figure 3. Simulation parameters input screen

In this screen has to be entered few options. One of them is attachment of reference frame. There are three option stator, synchronous speed or a arbitrary speed when relative speed must be entered.

The second option is stator voltage change. There is two possibilities linear maximal voltage change, or voltage change with firing angle of SCRs.

After this calculation step have to chosen. Calculation step can be chosen between 10^{-6} and 10^{-1} seconds. The last option which must be set is simulation time.

When all options are set with OK simulation is started. In every moment calculation can be cancel, if cancel button is clicked. On the simulation parameters input screen there is a tachometer which represents rotating speed change, as simulation goes on.

When all options are set with Button OK simulation is started. In every moment calculation can be cancel if cancel button is clicked. On the simulation parameters input screen there is a tachometer which represents rotating speed change, as simulation goes on.

When calculation is finished, information for that is shown on screen. When button OK is clicked the results manipulation screen is shown.

Manipulation with results

When calculations are finished results can be drawn on, printed or/and saved in ASCII form screen (Figure 4). The following characteristics vs. time could be shown: motor torque; load torque; motor supplied RMS voltage; motor RMS current; instantaneous value of motor current and motor efficiency

Each characteristic has a check box and checking it could be shown or hidden. On the form the is a cursor which presents values of the curves for cursor position time. For a better resolution characteristics can be zoomed.

All characteristics can be saved or printed using standard Windows printer options.

The saved characteristics could be load for a presentation which can be done in the few different screens in the program or for a use in the other software.

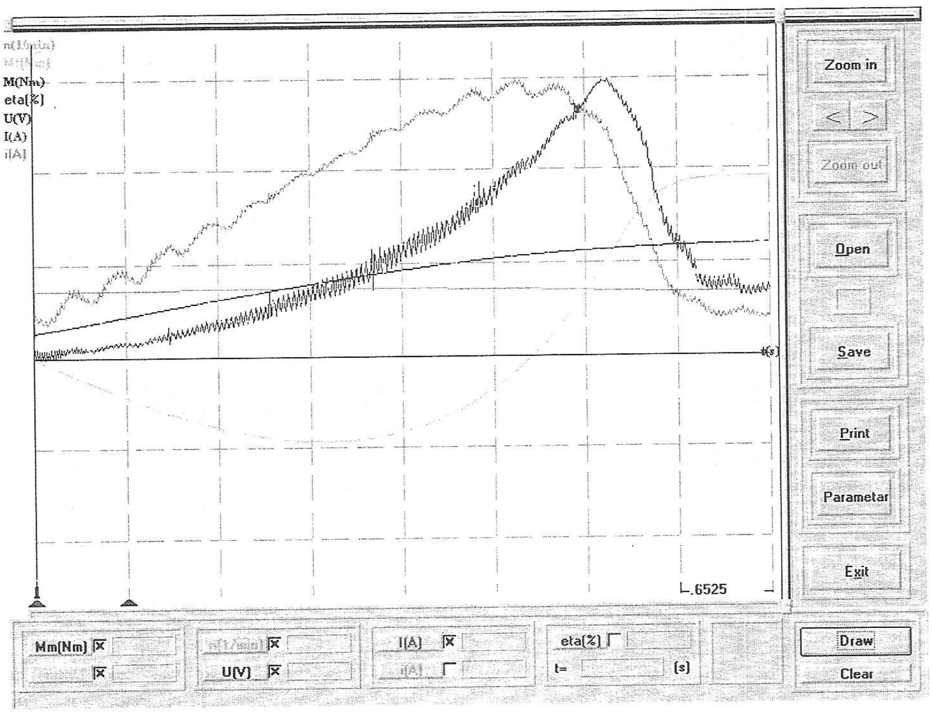

Figure 4. Screen for characteristics presentation and manipulation

Conclusion

With this simulation program, on easy and very fast way, students could be involved in SCIM drive start up transients, and solution of the problem with the soft start. Students could change motor, load and start-up techniques to learn more about SĆIM drive. Also, student could make simulation experiments to find a adequate technical problems for a different load torques and different start-up methods, and indirectly to find the best solution with the respect of economic reasons. All this is very difficult to be achieved in laboratory, because of limited financial, equipment and time.

We intend to develop this simulation program to became more powerful and universal for all type of rotating machines. In the first next step have to be included options for a wound rotor induction motor, then analyzes of DC motor and synchronous motors.

The basic disadvantages of all simulation methods are limitations of used mathematical model and no experience with the real equipment.

References

[1] P. Crause, O. Wasynczuk,S. Sudhoff, Analysis of Electrical Machinery, IEEE Press, Piscataway, 1994.

[2] J. R. Smith: Response analysis of AC. Electrical Machines, Research studies press LTD, Taunton England, 1990.

[3] T.Dimitrov, Dynamic simulation of squirrel cage induction motor drive soft start (diploma work), Faculty of electrical engineering - Skopje, 1996 (in macedonian).

[4] M. L. James, G. M. Smith, J. C. Wolford: Applied numerical methods for digital computation with FORTRAN and CSMP, IEP - A Dun-Donnelly Publisher, New York,1977.

[5] A. Dmitrovic, Z.Pondelec, Visual Basic, Znak, Zagreb, 1994 (in croatian).

CONTROL OF AC DRIVES WITHOUT SPEED SENSORS BY FREQUENCY COMPENSATION

Nebojša Mitrović, Borislav Jeftenić*, Milan Bebić*, Milutin Petronijević, Dragan Jevtić*

Faculty of Electronic Engineering, University of Nis
*Faculty of Electrical Engineering, University of Belgrade

Abstract: *Analysis of the PWM induction motor drive, where the regulation is made without the speed sensor, with the method of frequency compensation is presented in the paper. The control scheme is based on the well known V/f method. On the basis of the proposed method, the frequency compensation for the slip frequency and voltage drop compensation, being very important especially at the low speed range, is done. Slip frequency is determined on the basis of non-linear torque-speed dependence.*

1. INTRODUCTION

Induction motor drive based on full digital control is being applied in a great number of industrial application, begining from low cost drive to high performance. Great part of scientific efforts, in the last few yers had a goal of eliminating the speed sensor, saving good static and dynamic performances of a solution with speed sensors.

AC drives without speed sensor, according to the methods applied for speed regulation can be clasified in two groups: 1) low cost drive of general purpose, 2) high performance drive.

In the first group of drive some of the following methodology for speed calculation are used: slip frequency calculation method, constant volts-per-herts control, slot space harmonics, frequency compensation method [1].

In the second group the following methods are applied: speed estimation, model reference adaptive method, speed observers, Kalman filter techniques, neural nerwork based estimator [1]. Most of these method for speed estimation are carried out from methods applied in vector control techniques which had a purpose of determination of "inaccessable" quantities (flux and torque).

All of these methods are based on procedure which comprehends measurement of electrical stator quantities, directly or in DC link of the inverter with phase current reconstruction performed switching function and knowing motor parameters. However, in practice, simple, cheap and reliable drives are often needed, where it is possible to control speed, with modeset requests regarding dynamical features.

In this paper one of the slip compensation methods is analysed. The proposed control algorithm is based on frequency calculation by using air gap power estimation and nonlinear relationship between slip frequency and air gap power. Besides frequency compensation, the stator resistance voltage drop compensation is realized. The proposed control scheme requires motor name-plate data, the stator resistance value and instataneous stator current in two phases. The basic characteristics of the drive with the applied algorithm are the simplicity of the practical realization, fair steady state and transient characteristics, and the price not higher than the open loop frequency controlled drive.

2. FREQUENCY COMPENSATION

The criterion for the stator frequency selection for a given load and the reference speed is illustrated in Fig.1.

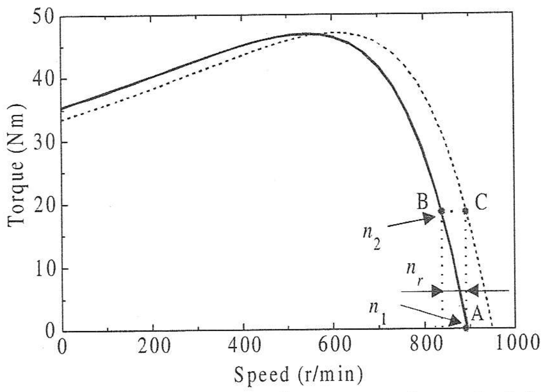

Fig. 1. The speed compensation principle

If the speed at no load was n_1 (point A), with the load increase operating point moves to the point B, with the speed "drop" of n_r. To compensate for the speed "drop", the controller increases the speed to $n_2 + n_r = n_1$ by means of increasing the frequency, thus moving the operating point to C. In this way, the actual speed is again equal to the reference speed n_1 from the point A.

2.1. Air-gap power estimation and voltage drop compesation

In order to implement this scheme it is necessary to know the relationship between load torque and slip. One of the possibilities is to assume a linear relationship between them [2]. Although this technique gives good results for high speeds its usefulness at low frequency and large torques is limited due to large steady state errors introduced by the linear approximation. To avoid above mentioned problem it is necessary to take into consideration non-linear torque-speed characteristic of the motor [4,5].

The Electrical Machine Theory establishes the relationship for the electromagnetic torque (M_m) and break down torque (M_{pr}):

$$M_m = \frac{2M_{pr}}{s/s_{pr} + s_{pr}/s} \qquad (1)$$

where s_{pr} is the slip at which the break down torque occurs.

Equation (1) is valid for any torque thus it is also valid for rated conditions. Defining $M_{pr}=\nu \cdot M_n$ and using (1) yields:

$$s_{pr}/s_n = k = \nu + \sqrt{\nu^2 - 1} \qquad (2)$$

which is the break down slip in per unit of the rated slip (s_n).

Substituing equation (2) into (1), the slip (s) required to produce electromagnetic torque M_m can be writen as:

$$s = k \cdot \nu \cdot M_n \cdot \frac{s_n}{M_m}\left[1 - \sqrt{1 - \left(\frac{M_m}{\nu} \cdot M_n\right)^2}\right] \qquad (3)$$

For the practical reasons we need to eliminate the load torque from equation (3). The elimination can be done by using equation (4):

$$M_m = (p/4\pi)P_{ob}/(f_m + f_r) \qquad (4)$$

where p is the number of poles, P_{ob} is the air gap power, f_r is the slip frequency, and f_m is the frequency which corresponds to the actual rotor speed.

Solving the equation (3) and (4) for the slip frequency can be obtained:

$$f_r = \frac{1}{2 - a \cdot P_{ob}}\left(\sqrt{f_m^{\,2} + \frac{k \cdot s_l}{2 \cdot \nu}P_{ob} - b \cdot P_{ob}^{\,2}} - f_m\right)$$

$$a = p/(4\pi k\nu M_n s_n f_n); \qquad b = (p/(4\pi\nu M_n))^2 \qquad (5)$$

When the ratio between the break down and rated torque is large enough, constants a and b become small and can be neglected. The physical explanation of this is that we have linear aproximation of mechanical motor characteristics, i.e the break down torque assume infinite value. For the linear dependence, in this case, for the slip frequency it can aproximately be writen as:

$$f_r \approx 1/2\left(\sqrt{f_m^{\,2} + s_l \cdot P_{ob}} - f_m\right) \qquad (6)$$

where $s_l = ps_n f_n/\pi M_n$.

Air gap power (P_{ob}) can be obtained by using expresion:

$$P_{ob} = 3V_s I_s \cos\varphi - 3I_s^{\,2} r_s - P_{Fe} \qquad (7)$$

To determine power P_{ob} it is necessary to know rms value of induction motor stator currents and active component of stator current. Assuming the symetrical sysytem, the rms current value can be obtained by measuring instataneous phase current as:

$$I_s = \sqrt{2/3} \cdot \sqrt{i_{as}(i_{as} + i_{cs}) + i_{cs}^{\,2}} \qquad (8)$$

The active stator current components can be obtained by qd transformation in synchronous reference frame as follows:

$$I_{s(\mathrm{Re})} = \sqrt{3}\{i_{ac}\cos(\omega t - \pi/6) - i_{cs}\sin(\omega t)\} \qquad (9)$$

The last term in equation (7) under variable frequency operation is difficult to obtain but it can be approximated from the knowledge of rated values and constant flux operation. It can be easily shown that the core losses for nominal load:

$$P_{Fen} = P_{u\ln}(1 - \eta_n/(1 - s_n)) - 3I_{sn}^{\,2} r_s \qquad (10)$$

Core losses can be devided into two components [3]:

$$P_{Fen} = K_h B_n^{\,2} f_n + K_e B_n f_n^{\,2} \qquad (11)$$

where K_h i K_e are coeficient which depend of core type, B_n is rated flux density.

For constatnt flux operation these losses only vary with frequency. Assuming that at rated conditions both components are equal, after some manipulation, the total core loss at any frequency can be writen in terms of its rated value as:

$$P_{Fe} = \frac{1}{2}\left(\frac{1+s}{1+s_n}\left(\frac{f_s}{f_n}\right) + \frac{1+s^2}{1+s_n^{\,2}}\left(\frac{f_s}{f_n}\right)^2\right)P_{Fen} \qquad (12)$$

Substituting (12) into (7) gives air gap power as a function of reference frequency and measured variables. The slip measurement required in (12) is obtained from (5) or (6).

Voltage drop compensation can be obtained by keeping magnitude of the leakage stator flux at the constant and rated value. Based on the phasor diagram shown in Fig.2 it can be writen:

$$V_s = I_s r_s \cos\varphi + \sqrt{(V_{s0} f_s/f_n)^2 - (I_s r_s \sin\varphi)^2} \qquad (13)$$

where with V_{s0} is marked amplitude of E_m at rated frequency f_n. The value for E_m needed for constant flux keeping (V/f=const.) at any another frequency f_s can be obtained as:

$$E_m = V_{s0} \cdot f_s / f_n.$$

For implementation of equation (13) the value of rms stator current I_s is needed like its active components which can be obtained based on the equations (8) and (9). Final expression for stator voltage at any frequency based on the instantaneous measurements of motor current is:

$$V_s = \frac{\sqrt{2}}{3} \cdot I_{s(\mathrm{Re})} r_s + \sqrt{\left(\frac{V_{s0} f}{f_n}\right)^2 + \frac{2}{9}\left(I_{s(\mathrm{Re})} r_s\right)^2 - \left(I_s r_s\right)^2} \tag{14}$$

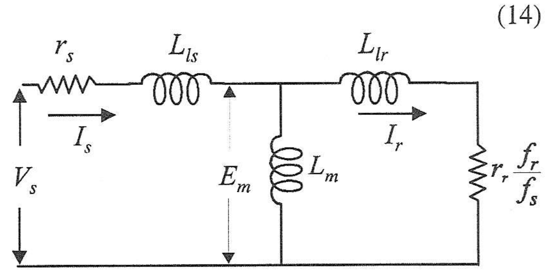

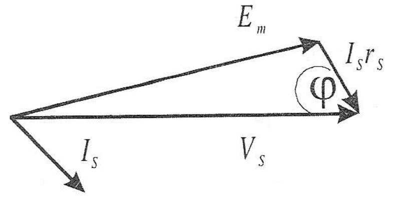

Fig. 2. Induction motor eqivalent circuit and phasor diagram

3. SIMULATION AND EXPERIMENTAL RESULTS

In Fig.3 the block diagram of the drive is shown so that the basic idea of applied speed regulation modus can be seen. Due to existing positive feedback at frequency compensation and voltage it is necessary to stabilize the system by using low-pass filter in the feedback loop. The proposed speed control method is first analysed by computer simulation on a detailed drive model, and than by the experimental results obtained on laboratory model.

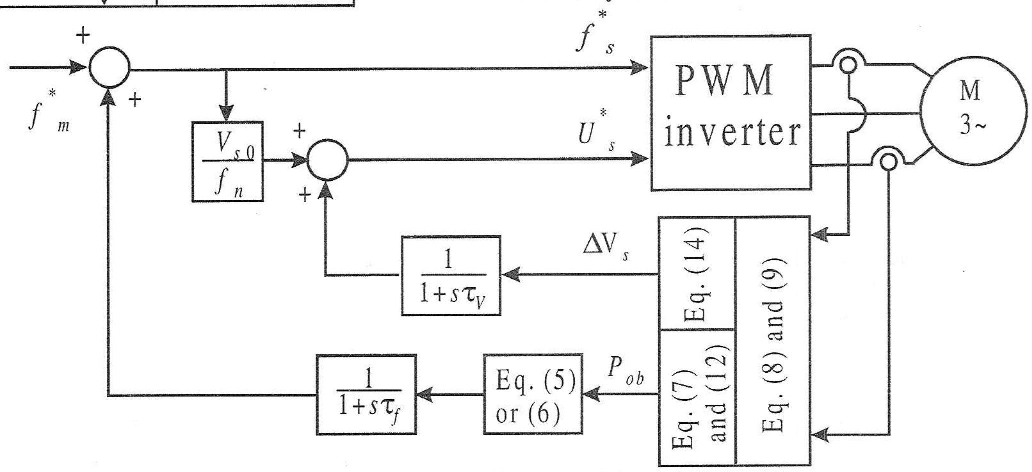

Fig. 3. Block diagram of the drive

Simulation results are obtained by using PSpice program package. In Fig.4 simulation results obtained for reference speeds of 200, 600 and 1000 r/min are shown. First, drive system operated at the no-load while load torque in stedy state was 50% of rated torque. The speed regulation effect with and without speed regulation is illustrated in Fig.4. In it the moment of switching off regulation is clearly marked, resulting in speed reduction. Dependence of the load torque versus time is also shown in figure.

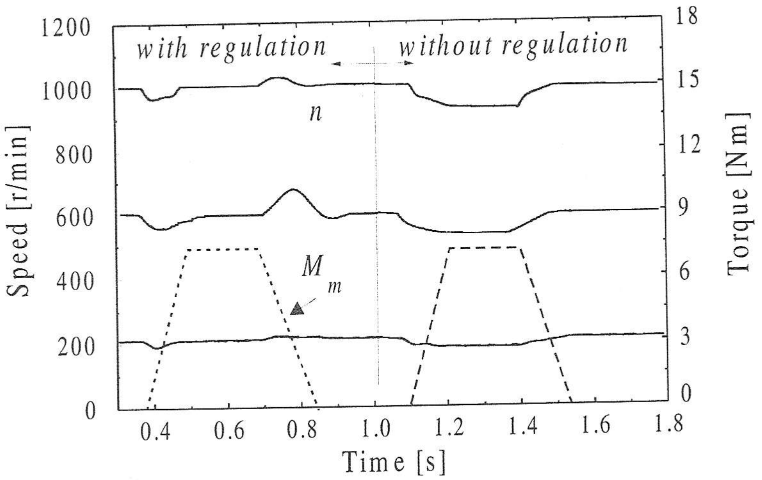

Fig. 4. Speed response. Simulation results.
(n_{ref}=200; 600; 1000 r/min)

Experimental verification of the proposed algorithm were made on the induction motor drive; its parameters are given in appendix A. Motor load was performed by the separately excited DC motor in dynamic braking regime. In Fig. 5 and 6 steady state speed-torque characteristics for different reference speed values in range of 100-1800 r/min are shown. The drive ability for keeping reference speed even at a very low speed is obvious.

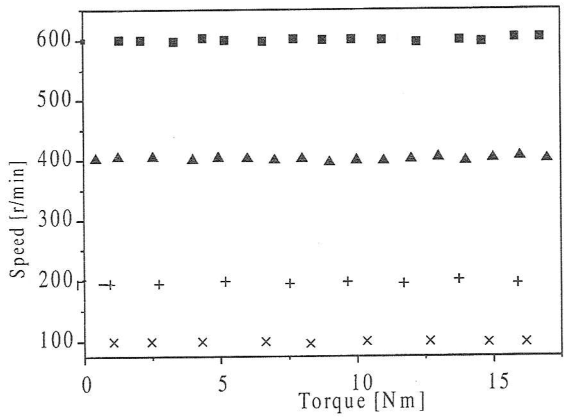

Fig. 5. Steady state speed response.
Experimental results (n_{ref}=100 ÷ 600 r/min)

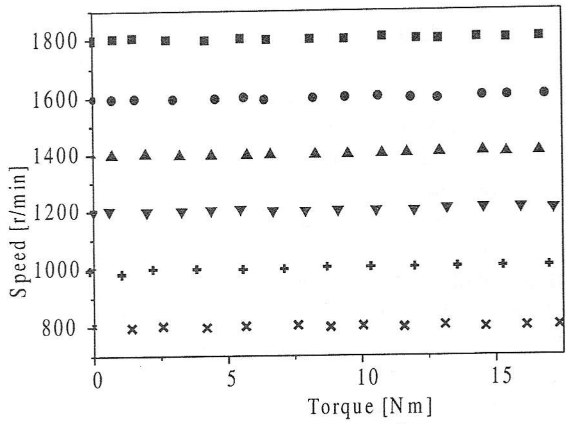

Fig. 6. Steady state speed response.
Experimental results (n_{ref}=800 ÷ 1800 r/min)

The dynamic characteristics of the drive are presented in Fig.7 showing the response of the system to the change of reference speed and load change. First, the drive operated at no load at the speed of 200 r/min. At the moment related to point A the change of reference speed at 600 r/min had been done, so that the drive at the moment related to the point B was loaded. Afterwords at the point C the reference speed of 1000 r/min was changed, and at point D no-load resulted.

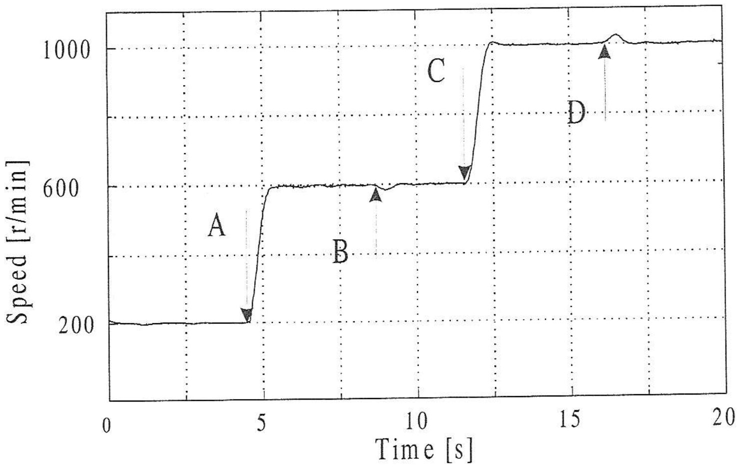

Fig. 7. Speed respons,. step change of reference speed and load. Experimentla results

4. CONCLUSION

Induction motor drive frequency compensation method based on V/f control has been presented. The proposed compensation method requires the knowledge of motor nominal data, stator resistance and motor stator currents measurements. The control algorithm can be simply implemented in the existing drives which use the clasic V/f control. By the theoretical and experimental analysis, the applicability of the frequency compensation method for drives with modest dynamic characteristics has been confirmed.

Appendix A

Induction machine data: 1,5 kW; 50Hz; 930 r/min; 220V; 4A; cosφ=0,8.

r_s=4Ω; r_r=3,4Ω; L_{ls}=0,01383H; L_{lr}=0,01383H; L_m=0,245 H

5. REFERENCES

[1] K. Rajashekara, A. Kawamara, K. Matsuse, “Sensorless Control of AC Drives”, IEEE Press, 1996.

[2] A. Garcia, T. Lipo, D. Novotny “A New Induction Motor Open-Loop Speed Control Capable of Low Frequency Operation” Annual Meeting, New Orleans, Oct.1997. pp. 121-128.

[3] D. Novotny, S. Nasar, B. Jeftenic, “Frequency Dependence of Time Harmonic Losses in Induction Machines”, ICEM, Boston, July 1990.

[4] Nebojša Mitrović, “Regulacija brzine asinhronog pogona sa PWM invertorom kompenzacijom učestanosti bez senzora brzine”, Doktorska Disertacija, Elektronski fakultet, Niš 1998,

[5] B. Jeftenić, N. Mitrović, M. Bebić, “A Simple Speed Sensorless Control For Variable Frequency Induction Motor Drive”, IEEE Trans. on Energy Conversion, Vol.14, No.3, Sept.1999.

INFLUENCE OF MAGNETIC NONLINEARITY AND "DEATH TIME" EFFECT IN *SENSORLESS* DRIVES

Petar Matić, Veran Vasić*, Radiša Jevremović*
Faculty of Electrical Engeneeringt, Banja Luka, Republic of Srpska

**Faculty of Technical Sciences*, Novi Sad, Yugoslavia

Abstract: *This paper deals with mathematical methods which can be used for analyzing the magnethical non-linearity and dead-time effect in sensorless drive. Those models are united with model of sensorless drive for computer simulation, and results of simulations are presented. There are suggested methods for minimizing those influences.*

Key Words: *Sensorless Drive/Influences/Magnetical non-lenearity/Dead-time effect*

1. INTRODUCTION

The greatest number of electrical drives are so called midle performance drives. In these drives it is not necesary to position shaft and to control angular velocity precisely. In these drives velocity and torque have to be independently controled, to be as cheep as possible and robust. That is the reason why these drives are realised as indirectly vector controled drives with induction machines (sensorless dives). Angular velocity, torque and flux are estimated. Estimation error is influenced by motor parameters.

Common sensorless drive is presented in this paper. Speed estimation is based on MRAS (Model Reference Adaptive System) algorithm. Control subsystem mathematical model is developed in stationary reference frame while mothor subsystem is presented with mathematical model in synchronous reference frame. In mathematical models of drives flux saturation and death time is typicaly ignored.

In this paper is shown how this aproximations influence estimation quality. This is done by computer simulation. Possibilities for elimination of these influences are suggested as a result of this work.

2. INFLUENCE OF MAGNETICAL NON-LINEARITY

State space model of induction machine is usually developed on assumption of linear relationship between flux and current. To conduct qualitative analyse of the transition phenomena in induction machine connected to inverter; it is necessary to account magnetic saturation.

Working point of the machines is positioned on the knee of the magnetic characteristic in the process of machine construction. (From this point magnetic material is saturated.) Reason for this is to maintain maximum possible use of ferromagnetic material. For induction machines fed by power electronic converters working regime is such that magnetic core is deeply saturated. Because of it mathematical model of machine where magnetic nonlinearity is not taken into consideration is highly inadequate (produces significant error).

For magnetic saturation to be accounted it is necessary to express stator and rotor fluxes as combination of the lequage and magnetising flux [1]. Mathematical model of the machine becomes:

$$\Psi_d = L_s i_d + L_m i_D = L_{\gamma s} i_d + \Psi_{dm}, \tag{1}$$

$$\Psi_q = L_s i_q + L_m i_Q = L_{\gamma s} i_q + \Psi_{qm}, \tag{2}$$

$$\Psi_D = L_r i_D + L_m i_d = L_{\gamma r} i_D + \Psi_{dm}, \tag{3}$$

$$\Psi_Q = L_r i_Q + L_m i_q = L_{\gamma r} i_Q + \Psi_{qm}, \tag{4}$$

Cappital letters in subscript are used for rotor and small letters for stator varaiables. Stator and rotor inductances are expressed as sum of the lequage and mutual inductances:

$$L_s = L_{\gamma s} + L_m, \tag{5}$$

$$L_r = L_{\gamma r} + L_m. \tag{6}$$

D and q components of the mutual fluxes, Ψ_{dm} and Ψ_{qm}, are defined by:

$$\Psi_{dm} = L_m(i_d + i_D) = L_m i_{dm}, \tag{7}$$

$$\Psi_{qm} = L_m(i_q + i_Q) = L_m i_{qm}, \tag{8}$$

and mutual flux is given with:

$$\Psi_m = \sqrt{\Psi_{dm}^2 + \Psi_{qm}^2}. \tag{9}$$

Magnetizing current (d and q components) are given with:

$$i_{dm} = i_d + i_D, \tag{10}$$

$$i_{qm} = i_q + i_Q, \tag{11}$$

and total value of magntizing current is:

$$i_m = \sqrt{i_{dm}^2 + i_{qm}^2}. \tag{12}$$

Standardly constructed inductance machine has cilindrical rotor, so mutual induction L_m is same for both axes (d and q) in saturated as well as in unsaturated working regime:

$$L_m = \Psi_m / i_m, \tag{13}$$

$$L_m = L_m(i_m). \tag{14}$$

Magnetising curve obtained by approximation using minimum square method is used in this paper [2]. Obtained relationship is expressed by table of flux or mutual inductance in function of magnetising current. Such tables are easy to be modelled in simulation programs.

Influence of saturated lequage fluxes exists as well and it is not included in above relations However, this influence is not very important, so it can be neglected.

2.1. Simulation of drive operation with magnetic nonlinearity modeled

A way to include magnetic saturation in induction motor model is explained so far. Magnetizing current is calculated from dq components of current, which are known (relations (10) to (12)). After magnetizing current being calculated, adequate value of mutual inductance is obtained from Lookup table given in Apendix. In this way nonlinearity of the magnetic core is modeled although estimating models are obtained assuming that magnetic core is linear.

In Figure 1 results of simulation are presented. In this case drive operation on 15 rad/s rate is simulated. Machine starts unloaded and in 0.1 sec. speed reference is given. After 0.4 sec., when transient regime is finished, machine is loaded with 50% and in 1 sec. load is set to 100%.

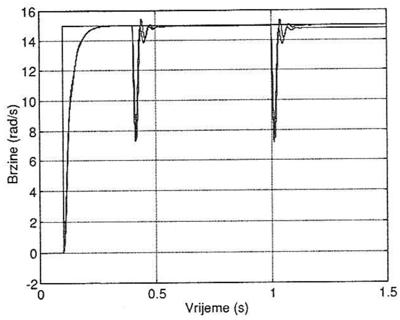

Figure 1a – Speed reference, real and estimated speed

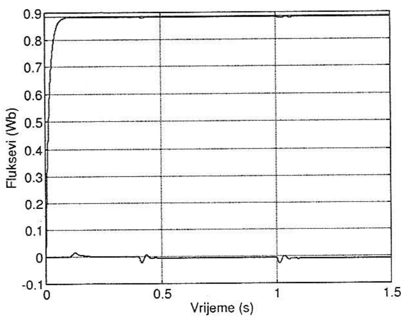

Figure 1b – Rotor flux

Figure 1 shows speed reference, real and estimated speed. Estimated and real speed differ as consequence of the magnetic nonlinearity. This error increases if motor load is increased. Since speed regulator has estimated speed on feedback it is logical that there is no steady state difference beetwene estimated and reference value of speed. In the Figure 1b stator and rotor fluxes are shown. There is an error in q component of flux so iti is not equal to zero which is condition to have vector controled drive.

2.2. Proposition for elimination of magnetic nonlinearity influence

Magnetic nonlinearity leads to an error in speed regulation. This error can be eliminated if estimator model is upgraded so that mutual inductance is evaluated from Lookup table as function of magnetising current calculated according to relations (10) to (12). Obtained in this manner mutual inductance is parameter for speed estimator.

3. INFLUENCE OF "DEATH" TIME

"Death" time is time in which semiconductor components in inverter bridge chance from one to another state. During "death" time both semiconductor switches in an inverter leg have to be turned off, which makes bridge uncontrollable. Output voltage polarity is defined by current orientation and output voltage value is defined by DC circuit voltage. Flywheel diodes conduct current during the "death" time period. Since motor voltage has impulse shape during the "death" time, its mean value is obtained [3].

$$U_D = U_{DC}\frac{t_\Delta}{T_s}, \tag{15}$$

Where used symbols are:

U_D - equivalent voltage during the "death" time,

U_{DC} - DC circuit voltage,

t_Δ - duration of "death" time,

T_s - commutation period.

Equivalent "death" time voltage, (15) is added or subtracted from phase voltage depending on current orientation:

$$u_a' = u_a - U_{DC}\frac{t_\Delta}{T_s}\operatorname{sgn}(i_a), \tag{16}$$

$$u_b' = u_b - U_{DC}\frac{t_\Delta}{T_s}\operatorname{sgn}(i_b), \tag{17}$$

$$u_c' = u_c - U_{DC}\frac{t_\Delta}{T_s}\operatorname{sgn}(i_c), \tag{18}$$

Where symbols are:

$u_{a,b,c}$ - phase voltage on the output of inverter with ideal switches,4

$u_{a,b,c}'$ - phase voltage with uncalculated "death" time,

$i_{a,b,c}$ - phase currents.

In order to obtain mean value of "death" time voltage drop it is necessary to know value of "death" time duration t_Δ, which is approximately 10ns (according to catalogue data), as well as switching period T_s. Power electronics converter is usually current regulated voltage inverter with hysteresis. Such configuration draw back is that switching period T_s is not constant during the output current period, and its value is different for all three phases in the same moment. Determining exact value of switching period is highly complex procedure and for accurate mathematical solution it is necessary to consider influence of many parameters such as ambient temperature and load current, on "death" time value. However, for "death" time effect to be qualitatively analysed it can be assumed:

1. It is going to be observed worst case, i.e. case when switching period is shortest (switching frequency highest) because then "death" time influence on drive control is strongest;
2. "Death" time in every phase has the same impact on control quality;

Considering first assumption it can be considered that switching period is constant and consequently value t_Δ/T_s will be constant. Consequence of the second assumption is that value t_Δ/T_s will be same for all three phases.

It will be assumed that t_Δ/T_s has value of about 1%, and "death" time effect will be accounted through constant voltage which will be added or subtracted from phase voltage in function of current orientation as it is shown in relations (16) – (18).

3.1. Simulation of drive operation with accounted "death" time

Block in which "death" time effect is modelled is included in induction machine model, but not in control model. Simulation results are shown in Figure 2.

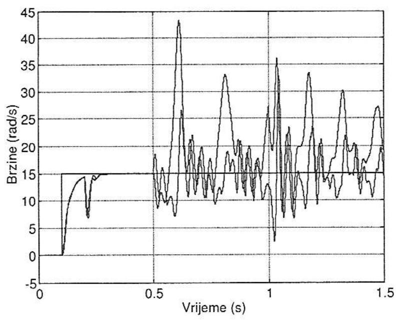

Figure 2a – Speed reference, real and estimated speed

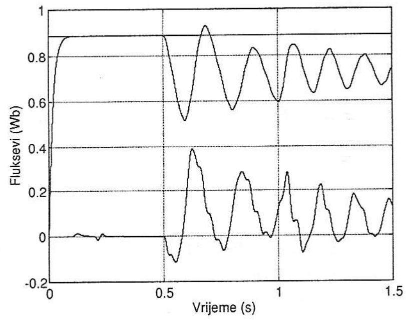

Figure 2b – Rotor fluxes

Induction machine is unloaded on startup. In 0,2s induction machine is loaded with 50% of nominal torque. In 0,5s "death" time effect simulation starts. It is obvious from Figure 2a that speed responce is oscilatory when "death" time is modeled. After 1s nominal load of machine is modeled. In Figure 2a it can be seen that speed response remains oscilatory when load is incresed. Figure 2b shows rotor fluxes which are oscilatory as well.

From simulation results it cam be concluded that "death" time effect has great influence on sensorless drive performance, especialy on low speed. To ovecome this effect it is necesary to use faster switching components in order to decrease death time duration.

"Death" time influences drive performance on nominal speed too. This influence in nominal regime has much less intensity.

4. LITERATURE

[1] E. Levi: Vector control of Induction machines considering magnetic saturation, *Ph. D. Thesis,* Belgrade University, Belgrade 1990. (in Serbian)

[2] M. Božić, V. Martinović: Simple Aproximation of Induction Machine Magnetic Curve, Power Electronics, VIII Symposium, Novi Sad, 27-29. IX 1995. (in Serbian)

[3] Slobodan N. Vukosavić, Milić R. Stojić: On - Line Tuning of the Rotor Time Constant for Vector – Controlled Induction Motor in Position Control Applications, *IEEE Transactions on Industrial Electronics, vol. 40, NO. 1, February 1993.*

5. APENDIX

Nameplate data of the induction machine are:

TYP ZK – 80	Nr 471458/83
3 MOT	Δ220/Y380V
3,6/2,1 A	0,75 kW
$\cos\varphi = 0{,}72$	1390 o/min
50 Hz Izl. kl. B IP 54 B3	

Parameters of this machine are:

$R_s = 10\Omega$

$R_r = 6{,}3\Omega$

$L_{\gamma s} = 43{,}067mH$ $L_{\gamma r} = 40{,}107mH$

$L_{mn} = 0{,}4212H$

$J = 0{,}00442kgm^2$

Through no load experiment pairs of current and flux values are measured. On the base of these experimental results approximated magnetic curve is calculated [2]. These approximated values are summarised in table P.1.

Table P.1. – Approximated magnetic curve in table format: effective values of flux and magnetic current, magnetic current value in dq reference frame and mutual inductance

I_{meff}	Ψ_{meff}	i_m	L_m
0	0		0,612
0,5	0,306	0,707	0,612
0,75	0,425	0,61	0,567
1,35	0,615	1,909	0,456
1,875	0,667	0,652	0,356
14,14	0,848	19,997	0,06

EXPERIMENTAL SURVEY OF THE MOTOR REFERENCE CURRENT CORRECTION UNDER THE VECTOR CONTROL

Aleksandar Nikolic, Energoprojekt ENTEL L.L.C., Belgrade, Yugoslavia, nba@ieee.org
Borislav Jeftenic, Faculty of Electrical Engineering, Belgrade, Yugoslavia, jeftenic@etf.bg.ac.yu

Abstract: *In the paper, the experimental survey of the motor current correction in the vector controlled CSI fed induction motor drive is presented. In this drive a thyristor type current source inverter is used. The complete control is implemented in the Intel's 16-bit 80C196KC20 microcontroller. The control algorithm, based on vector control with the rectifier reference current correction, is accomplished by software written in C language. All results that are obtained by a experiment confirms the accuracy of the proposed current correction and shows the advantages of the realized drive related to the vector controlled drive known in the literature.*

INTRODUCTION

Vector controlled induction motor drives with thyristor type current-source inverter (CSI) are interesting for the researches and development because of its robustness and easy power regeneration to the supply network under the breaking conditions, what is favor in a large-power induction motor drives.

But, for the nature of the CSI operation, the needed dynamic performances that exist in PWM inverter drives are not achieved with the known vector control algorithms. In the examples of vector controlled CSI drives that could be found in [1]-[6] the problems of the speed response are reported. This is influenced by the instantaneous phase error and, as a result, this configuration has slower torque response compared to the current regulated PWM drive. In addition to the phase error, the commutation delay is inhered in CSI operation and must be generally compensated to achieve acceptable vector control.

In the drive used in this paper (induction motor fed by a CSI) mentioned problems are avoid with new vector control algorithm [7]-[9]. The main advantage of the suggested algorithm compared to the known from literature is better dynamic performances of the proposed CSI drive. This enhancement rely on the fast changes of the motor current, without phase error, similarly to the control of current regulated voltage source PWM inverter. The realized CSI drive has more precisely vector control, accomplished by the implemented prediction of the reference current. The suggested algorithm produces the same dynamic performances of the CSI drive that exist in the other vector controlled drives [9].

The paper reviews the specific experiment intended to show the accurate vector control in the induction motor drive with applied reference current correction.

On the Fig. 1 the simplified scheme of the realized drive is shown, and software structure of the motor speed regulation is presented on Fig.2.

REFERENCE CURRENT CORRECTION

In the vector controlled induction motor drive fed by a CSI exist a problem of incorrect copying of the d-q references to the motor. The reason is non-sinusoidal current waveform produced by a CSI. The ideal CSI current with neglected commutation and DC link current pulsation is quasi-square waveform. Fourier analysis of this waveform gives the expression [1]:

$$i_a = \frac{2\sqrt{3}}{\pi} \cdot I_d \cdot \left(\sin(\omega t) - \frac{1}{5}\sin(5\omega t) - \right.$$
$$- \frac{1}{7}\sin(7\omega t) + \frac{1}{11}\sin(11\omega t) +$$
$$\left. + \frac{1}{13}\sin(13\omega t) - \ldots \right) \tag{1}$$

From the previous relation it could be seen that the fundamental component of AC output current has amplitude 10 percent greater than amplitude of DC link current $\left(2\sqrt{3}/\pi \cdot I_d \approx 1.1 \cdot I_d\right)$. For that purpose, a fine-tuning of the motor currents in d-q frame is performed. The corresponding relation is made between the mean values of the motor currents in d-q frame and the commanded d-q currents. For proposed correction it is not sufficient to use the difference between currents of 10% from (1), because the correction depends on the phase angle of the d-q components and the inverter commutation process. At lower speed, the commutation process could be neglected since it is much shorter than the motor current cycle. Taking all this in consideration, at first the rectifier reference current is corrected concerning the reference amplitude, the phase angle and the commutation duration. The rectifier reference current formed in that manner is now introduced to the current controller to obtain a suitable motor d-q currents and achieve desired vector control. To explain this technique, it should be started from the fundamental reference current obtained on the resolver output (see Fig. 2):

$$i_s^* = \sqrt{(i_{sd}^*)^2 + (i_{sq}^*)^2} \quad (2)$$

The amplitude of the motor current vector in polar coordinates could be determined in the same way as the fundamental reference current calculated from (2), using the average values of d-q currents:

$$i_s(\theta_s) = \sqrt{i_{sd_{av}}^2(\theta_s) + i_{sq_{av}}^2(\theta_s)} \quad (3)$$

The correction factor is introduced as relation between reference current obtained from (2) and actual motor current calculated from (3):

$$K(\theta_s) = \frac{i_s^*}{i_s(\theta_s)} \quad (4)$$

The corrected rectifier reference current that provide preferred values of motor current d-q components is now:

$$i_{s\_ref} = K(\theta_s) \cdot i_s^* \quad (5)$$

After the correction is applied, the stator d-q currents mean values will be equal to the corresponding d-q references. The accuracy of this correction is approved from calculation as shown in [7], and the needed precision of the vector control algorithm is proven in [7] and [8] by simulation of the drive model in *Matlab SIMULINK* software.

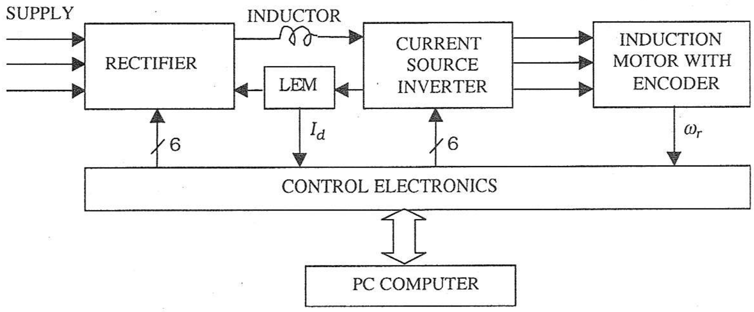

Fig. 1. *Block diagram of the current converter fed induction motor drive*

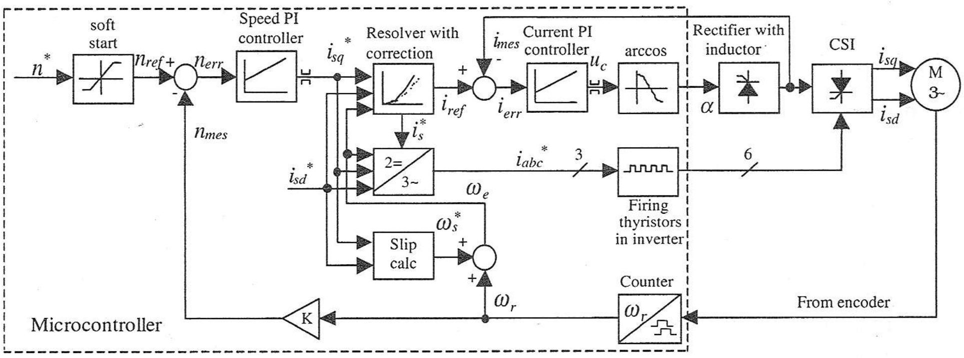

Fig. 2. *Speed control of the induction motor drive fed by a CSI*

IMPLEMENTATION

The realized induction motor drive has a standard thyristor type frequency converter (three-phase bridge rectifier, dc link inductor and autosequentially commutated inverter). All functions of the drive including the vector control are accomplished by the Intel's 16-bit microcontroller 80C196KC20 and its peripherals [9]. The speed control of the drive is fully accomplished by software written in C and implemented in the microcontroller, as presented on Fig. 2. Program modules are maximally optimized to obtain effective code, equivalent to the corresponding one written in the assembler [9].

Correction given by (5) is developed in the software as a lookup table calculated in Matlab for all possible values of isq* with isd* maintained constant.

Motor stator current could be expressed in the two-phase *d-q* reference frame with the following equations:

$$i_{sd} = -1/\sqrt{3} \cdot (i_a + 2 \cdot i_b) \cdot \cos(\theta_e) + i_a \cdot \sin(\theta_e) \quad (6)$$

$$i_{sq} = 1/\sqrt{3} \cdot (i_a + 2 \cdot i_b) \cdot \sin(\theta_e) + i_a \cdot \cos(\theta_e) \quad (7)$$

From (6) and (7) it could be observed that d and q current components are known from two motor phase currents (i_a and i_b) and angle θ_e between the a-axis of the three phase system and d-axis of two phase d-q system. Phase currents i_a and i_b are measured directly on the motor with current probes.

The angle θ_e is obtained in the control algorithm as a result of a digital integration:

$$\theta_e(k) = \theta_e(k-1) + \omega_e \cdot T_s \tag{8}$$

where k is a sample, T_s is sample time and ω_e is excitation frequency. The integrator is reset every time when θ_e reaches 0 or 360 degrees.
The excitation angle could be measured/detected in a several ways:

- by sending the angle value via serial channel, what is slow for this purpose,
- by sending the angle value to the special D/A converter, what needs additional hardware,
- and by changing state of the one microcontroller's digital output at the instants when the integrator is reset (the time between two resets correspond to the angle change from 0 do 360 degrees).

In this experiment the third way is used, because there is no need for additional hardware and it gives good results. For the measurements, a four channel digital storage scope with GPIB interface and two current probes is used, PC computer with GPIB card and a program written in *Matlab* for automatic data acquisition from the scope. The complete hardware used in this experiment and the way of collecting data is shown on Fig. 3.

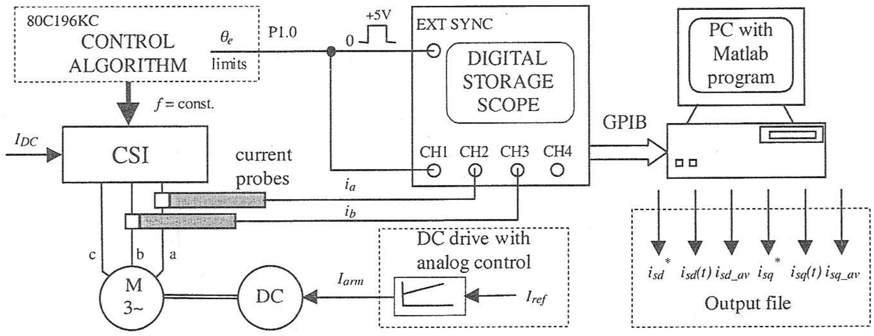

Fig. 3. *Experimental setup for the stator current components detection*

- The changes of the angle integrator are detected by alternating the state of the one microcontroller's digital output (Port 1) from 0 to +5V and vice versa. This port is connected to the oscilloscope's external synchronization input. The output results from the scope are stored in two ASCII files. In the first file the time base, the motor current in a-phase and the time instants of the angle integrator resets are saved, while in the second file the time base and the motor current in b-phase are saved. To improve this experiment, the automatic procedure that relies on the Matlab program is developed. By this program the input values are at first filtered, then the particular angle range is found and at the end, the instantaneous and average values of the stator current components are computed from relations (6) and (7). This procedure is also repeated with the control algorithm without current correction. From these values the averages are computed in the particular angle range and compared by the corresponding references.
- The DC link current is measured by a 10-bit A/D converter integrated in the microcontroller [9]. This is the reason why reference current is also represented in the 10-bit notation. The scaling factor needed for translation of the measured current to its 10-bit equivalent is calculated from the A/D converter characteristics and the measuring range. For this drive this factor is:

$$\boldsymbol{K_{A/D} = 33.759} \tag{9}$$

The reference current in d-axis (i_{sd}^* = 2,962A) is calculated for this drive using (9), what is equal to 100 processor units in the 10-bit notation (the range is from 0 to 1024 p.u.). The torque command (q axis current) is changed in the range from 50p.u. to 110p.u. directly (the speed controller from Fig. 2 is disabled). The inverter output frequency is retained same during experiment (about 10Hz) by varying the DC motor armature current. This current is controlled by the thyristor drive with analog control electronics. In this way, because of the low inverter frequency, the inverter commutation could be neglected as done in the correction lookup table.

EXPERIMENTAL RESULTS

On Fig. 4 the instantaneous values of d and q currents are shown for one given torque reference (i_{sq}^* = 60p.u. = 1.7773A, i_{sd}^* = 100p.j. = 2.9622A). On Fig. 5 and Fig. 6 the references are compared to the corresponding real values of d and q components with and without correction. From these figures it could be clearly seen that differences from the references are greater in the cases when correction is not performed. When the correction is applied, the differences are very small and they are only result of:

- neglected commutation (not important in the speed range in which the experiment is performed), and
- neglected pulsations of the current in DC link.

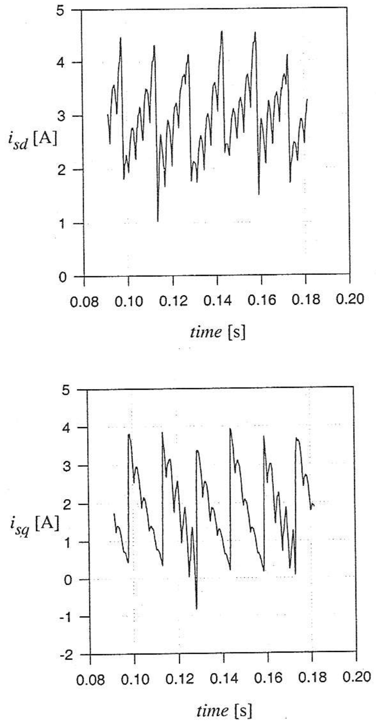

Fig. 4: *The motor instantaneous d and q currents*

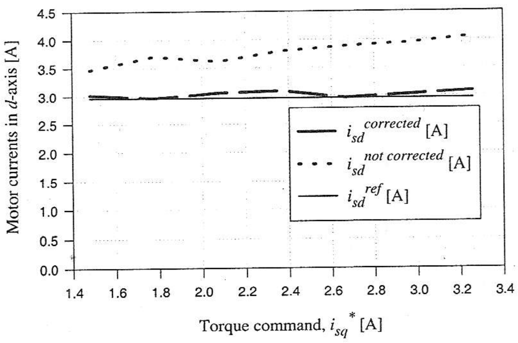

Fig. 5: *References and average values of d-axis currents with and without correction*

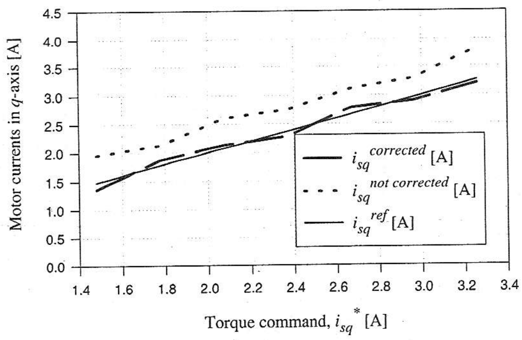

Fig. 6: *References and average values of q-axis currents with and without correction*

CONCLUSION

This paper reviews the experimental verification of the necessity for application of the rectifier reference current correction in the vector controlled induction motor drive supplied by current source converter. Additionally, the accurate and simple method for estimation of the excitation angle is also presented in the experiment. The results obtained from this experiment shows that precisely vector control is achieved. Thanks to the implemented correction of the rectifier reference current, d and q components applied to the motor are nearly equal to the given references. In this way the increase of motor flux and possible machine saturation is avoid, because the value of flux current component (d-axis current) without correction is greater than its rated value. In the further researches authors plan to develop the suggested correction with the neural network and use the real waveform of the inverter current.

BIBLIOGRAPHY

[1] Winsconsin Electric Machines and Power Electronics Consortium, Field Orientation and High Performance Motion Control, Summary of publications 1981–1988, Madison, 1990.

[2] J.M.D.Murphy, F.G.Turnbull, Power Electronic Control of AC Motors, Pergamon Press, Oxford, 1988.

[3] B.K.Bose, Power Electronics and AC Drives, Prentice-Hall, New Jersey, 1986.

[4] B.K.Bose (Editor), Microcomputer Control of Power Electronics and Drives, IEEE Press, New York, 1987.

[5] V.R.Stefanovic, R.M.Nelms (Coeditors), Microprocessor Control of Motor Drives and Power Converters, IEEE Press, New York, 1994.

[6] P.Vas, Vector Control of AC Machines, Clarendon Press Oxford, New York, 1990.

[7] A.B.Nikolic, B.I.Jeftenic, "The New CSI Control Strategy for Avoiding Slow Response in Vector Controlled Induction Motor Drive", Proceedings of the 7th Conference EPE'97, vol. 3, pp. 842-847.

[8] A.B.Nikolic, B.I.Jeftenic, "The New Algorithm for Vector Controlled CSI Fed Induction Motor Drive", Proceedings of the 8th Conference PEMC'98, vol. 5, pp. 143-19.

[9] A.B.Nikolic, B.I.Jeftenic, "A Microcontroller Based Control of Current Source Converter Fed Reversing Induction Motor Drive", Proceedings of the IEEE Power Tech '99 Conference, Abstract records p. 111, Paper BPT99-447-60

EXPERIMENTAL METHODS FOR MAGNETISING CURVE IDENTIFICATION DURING COMMISSIONING OF VECTOR CONTROLLED INDUCTION MACHINES

Emil Levi, Slobodan N. Vukosavic *, Matija Sokola **
Liverpool John Moores University, School of Engineering, Liverpool, UK
* *University of Belgrade, Dept. of Electrical Engineering, Belgrade, Yugoslavia*
** *M.Sokola, University of Bath, Dept. of Mechanical Engineering, Bath, UK*

Abstract: *Numerous operating regimes of rotor flux oriented induction machines require variation of the rotor flux reference. Correct setting of the stator d-axis current reference therefore requires incorporation of the magnetising curve of the machine into the control system. Consequently, magnetising curve has to be identified during the drive commissioning. The paper describes two experimental methods for identification of the magnetising curve, developed for rotor flux oriented induction motor drives. The procedures are verified by extensive experimentation. Their merits and shortcomings regarding factory based commissioning and on-site commissioning are discussed.*

Keywords: *Vector Control /Commissioning/ Parameter Identification/Magnetising Curve*

1. INTRODUCTION

It is often the case in practice that the inverter and the vector controller are supplied by one manufacturer, while the machine comes from another manufacturer or is an existing machine on the site. Under these conditions it is not possible to set the parameters of the controller in advance and these have to be set at the site once when the inverter is connected to the machine. Such a situation has led to the development of the so-called self-commissioning procedures for vector controlled induction machines [1,2]. The main idea behind this concept is that all the parameters of the induction machine, required for vector control, are identified experimentally, by the controller itself. Once when the controller is initiated, a few tests are performed that enable calculation of the required parameters. The procedure of testing and calculation is done automatically following the first enabling of the controller. If the machine is already coupled to a load, the tests that enable identification of the parameters of the motor equivalent circuit should be performed at standstill. Alternatively, when the load is not connected, parameter identification may be performed with appropriate procedures developed for a running machine. The inertia of the machine and the load, that is needed in order to set up the parameters of the PI speed controller, is calculated during the first test run of the drive.

The other possible case that occurs in practice is that the complete drive is delivered by a single manufacturer. In such a case commissioning has to be performed in the factory, prior to the delivery of the drive. Requirements on factory based commissioning are less stringent as, in general, both a better qualified personnel is available and a wider range of laboratory equipment exists. The requirement that commissioning is performed using the same PWM inverter that will be used in subsequent on-site operation of the drive remains. However, the motor is in this case normally not coupled to the load and parameter identification by suitable tests developed for a running machine is always possible.

Identification of induction machine parameters at standstill is always performed by applying single-phase supply to the machine. In principle, two types of excitation may be applied. The first one is DC. From applied DC voltage and resulting DC steady-state current one finds the value of the stator resistance. Determination of the remaining parameters is then based most frequently on transient current responses that follow application of the DC voltage. Self-commissioning schemes that rely on this approach are available for both voltage-fed [3-5] and current-fed [6-8] rotor flux oriented induction machines (vector control of a current-fed machine asks for a smaller number of parameters). Some of these parameter identification schemes are at present too complicated to be incorporated into a true self-commissioning procedure, as they require substantial amount of signal processing (for example, [6] involves application of pseudo-random binary-sequence voltage excitation and requires an adaptive observer; the method of [7] relies on maximum likelihood estimation) and are therefore better classified as off-line parameter identification methods that could be used during factory based commissioning. The others, such as those described in [1-5,8] may be regarded as true self-commissioning schemes. The second method of parameter identification at standstill utilises standstill frequency response tests, where the applied single-phase excitation is AC rather than DC [9-11].

Parameter identification methods are not restricted to standstill tests. It is possible to use various testing procedures, developed for a running machine, to identify the parameters. Method described in [12] enables identification of all the parameters (except stator resistance) from measurements of fundamental and higher harmonics. An extremely simple procedure for rotor time constant tuning in the indirect rotor flux oriented induction machines, described in [13], is based on the tests performed while the machine is running under no-load conditions in the torque mode.

It should be noted that accuracy of parameter determination in both on-site self-commissioning procedures and in off-line identification techniques, that are suitable for factory based commissioning, depends on sample rate selection, quantization errors, resolution and accuracy of sensors, etc. [14]. Thus it appears that completely accurate identification is actually not possible and that all the parameters will be identified, regardless of the employed method, with some error.

The type of the vector control that has gained the firm ground in industrially available products is the indirect rotor flux oriented control of a current-fed machine. This method of vector control requires knowledge of the slip gain only when the drive is designed for operation in the base speed region only [15]. However, in many applications rotor flux reference is varied for one reason or the other and is therefore not a constant. In such a case knowledge of the rated rotor time constant value is insufficient for correct field orientation under all the operating conditions. Variation of the rotor flux reference is used when a rotor flux oriented induction machine is operated with maximum efficiency [16,17], when development of an increased short-term transient torque with limited current capability of the converter is required [18,19], or when accelerated build-up of the rotor flux is to be achieved [20]. The most frequently met case of variation of rotor flux reference is the operation in the field weakening region, where rotor flux reference has to be reduced below rated value [21,22]. Decrease in rotor flux reference is usually in inverse proportion to the rotor speed [23], although this is not optimal from the point of view of the torque capability [21,22].

Variation of the rotor flux reference implies variable level of main flux saturation in the machine. Magnetising inductance of the machine is therefore a variable parameter, determined with the instantaneous level of saturation. Although it is possible to perform on-line identification of the magnetising inductance [24], such an approach is usually not satisfactory as the variation in the saturation level is rapid. An alternative approach, that enables correct setting of the stator d-axis current reference for each value of the rotor flux reference, consists of embedding the magnetising curve of the machine in the control system [25-27]. This approach requires identification of the magnetising curve during factory based commissioning or during on-site commissioning of the drive.

Identification of the magnetising curve, using vector control system and PWM inverter, has been discussed extensively in recent past [4,8,10,28-32]. A method, ideal for self-commissioning, should enable identification at standstill with either single-phase AC or DC supply, it should require measurement of stator currents and DC voltage only, and it should be accurate. Additionally, an important consideration is the complexity of the algorithm. If it is aimed at on-site commissioning, it should be possible to add the algorithm within the existing digital controllers, so that its implementation needs to be simple. Unfortunately, a method that satisfies all these requirements is not available at present. If identification is performed with DC excitation at standstill, statistical methods, such as recursive least squares [4,28], have to be used in data processing. As voltages are reconstructed rather than measured, it is necessary to pre-determine inverter non-linear characteristic by appropriate tests, prior to the magnetising curve identification [4,28,29]. Accuracy of the method significantly deteriorates below certain magnetising current value [4,28,29], due to the pronounced impact of inverter lock-out time on identification results. This technique is therefore regarded as inappropriate for magnetising curve identification [30]. Another similar method, that performs identification at standstill using single-phase AC supply, is described in [31]. Problems regarding inverter non-linearity and lock-out time are very much the same as when DC voltage is used.

If measurement of stator voltages is acceptable, it is possible to avoid use of statistical methods and to perform identification purely from measurement data using either single-phase AC [10] or DC [8] supply. Methods of this group [8,10] are applicable during the drive commissioning if the voltage sensors are available. This is however rarely the case.

Approaches to the magnetising curve identification, described in [32-34] are not really suitable for either factory based commissioning or on-site commissioning of the drive. Identification of the magnetising curve, described in [32], is based on the broad-band excitation method, and requires injection of multiple frequency supply into machine stator terminals. Method of [33], although apparently very accurate, is not based on the inverter supply and is usually not applicable as it requires that neutral point of the stator star connected winding is accessible. Magnetising curve identification method of [34] has a number of shortcomings when its wider applicability is considered. It requires existence of a controllable load (a DC generator) that has to be coupled to the induction motor. It is therefore not applicable in on-site commissioning. Additionally, it is not possible to identify the magnetising curve below approximately 0.5 p.u. stator d-axis current reference as the identification takes place in loaded operation.

The purpose of this paper is to describe two experimental methods of magnetising curve identification in rotor flux oriented induction machines. Both methods have a couple of common features. Firstly, the same PWM inverter, that will be used in subsequent operation of a vector controlled induction machine, is utilised in the identification process. Secondly, the supply is three-phase rather than single-phase. Thirdly, identification is always based on steady-state measurements. Finally, testing is performed in a running machine under no-load conditions. The first method is a recent development [35], that appears to be extremely well suited to the factory based commissioning. The second method makes use of a special identification function, that was originally proposed in [36] for on-line rotor time constant identification, and is characterised with excellent accuracy. The methods are described, their accuracy is evaluated by experiments, and merits and shortcomings of each of them are evaluated with respect to their suitability for factory based and on-site commissioning.

2. DESCRIPTION OF THE DRIVE

As already noted, commercially available vector controllers typically rely on indirect feed-forward method of rotor flux oriented control [15]. For operation in the field-weakening region rotor flux reference is varied using the pre-programmed law,

$$\psi_r^* = \psi_{rn}\,\omega_B/\omega\,, \tag{1}$$

where indices n and B denote the rated value of rotor flux and base speed at which field weakening starts, respectively.

Operation with reduced rotor flux leads to an increase in the magnetising inductance in the machine. If the stator d-axis current reference is to be correctly set, it is necessary to compensate for the variation of main flux saturation in the machine, by including the inverse magnetising curve in the control system [25]. As shown in [25], an indirect feed-forward rotor flux oriented controller with partial compensation of main flux saturation is described with the following equations:

$$\psi_m = \psi_r^* + T_{\sigma r}^*\, d\psi_r^*/dt \tag{2}$$

$$i_{ds}^* = i_m(\psi_m) + \left(1/L_{\sigma r}^*\right)T_{\sigma r}^*\, d\psi_r^*/dt \tag{3}$$

$$\omega_{sl}^* = K_1\, i_{qs}^*/\psi_r^* \tag{4}$$

$$i_{qs}^* = \left(1/K_2\right)T_e^*/\psi_r^* \tag{5}$$

where $K_1 = L_{mn}^*/T_{rn}^*$ and $K_2 = (3/2)P\,L_{mn}^*/L_{rn}^*$ are constants. The index m identifies magnetising flux, current and inductance. An asterisk denotes reference values, while the rotor leakage time constant is $T_{\sigma r}^* = L_{\sigma r}^*/R_r^*$. The symbols T_e, ω_{sl} and i stand for torque, angular slip frequency and current, respectively. An indirect vector controller, described by (2)-(5), ignores the cross-saturation effect and neglects the change in the ratio of magnetising inductance to rotor inductance in (4)-(5) [25].

If the rotor speed is assumed to vary much more slowly than the electromagnetic transients, then the rate of change of the rotor flux reference in (2)-(3) is slow. It is therefore possible to further simplify (2)-(3), by neglecting the rate of change of rotor flux reference. Hence:

$$\psi_m = \psi_r^* \qquad i_{ds}^* = i_m(\psi_m)\,. \tag{6}$$

It should be pointed out that this approximation has no impact on any of the two methods of the magnetising curve identification described here. It merely reflects the actual structure of the controller in a commercially available drive [37], used in the experiments.

If rated magnetising current is taken as an independent input into the system, it is possible to introduce the normalised rotor flux value and normalised inverse magnetising curve. The indirect feed-forward rotor flux oriented controller then takes the form shown in Fig. 1, [37]. The constant K_2 and the variable rotor flux reference value, required for generation of the stator q-axis current reference in (5), are taken care of by the PI speed controller. The stator d-axis current reference is generated as the product of the rated value and a per unit value. The per unit value is obtained at the output of the inverse magnetising curve as a function of the per unit rotor flux reference (which is a function of speed). All the per unit values in Fig. 1 are identified with the index *pu*. Slip gain of the drive (denoted in Fig. 1 as SGD) is a constant parameter, given from (4) with $\mathrm{SGD} = L_{mn}^*/\left(T_{rn}^*\psi_{rn}\right)$.

The rated magnetising current can be relatively accurately estimated from the rated stator current and rated power factor for low to medium power machines. Alternatively, it can be experimentally determined by running the machine in vector control mode under no-load conditions at the rated frequency. If the fundamental voltage component is measured for different settings of the stator d-axis current reference, the rated magnetising current will correspond to the value of the stator d-axis current reference that yields the rated voltage at the machine terminals. Rated magnetising current was in this study determined using the former approach.

Correct operation of the control system of Fig. 1 at speeds above rated requires knowledge of the machine's magnetising curve. It is therefore necessary to identify this curve during commissioning of the drive.

3. MAGNETISING CURVE IDENTIFICATION: METHOD 1

The first identification method requires knowledge of the rated magnetising current and the stator leakage inductance. The complete indirect vector controller of Fig. 1 is used, including the unknown magnetising curve. Identification is performed under no-load conditions, by operating the machine in the field weakening region at different speeds. Measurement of the fundamental component of the stator voltage is required.

Implementation of the scheme of Fig. 1 requires analytical representation of the inverse magnetising curve. Many functions, of different complexity, can be selected. The method does not depend on the selected type of the analytical function. However, from the practical point of view, it is desirable to use the simplest possible representation.

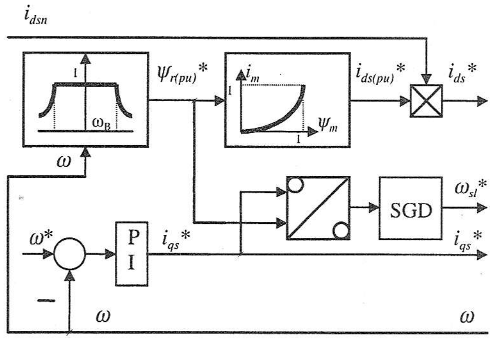

Fig. 1. *Indirect feed-forward vector controller of an industrial drive [37] with compensation of main flux saturation.*

As the curve is given in terms of per unit values, a convenient choice is the following simple two-parameter function:

$$i_{m(pu)} = a\psi_{m(pu)} + (1-a)\psi^{b}_{m(pu)}\,. \qquad (7)$$

Coefficients a and b are unknown and they have to be determined by the process of the experimental magnetising curve identification. Examination of the functional dependence given in (7) shows that, the influence of the parameter b on the inverse magnetising curve approximation is very small for flux values of interest, from zero up to 1 p.u.. The influence of parameter a is dominant in this region.

Let the machine operate in the field weakening region, with the rotor flux reference value given by (1). The stator d-axis current reference is then determined by

$$i_{ds}^{*} = \left(\psi_{rn}/L_m^{*}\right)\left(\omega_B/\omega\right), \qquad (8)$$

where L_m^* is a variable parameter, whose value for each speed setting depends on the actual values of parameters a and b of the inverse magnetising curve approximation (7) implemented in the controller of Fig. 1. As the machine operates under no-load conditions, the value of the slip gain parameter (SGD) is irrelevant, as the stator q-axis current command is zero. Mechanical and fundamental harmonic iron losses are neglected, and the rotor electrical speed of rotation ω is regarded as equal to the stator fundamental angular frequency ω_e. Regardless of the value of the magnetising inductance used in the controller, the orientation angle error is zero under such an idealised no-load operation. The steady-state stator voltage equations for fundamental harmonic

$$\begin{aligned} v_{ds} &= R_s i_{ds} - \omega_e \psi_{qs} \\ v_{qs} &= R_s i_{qs} + \omega_e \psi_{ds} \end{aligned} \qquad (9)$$

therefore reduce to

$$v_{ds} = R_s i_{ds}^{*} \qquad v_{qs} = \omega L_s i_{ds}^{*}, \qquad (10)$$

where $\omega = \omega_e$ is accounted for and reference and actual stator d-axis currents are equal due to absence of an orientation angle error. The magnitude of the fundamental component of stator voltage follows from (10),

$$v = \sqrt{v_{ds}^2 + v_{qs}^2} = i_{ds}^{*}\sqrt{R_s^2 + (\omega L_s)^2}\,, \qquad (11)$$

where L_s is stator self-inductance. Provided that the speed at which field weakening is initiated, ω_B, is sufficiently high, the stator resistance in (11) can be neglected. The peak value of the fundamental stator voltage is then from (8) and (11)

$$v = \psi_{rn}\omega_B \frac{L_{\sigma s} + L_m}{L_m^{*}}\,. \qquad (12)$$

Taking the product of the rated rotor flux and base speed as 1 p.u., equation (12) can be re-written as per unit voltage in the field weakening region,

$$v_{pu} = \frac{L_{\sigma s}}{L_m^{*}} + \frac{L_m}{L_m^{*}}\,. \qquad (13)$$

If the inverse magnetising curve approximation in the controller exactly matches the actual magnetising curve, then at all speeds $L_m \equiv L_m^*$. Variation of voltage in (13) with increase in speed is then negligibly small and is only due to variation in the term $L_{\sigma s}/L_m^*$, as magnetising inductance in the controller changes from the rated value towards the unsaturated value. However, if the inverse magnetising curve approximation is incorrect, the variation in voltage of (13) can be substantial. This is confirmed by performing the following experiment (experimental set-up is described in [35]). Parameters a and b of (7) are arbitrarily selected and the machine is operated as vector controlled (using the controller of Fig. 1) in the field-weakening region under no-load conditions. Fundamental components of the stator line-to-line voltage and stator current are measured for different operating speeds. Figure 2 illustrates measurement results (fundamental components of the stator line-to-line voltage and stator current in terms of rms values) for two values of coefficient a of (7), with $b = 7$. Cases with $a = 1$ (saturation ignored in the controller) and $a = 0.7$ (magnetising curve too saturated) are shown. The base speed is selected as 1150 rpm, while the rated synchronous speed of the machine is 1500 rpm. If the main flux saturation is neglected in the controller ($a = 1$), the stator voltage increases in the field weakening region, so that the voltage margin available for current control reduces (Fig. 2a). If saturation is over-compensated ($a = 0.7$), the voltage in the field weakening decreases (Fig. 2a). The stator d-axis current is reduced too much (Fig. 2b), leading to a decrease in the motor's torque capability. Thus only correct setting of parameters of the inverse magnetising curve (here a and b) enables operation with the correct voltage margin necessary for current control, with torque capability of the motor preserved.

The stator d-axis current reference and the measured fundamental component of the stator no-load current coincide, Fig. 2b. Stator current measurement is thus not necessary, as the stator d-axis current reference can be used instead.

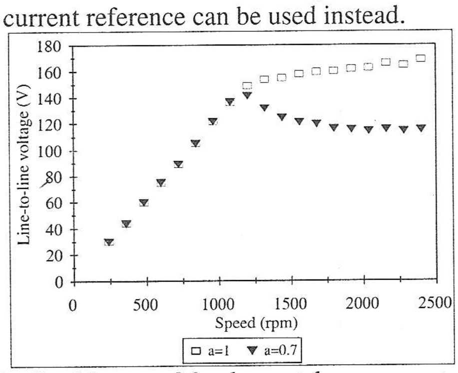

Fig. 2a. *Measured fundamental components of stator voltage, for b = 7 and two values of parameter a (stator d-axis current reference rms values included in (b)).*

On the basis of the theoretical considerations, the following procedure is suggested. Parameters a and b are arbitrarily selected and a variable frequency no-load test is performed in the field weakening region. Figure 3a illustrates a set of experimental results, obtained using a procedure identical to the one described in conjunction with Fig. 2. Field weakening is initiated at 1150 rpm and fundamental stator voltage is measured for various values of the coefficient a in the control system, with $b = 7$. As discussed in conjunction with (13), accurate representation of the inverse magnetising curve will lead to a practically constant value of the fundamental stator voltage in the field weakening region.

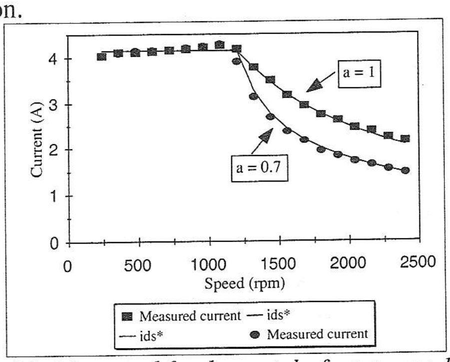

Fig. 2.b *Measured fundamental of stator no-load current, for b = 7 and two values of parameter a (stator d-axis current reference rms values included in (b)).*

Thus, by performing measurements for various values of coefficients a and b, it is possible to determine the most appropriate pair a, b purely by visual inspection of the measured voltage curves. From Fig. 3a the flattest voltage curve results for $a = 0.9$ with $b = 7$.

A more exact approach involving calculations based on (11), can be used for determination of the magnetising inductance as a function of the magnetising current (i.e., stator d-axis current reference). If the stator resistance is not known, it is neglected. The magnetising inductance is obtained from (11) as:

$$L_m = \frac{v}{\omega}\frac{1}{i_{ds}^*} - L_{\sigma s}. \tag{14}$$

It is necessary to measure only the fundamental component of the stator voltage, v. The speed of rotation equals the set speed and the stator d-axis current reference is used instead of the measured stator no-load current. For each set of points of Fig. 3a, that correspond to one pair of values of a and b, the magnetising inductance is calculated using (14) at all speeds. The inverse magnetising curve of the machine, calculated in this way, is shown in Fig. 3b. Figure 3b includes data obtained with all of the parameter a values used in Fig. 3a ($b = 7$).

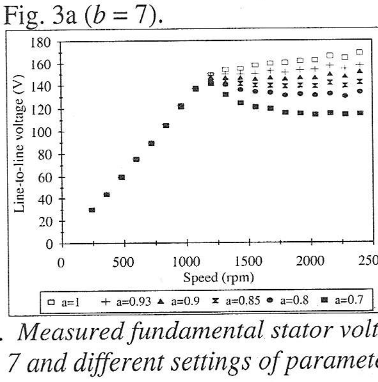

Fig. 3a. *Measured fundamental stator voltage for b = 7 and different settings of parameter a*

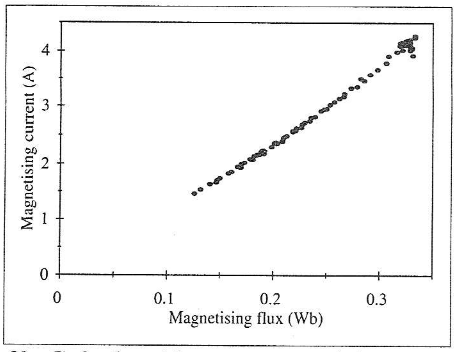

Fig. 3b. *Calculated inverse magnetising curve (all values are rms).*

Figure 3b shows that, regardless of the setting of the parameters a and b in the indirect vector controller, the identified points will always belong to the same curve. It is therefore sufficient to carry out the no-load test in the field weakening region with a single set of values of parameters a and b and then to calculate the inverse magnetising curve using (14). Fitting of the curve of Fig. 3b yields the required values as a = 0.9 and b =7. These values are the same as those that follow from Fig. 3a without any calculations (the flattest behaviour of the measured voltage in the field-weakening region, with all the values close to 1 p.u.).

Selection of the speed at which field weakening is started is rather arbitrary. This is confirmed by another experiment, that fully corresponds to those described in the previous sub-section. Field weakening is now initiated at 650 rpm and the tests are conducted up to a speed of around four times base speed. The inverse magnetising curve, calculated under these conditions by means of (14), is shown in Fig. 4. Overlapping of Figs. 4 and 3b shows that the two curves coincide. Figure 4 includes results of the standard no-load test, performed with variable voltage, 50 Hz sinusoidal supply. Agreement between the data obtained by two different experimental procedures is very good.

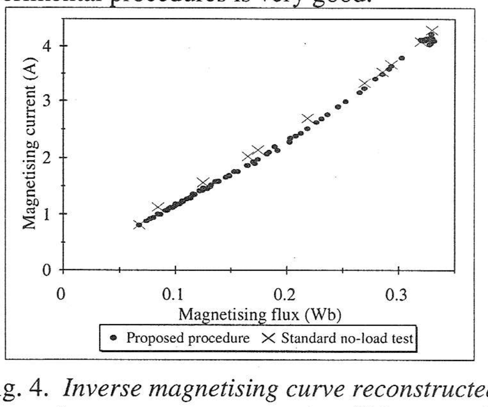

Fig. 4. *Inverse magnetising curve reconstructed from voltage measurements, using 650 rpm as the base speed, and curve obtained from standard no-load test with sinusoidal 50 Hz supply.*

This identification procedure is characterised with the following features. It requires that the machine can run under no-load conditions, that the fundamental component of the stator voltage can be measured (this is the only required measurement), and that the stator leakage inductance is known. It is extremely simple and it actually does not require any calculation as the pure visual inspection of the measurement results can be used to determine the most appropriate coefficients of the inverse magnetising curve approximation. The procedure is ideal for commissioning in factory and, as far as the on-site commissioning is concerned, it is only necessary that the load is not coupled and that a spectrum analyser is available on the site.

4. MAGNETISING CURVE IDENTIFICATION: METHOD 2

This method once more requires that the stator d-axis current reference can be varied. Measurement of only those quantities that are normally measured anyway in a vector controlled drive (stator currents and DC link voltage) is required. Stator voltages are reconstructed from known switching functions of the inverter and the measured DC link voltage. Information on measured stator currents and reconstructed stator voltages is further used to calculate a conveniently defined identification function. This function is defined in such a way that its value is independent of stator resistance and inverter lock-out time and it was proposed originally for on-line rotor time constant identification [36]. The special form of the identification function enables, as shown in what follows, direct calculation of the magnetising curve. The only required parameters of the machine are total leakage inductance and the rated value of the rotor time constant. These parameters have to be determined prior to the magnetising curve identification. Identification is performed at a certain constant speed of rotation (in contrast to the method described in the previous section), under steady-state no-load operating conditions, by performing a series of simple calculations for different values of the stator d-axis current reference.

Let the measured values of stator currents and DC link voltage be i_a, i_b, i_c and V_{DC}. Stator voltages are not measured and therefore they have to be reconstructed using measured value of the DC link voltage and known binary control signals fed to the inverter power switches (i.e. switching functions). Let the reconstructed stator phase voltages be v_a, v_b, v_c. Due to the reconstruction of the stator voltages, the problem of the lock-out time of power switches is faced. That is, the lock-out time causes a difference between the reconstructed voltage values and the actual voltages across the motor. Any function that is to be selected for identification purposes should therefore be of such a form that the discrepancy between reconstructed and actual voltages due to lock-out time effect does not affect its value. As it is intended to use reconstructed voltages in the formulation of the function for the magnetising curve identification, stator resistance will inevitably appear in this function. It is desirable to formulate the function in such a way that knowledge of the stator resistance is not required, as this is a varying parameter. The identification function therefore needs to be selected in such a way that the knowledge of the stator resistance is not necessary and that the difference between actual and reconstructed stator voltages due to lock-out time does not affect the value of the function. One such function has been proposed in [36] as a convenient choice for the process of on-line rotor resistance estimation in vector controlled induction machines. The function is defined as

$$F(v_a,v_b,v_c,i_a,i_b,i_c)=F(\underline{v}_s,\underline{i}_s)=i_a\int v_a dt+i_b\int v_b dt+i_c\int v_c dt \tag{15}$$

where underlined symbols denote space vectors of stator voltage and stator current, while indices *a*, *b*, *c* stand for the three stator phases. As shown in [36], this function satisfies the two above stated requirements. Stator voltages can be written as

$$v_a=R_s i_a+d\psi_a/dt\ ,\quad v_b=R_s i_b+d\psi_b/dt\ ,\quad v_c=R_s i_c+d\psi_c/dt. \tag{16}$$

so that

$$F(\underline{v}_s,\underline{i}_s)=i_a\psi_a+i_b\psi_b+i_c\psi_c+R_s\int\left(i_a+i_b+i_c\right)dt= \\ =i_a\psi_a+i_b\psi_b+i_c\psi_c \tag{17}$$

as sum of the three stator currents equals zero at any instant of time. After performing the co-ordinate transformation, (17) becomes

$$F(\underline{v}_s,\underline{i}_s)=i_{ds}^*\psi_{ds}+i_{qs}^*\psi_{qs} \tag{18}$$

Identification function F of (18) can be expressed in a convenient way in terms of the rotor flux d-q axis components as

$$F(\underline{v}_s,\underline{i}_s)=\sigma L_s i_s^2+\frac{L_m}{L_r}\left(\psi_{dr}i_{ds}^*+\psi_{qr}i_{qs}^*\right) \tag{19}$$

where

$$i_s=\sqrt{i_{ds}^2+i_{qs}^2}=\sqrt{i_{ds}^{*2}+i_{qs}^{*2}},$$

$\sigma=1-L_m^2/\left(L_s L_r\right)$ is the total leakage coefficient of the machine and L_s and L_r are stator and rotor self-inductances, respectively. Note that $\sigma L_s\approx L_{\sigma s}+L_{\sigma r}$ always holds true for any induction machine.

If correct field orientation is maintained in all the operating conditions, then $\psi_{qr}=0$ and $\psi_{dr}=\psi_r$. Furthermore, in any steady state $\psi_r=L_m i_{ds}^*$. Hence (19) becomes

$$F(\underline{v}_s,\underline{i}_s)=\left(L_{\sigma s}+L_{\sigma r}\right)i_s^2+\frac{L_m^2}{L_r}i_{ds}^{*2} \tag{20}$$

Stator current can be easily calculated from the known stator d-q axis current references as $i_s=i_s^*=\sqrt{i_{ds}^{*2}+i_{qs}^{*2}}$. Equation (20) suggests the following procedure for the magnetising curve identification. The machine is allowed to run at certain constant speed in closed-loop speed mode under no-load conditions. A series of steady-state measurements are performed for different values of the stator d-axis current reference. Value of the function F is evaluated for each setting of the stator d-axis current reference using (15). The first term on the right hand side of (20) is at first calculated on the basis of known stator d-q axis current references and total leakage inductance, and is further deducted from the appropriate function F value. Magnetising inductance is then obtained by equating the second term on the right-hand side of (20) to this difference. Magnetising characteristic, obtained from (20), is of the form $L_m=f\left(i_m\right)$ where $i_m=i_{ds}^*$ is assumed. Magnetising curve is finally obtained as $\psi_m=L_m i_{ds}^*$.

It is important to emphasise that identification of the magnetising curve, using (20) and the described procedure, assumes that correct field orientation is maintained during measurements. This could only be possible if the calculation of the reference slip in Fig. 1 would account for the non-linearity of the magnetising curve. At the identification stage magnetising curve is not known and therefore calculation of the reference slip will always be inaccurate to a smaller or greater extent. One could be inclined to say that calculation of the slip reference is irrelevant as the testing is performed under no-load conditions (so that stator q-axis current reference and slip reference are sufficiently close to zero). This is however not the case at low settings of the reference stator d-axis current (unless the speed at which testing is performed is sufficiently small, as shown later). Experiments show that in this region no-load losses can produce such a stator q-axis current reference, which, combined with incorrect setting of the slip gain, leads to detuned operation. Setting of the slip reference during experiments is discussed in more detail shortly.

Principles of magnetising curve identification are developed under the assumption that the existence of the iron losses and mechanical losses can be ignored. As the indirect vector controller neglects both types of losses, stator q-axis current reference inevitably has a non-zero value even under no-load conditions. Iron losses depend on the frequency of the supply, while mechanical losses are a function of the speed of rotation. It is therefore obvious that the speed at which testing is performed should be selected as low as possible.

Described identification procedure was experimentally tested using the commercially available indirect feed-forward rotor flux oriented controller [37]. Original structure of the control system is the one in Fig. 1. As magnetising curve of the machine is not known, it had to be bypassed in the controller of Fig. 1 during measurements. Stator d-axis current reference is therefore taken as an independent input into the system. It is varied in all the experiments (unless otherwise stated) from 0.2 to 1.7 of the rated value, with 0.1 step (rated value of the stator d-axis current is 0.52 p.u. on the rated stator current base; range of stator d-axis current variation is therefore $i_{ds}^* \in [0.104,\ 0.884]$ p.u.). It should be noted that the induction motor was in all the experiments coupled to a DC machine for the reason that is beyond the scope of this paper. The net consequence of this is the significantly higher value of the mechanical losses. Correct calculation of the reference slip in Fig. 1 requires knowledge of the magnetising curve, that is at present unknown. Consequently, calculation of the slip reference is bound to be inaccurate to some extent. Experiments are performed with two different methods of calculating the reference slip:

$$\begin{aligned} \omega_{sl}^* &= (SG)i_{qs}^* & SG &= 1\Big/\left(T_{rn}^* i_{dsn}\right) \\ \omega_{sl}^* &= \left(SG_n\right)i_{qs}^*\Big/i_{ds}^* & SG_n &= 1\Big/T_{rn}^* \end{aligned} \tag{21}$$

Reasoning behind this selection is as follows. For small stator d-axis current references calculation of the slip reference according to the first method of (21) gives a too low value of the slip reference (with respect to the correct one), while calculation according to the second method of (21) gives a too high value of the slip reference. The opposite holds true for $i_{ds}^* > i_{dsn}$. The errors in the identified magnetising curve (if any) are therefore expected to be of opposite signs for these two methods of the slip reference calculation. Figure 5 illustrates controller structure used in the experimental magnetising curve identification.

In each test-point value of the function F is determined using (15). Rather than being measured, stator voltages are reconstructed from the PWM pattern and the DC link voltage. The stator current feedback is acquired by scaling and filtering the signals from the drive current sensors. These signals are used for the evaluation of (15). Digital filtering and conditioning of the current feedback is aimed to filter out the ripple and the commutation noise, and affects in no way the average value of the identification function F. The problem encountered most frequently in the process of deriving the flux from the motor terminal quantities is the offset of the voltage integrators. Although the proposed calculations involve digital integration of the internal voltage commands, the parasitic DC component remains due to the offset of current sensors and the imperfection of the PWM chain and the VSI components. As proved in [36], the average value of the proposed identification function (15) is not sensitive to the offset of the voltage integrators. Therefore, the integration is performed by simple saturable integrators that prevent the clipping of the output wave-forms, leaving at the same time the parasitic DC component. As the offset does not affect the average value of (15) over several periods of the fundamental frequency [36], the function (15) is averaged within 1 second interval for each measurement point (i.e., for $i_{ds}^* \in [0.104,\ 0.884]$ p.u.).

Magnetising curve of the induction motor was at first determined using standard no-load test with variable voltage 50 Hz sinusoidal supply. Figure 6 displays magnetising characteristic and corresponding magnetising inductance, obtained in this way. Abscissa is given in Fig. 6 and all the subsequent figures in terms of the relative value of the stator d-axis current reference with respect to the rated stator d-axis current references, i_{ds}^*/i_{dsn}. All the relevant results of the identification procedure are plotted to the same scales as Fig. 6. Direct overlapping of corresponding figures thus enables direct comparison of the accuracy of the proposed procedure. Actual measurement and/ or identification points are in all the figures denoted with a circle or a square.

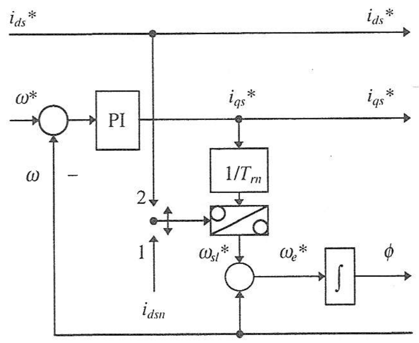

Fig. 5. *Structure of the control system used in the experiments: Method 1:* $\omega_{sl}^* = (SG)i_{qs}^*$*; Method 2:* $\omega_{sl}^* = (SG_n)i_{qs}^*/i_{ds}^*$

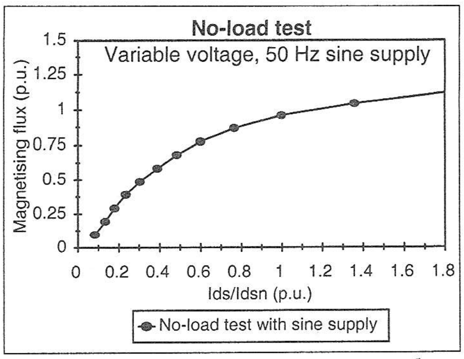

Fig. 6. *Magnetising curve and magnetising inductance obtained from standard no-load test with sinusoidal supply.*

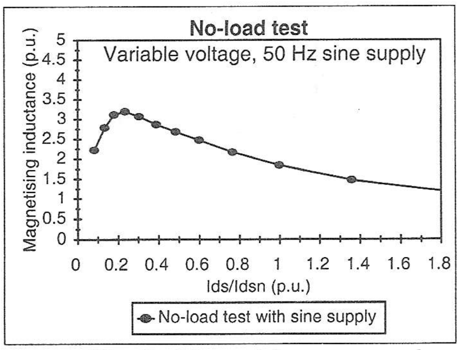

Fig. 6. *Magnetising curve and magnetising inductance obtained from standard no-load test with sinusoidal supply.*

Test were performed initially at two speeds of rotation, selected quite arbitrarily as 375 rpm and 1050 rpm, under no-load conditions. It should be noted that, as identification process includes magnetising current values higher than rated, the highest possible speed at which one can attempt the identification is limited by the voltage reserve of the inverter. On the basis of the previous discussion one can expect that the results of the identification will be better at the lower of the two speeds. Indeed, experimental results confirm this expectation, as shown shortly.

Figure 7 depicts values of the identification function *F*, obtained using (15), for both speeds of rotation and for both methods of calculating the slip reference. The four curves completely overlap, indicating that the function *F* is independent of both the speed of rotation and the method of the slip reference calculation.

Figure 8 shows variation of the stator q-axis current reference (as relative value with respect to the rated stator current) for the two speeds of rotation and for the two methods of the reference slip calculation.

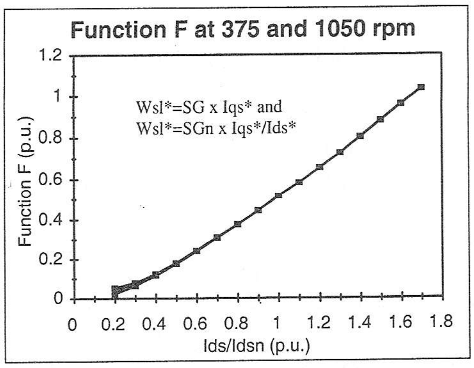

Fig. 7. *Function F values for 375 rpm and 1050 rpm tests for both methods of slip reference calculation.*

An important conclusion that follows from Fig. 8 is that at 1050 rpm a substantially higher stator q-axis current reference is required for any setting of the stator d-axis current reference and regardless of the method of the reference slip calculation. This is a consequence of an increase in the iron and mechanical losses at 1050 rpm, when compared to the losses at 375 rpm. Values of stator q-axis current reference become especially high at 1050 rpm for very low settings of the stator d-axis current reference, where mechanical losses are dominant.

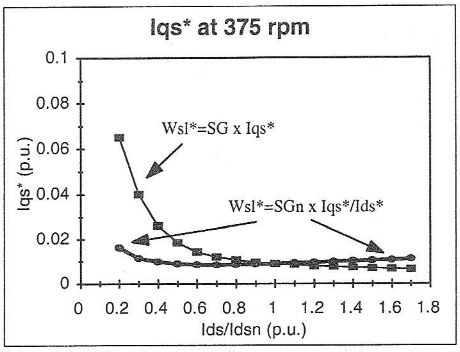

Fig. 8a. *Variation of stator q-axis current reference at 375 rpm for the both methods of the slip reference calculation.*

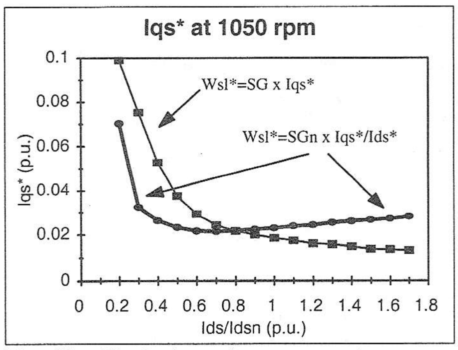

Fig. 8b. *Variation of stator q-axis current reference at 1050 rpm (b) for the both methods of the slip reference calculation.*

Values of function *F* of Fig. 7 and stator q-axis current reference of Fig. 8 are further used to reconstruct the magnetising curve of the machine by means of (20). Identified magnetising curve is shown in Fig. 9a for 375 rpm speed and Fig. 9b for 1050 rpm speed. Both methods of slip reference calculation are considered. At sufficiently high values of stator d-axis current reference (above 0.5 i_{dsn} at 1050 rpm and above 0.3 i_{dsn} at 375 rpm) detuning caused by incorrect setting of the slip reference is negligibly small. Consequently both methods of the slip reference calculation lead to the same reconstructed magnetising curve, at both speeds. Overlapping with Fig. 6 shows excellent matching. However, for small values of the stator d-axis current reference detuning becomes pronounced, so that (20) is essentially not valid any more. As a consequence, the two methods of the reference slip calculation give two different predictions of the magnetising curve that are positioned at opposite sides of the correct curve. The stator d-axis current reference threshold value below which discrepancies start to occur is $i_{ds}^{*} = 0.5 i_{dsn}$ for 1050 rpm and $i_{ds}^{*} = 0.3 i_{dsn}$ for 375 rpm. Furthermore, deviations of the reconstructed curve from the correct one at very low stator d-axis current reference setting are much higher at 1050 rpm than at 375 rpm. These findings confirm that the identification should be performed at as low speed as possible.

In order to further improve the accuracy of the magnetising curve identification, the third no-load test is performed. Speed of rotation is reduced to just 100 rpm. Mechanical losses are now made negligibly small. Consequently, stator q-axis current reference is so small even in the region of the low stator d-axis current reference, that it becomes irrelevant which method of the slip reference calculation is used. Detuning is practically completely eliminated and both methods of slip reference calculation lead to the same identified magnetising curve. Testing is now performed for stator d-axis current reference from 0.1 to 1.7 of the rated value.

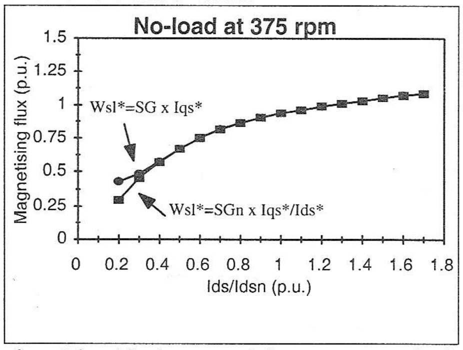

Fig. 9a. *Identified magnetising curve on the basis of measurements at 375 rpm*

Figure 10a displays magnetising curve, while Fig. 10b shows corresponding magnetising inductance. Overlapping of Figs. 6a and 10a shows extremely small differences in the region of very small stator d-axis current references. Figure 10b shows that sufficient reduction of the speed at which testing is performed enables even identification of the point of inflexion. This is known to be a problem with most of the existing methods [4,29].

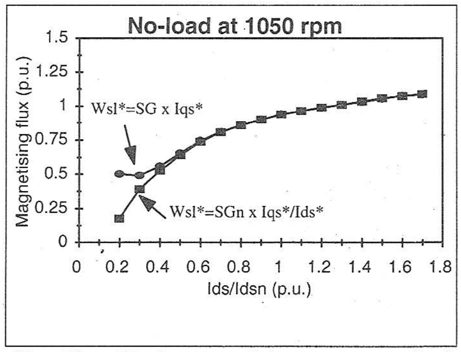

Fig. 9b. *Identified magnetising curve on the basis of measurements at 1050 rpm*

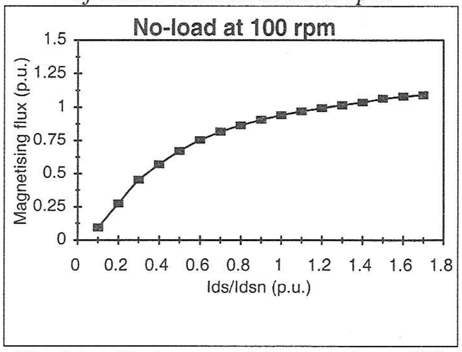

Fig. 10. *Identified magnetising curve at 100 rpm.*

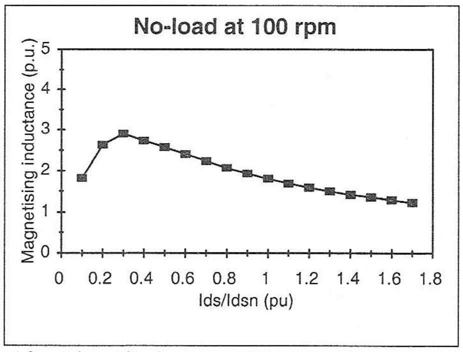

Fig. 10. *Identified magnetising inductance at 100 rpm.*

This method is believed to offer an excellent potential for the application in on-site self-commissioning of vector controlled induction motor drive. It requires no additional measurements and the calculation of the identification function F of (15) is easy to implement within the drive controller. As all the subsequent calculations related to (20) are pure algebraic manipulations, the method can be fully automated at a minimum expense. The only requirement is that the induction machine is not already coupled to the load. Of course, the method can be used in factory based commissioning as well. Presented experimental results indicate excellent accuracy of the method at very low speeds, when only measurements with one of the two possible ways of setting the slip reference are required. Successful implementation of the method requires that total leakage inductance and the rated rotor time constant (slip gain) are identified prior to the magnetising curve identification.

5. CONCLUSION

Two novel methods of magnetising curve identification in vector controlled induction machines are presented and experimentally verified in the paper. Both methods utilise the same PWM inverter supply that will be subsequently used in normal operation of the drive, and testing is in both cases performed in the running machine under no-load conditions. In the first method, testing is performed in the field weakening region, at various operating speeds, and reduction of the stator d-axis current reference is achieved automatically by increasing the operating speed above the base speed. The only additional measurement required is the one of the stator voltage fundamental component. The method is extremely simple as identification can be performed without any calculations. As the application of the method requires a spectrum analyser, its primary area of application is likely to be factory based commissioning.

The second method requires no additional measurements, but it requires inclusion of an appropriate software for the identification algorithm within the vector controller. All the calculations involved in the identification procedure are rather simple, so that the cost of including such a software within the vector controller is minimal. Identification is performed at a constant speed of rotation, that should be as low as possible for the best accuracy. The method is characterised with an excellent accuracy, down to ten percent of the rated magnetising current. It is primarily aimed at the on-site self-commissioning, although it can equally be used in the factory based commissioning.

6. REFERENCES

[1] H. Schierling, "Self-commissioning - A novel feature of modern inverter-fed induction motor drives," *Proc. IEE Conf. on Power Electronics and Variable Speed Drives PEVSD*, IEE Conf. Pub. no. 291, London, UK, 1988, pp. 287-290.

[2] R. Jötten, E.D. Lettner, "Adaptive and self-commissioning control for a drive with induction motor and current source inverter," *Proc. Eur. Power Electronics and Applications Conf. EPE*, Aachen, Germany, 1989, pp. 627-632.

[3] M. Sumner, G.M. Asher, "Autocommissioning for voltage-referenced voltage-fed vector-controlled induction motor drives," *IEE Proceedings - B*, vol. 140, no. 3, 1993, pp. 187-200.

[4] M. Ruff, A. Bünte, H. Grotstollen, "A new self-commissioning scheme for an asynchronous motor drive system," *Proc. IEEE IAS Annual Meeting*, Denver, CO, 1994, pp. 616-623.

[5] A.M. Khambadkone, J. Holtz, "Vector-controlled induction motor drive with a self-commissioning scheme," IEEE Trans. on Industrial Electronics, vol. 38, no. 5, 1991, pp. 322-327.

[6] P.J. Chrzan, H. Klaassen, "Parameter identification of vector-controlled induction machines," *Electrical Engineering*, vol. 79, no. 1, 1996, pp. 39-46.

[7] S.I. Moon, A. Keyhani, "Estimation of induction machine parameters from standstill time-domain data," *IEEE Trans. on Industry Applications*, vol. 30, no. 6, 1994, pp. 1609-1615.

[8] W.H. Kwon, C.H. Lee, K.S. Youn, G.H. Cho, "Measurement of rotor time constant taking into account magnetising flux in the induction motor," *Proc. IEEE IAS Annual Meeting*, Denver, CO, 1994, pp. 88-92.

[9] C. Wang, D.W. Novotny, T.A. Lipo, "An automated rotor time constant measurement system for indirect field-oriented drives," *IEEE Trans. on Industry Applications*, vol. 24, no. 1, 1988, pp. 151-159.

[10] N.R. Klaes, "Parameters identification of an induction machine with regard to dependencies on saturation," *Proc. IEEE IAS Annual Meeting*, Dearborn, Michigan, 1991, pp. 21-27.

[11] R.J. Kerkman, J.D. Thunes, T.M. Rowan, D. Schlegel, "A frequency based determination of the transient inductance and rotor resistance for field commissioning purposes," *Proc. IEEE IAS Annual Meeting*, Orlando, FL, 1995, pp. 359-366.

[12] R.J.A. Gorter, J.L. Duarte, P.P.J. van den Bosch, "Parameter estimation for induction machines," *Proc. Eur. Power Electronics and Applications Conf. EPE*, Sevilla, Spain, 1995, pp. 3.627-3.632.

[13] R.D. Lorenz, "Tuning of field oriented induction motor controllers for high performance applications," *Proc. IEEE IAS Annual Meeting*, Toronto, ON, 1985, pp. 607-612.

[14] D.E. Borgard, G. Olsson, R.D. Lorenz, "Accuracy issues for parameter estimation of field oriented induction machine drives," *IEEE Trans. on Industry Applications*, vol. 31, no. 4, 1995, pp. 795-801.

[15] D.W.Novotny, T.A.Lipo, "*Vector control and dynamics of AC drives,*" Oxford: Clarendon Press, 1996.

[16] D.S.Kirschen, D.W.Novotny, T.A.Lipo, "Optimal efficiency control of an induction motor drive," *IEEE Trans. on Energy Conversion,* vol. 2, no. 1, 1987, pp. 70-76.

[17] R.D.Lorenz, S.M.Yang, "Efficiency-optimised flux trajectories for closed-cycle operation of field-orientation induction machine drives," *IEEE Trans. on Industry Applications,* vol. 28, no. 3, 1992, pp. 574-580.

[18] I.T.Wallace, D.W.Novotny, R.D.Lorenz, D.M.Divan, "Increasing the dynamic torque per ampere capability of induction machines," *Proc. IEEE Ind. Appl. Soc. Annu. Meet. IAS,* Dearborn, Michigan, 1991, pp. 14-20.

[19] I.T.Wallace, D.W.Novotny, R.D.Lorenz, D.M.Divan, "Verification of enhanced dynamic torque per ampere capability in saturated induction machines," *IEEE Trans. on Industry Applications,* vol. 30, no. 5, 1994, pp. 1193-1201.

[20] D.S.Zinger, "A flux control for improved dynamic response," *Proc. IEEE Ind. Appl. Soc. Annu. Meet. IAS,* Dearborn, Michigan, 1991, pp. 47-51.

[21] B.J.Seibel, T.M.Rowan, R.J.Kerkman, "Field-oriented control of an induction machine in the field-weakening region with DC-link and load disturbance rejection," *IEEE Trans. on Industry Appl.,* vol. 33, no. 6, 1997, pp. 1578-1584.

[22] H.Grotstollen, J.Wiesing, "Torque capability and control of a saturated induction motor over a wide range of flux weakening," *IEEE Trans. on Industrial Electronics,* vol. 42, no. 4, 1995, pp. 374-381.

[23] R.Joetten, H.Schierling, "Control of the induction machine in the field weakening range," *Proc. IFAC Symp. Power Electronics and Electric Drives,* Lausanne, Switzerland, 1983, pp. 297-304.

[24] D.H.Choi, S.B.Cho, D.S.Hyun, "Improved torque response by tuning of the magnetising inductance under field weakening operation region," *Conf. Rec. IEEE Ind. Appl. Soc. Annu. Meet. IAS,* New Orleans, LA, 1997, pp. 418-425.

[25] E.Levi, S.Vukosavic, V.Vuckovic, "Saturation compensation schemes for vector controlled induction motor drives," *Conf. Rec. IEEE Power Elec. Spec. Conf. PESC,* San Antonio, TX, 1990, pp. 591-598.

[26] R.S.Wieser, "Optimal rotor flux regulation for fast accelerating induction machines in the field weakening region," *Conf. Rec. IEEE Ind. Appl. Soc. Annu. Meet. IAS,* New Orleans, LA, 1997, pp. 401-409.

[27] E.Levi, "Magnetic saturation in rotor flux oriented induction motor drives: Operating regimes, consequences and open-loop compensation," *European Transactions on Electrical Power ETEP,* vol. 4, no. 4, 1994, pp. 277-286.

[28] M.Ruff, H.Grotstollen, "Off-line identification of the electrical parameters of an industrial servo drive systems," *Conf. Rec. IEEE Ind. Appl. Soc. Annu. Meet. IAS,* San Diego, CA, 1996, pp. 213-220.

[29] H.Rasmussen, M.Knudsen, M.Tonnes, "Parameter estimation of inverter and motor model at standstill using measured currents only," *Proc. IEEE Int. Symp. on Industrial Electronics ISIE,* Warsaw, Poland, 1996, pp. 331-336.

[30] M.Bertoluzzo, G.Buja, R.Menis, "Identification techniques of induction motor parameters for self-commissioning field-oriented drives," *Automatika,* vol. 38, no. 3-4, 1997, pp. 103-115.

[31] G.Buja, R.Menisi, "Identification of the magnetizing characteristic of an induction motor incorporated into a field-oriented drive for self-commissioning purposes," *Proc. Int. Conf. Power Elec. and Motion Control PEMC,* Prague, Czech Republic, 1998, pp. 3.75-3.80.

[32] A.Ganji, P.Guillaume, R.Pintelon, P.Lataire, "Induction motor dynamic and static inductance identification using a broadband excitation technique," *IEEE Trans. on Energy Conversion,* vol. 13, no. 1, 1998, pp. 15-20.

[33] A.Stankovic, E.R.Benedict, V.John, T.A.Lipo, "A novel method for measuring induction machine magnetizing inductance," *Proc. IEEE Ind. Appl. Soc. Annu. Meet. IAS,* New Orleans, Lousiana, 1997, pp. 234-238.

[34] E.Levi, "Method of magnetising curve identification in vector controlled induction machines," *European Trans. on Electrical Power Eng. ETEP,* vol. 2, no. 5, 1992, pp. 309-314.

[35] M.Sokola, "Vector control of induction machines using improved machine models", *PhD Thesis,* Liverpool John Moores University, Liverpool, UK, 1998.

[36] S.N.Vukosavic, M.R.Stojic, "On-line tuning of the rotor time constant for vector-controlled induction motor in position control applications", *IEEE Trans. on Industrial Electronics,* vol. 40, no. 1, 1993, pp. 130-138.

[37] "DBS 04 User's Manual," *Vickers Electrics*, Cassela, Italy, 1996.

DEFINITION AND CALCULATION OF REACTANCES IN ELECTRICAL MACHINES

Dr Dragan Petrovic, Faculty of Electrical Engineering, Belgrade, Yugoslavia

1.Introduction

In the analysis of the functioning of electrical machines various reactances are often used both in considering stationary states as well as in transient phenomena. When asynchronous or synchronous machines are at stake, two analysing methodologies are usual. In the first case the so-called phase coordinates are used, where In In the analysis of the functioning of electrical machines various reactances are often used both in considering stationary states as well as in transient phenomena. When asynchronous or synchronous machines are at stake, two analysing methodologies are usual. In the first case the so-called phase coordinates are used, where every phase or particular winding are shown with their real voltages, currents and parameters. In the majority of cases, instead of the previous manner, the transformed windings are applied and the magnitudes by which they are modelled. The most known is the so-called Park d,q,o transformation and a series of others [1]. In previous models as an essential parameter inductivity, i.e. reactances in various forms and amounts appear. The aim of this paper is to define various reactances and to explain their link.

2.Definitions and calculations of reactances in asynchronous and synchronous machines

Since the reactance is the product of circular frequency and inductivity the problem reduces to define the inductivity of the machines under consideration. As the inductivity,by definition, is the relation between flux inclusion of the phase observed and the current provoking this flux, the following inductivities are defined for one multy-phase machine.

a- inductivity due to flux scattering

b- inductivity due to flux passing through air-gap (the main inductivity).

The inductivity due to flux scattering ($L\gamma$) of the phase under consideration depends on the form and dimensions of grooves where the parts of this phase are located, is calculated on the basis of data about the windings and the machine dimensions [2]. This part of inductivity of the windings does not change for two mentioned manners of machine modelling, so that we will not deal with them. The main flux Φ passing through air-gap is involved by particular phases and one or more phases take part in its creation. The corresponding main inductivity (or eigen-inductivity) of phase 1 is defined as:

$$L_1 = \frac{\psi_1}{i_1},$$

where $\Psi_1 = k_1 N_1 \Phi$ is the flux involvement of phase 1 having the number of windings N_1 and winding factor k_1, through which current i_1 passes. Flux Φ is calculated by means of the maximal values of induction in B_{m1} and the pole surface, i.e. $\Phi = 2/\pi\tau l B_{m1}$, where τ are pole steps and l the axial length of the machine (tins). The induction in the air-gap of length δ is provoked by a magnetoexciting force (MPS) $F_{\delta m}$ (by a pole), so that:

$$B_{m1} = \mu_0 \frac{F_{\delta m}}{\delta}$$

If this magnetic field is created by a phase or a winding with winding.... k1, with the number of windings N1 and current I1, then the corresponding inductions I:

$$B_{m1} = \mu_0 \frac{F_{\delta m}}{\delta} = \mu_0 \frac{2\sqrt{2}}{\pi} \frac{N_1 k_1 I_1}{p\delta} = \frac{8 N_1 k_1}{p\delta} I_{m1} \cdot 10^{-7} \; [\mathrm{T}]$$

To this maximal value of the induction in... corresponds the sum of fluxes by a pole:

$$\Phi_1 = \frac{2}{\pi} B_{m1} \tau l = \frac{16}{\pi} \frac{\tau l}{p\delta} N_1 k_1 I_{m1} \cdot 10^{-7} \; [\mathrm{Wb}] \quad (1)$$

The flux involvement of the phase observed amounts to:

$$\Psi_1 = N_1 k_1 \Phi_1 = \frac{16}{\pi} \frac{\tau l}{p\delta} (N_1 k_1)^2 I_{m1} \cdot 10^{-7} \; [\mathrm{Wb}]$$

Thus, the main inductivity (eigeninductivity) of the phase under consideration amounts to:

$$L_1 = \frac{\Psi_1}{I_{m1}} = \frac{16}{\pi} \frac{\tau l}{p\delta} (N_1 k_1)^2 \cdot 10^{-7} \; [\mathrm{H}] \quad (2)$$

In a *three-phase* winding ,where the field in air-gap is formed by all three phases of induction in air-gap is:

$$B_3 = \mu_0 \frac{F_3}{\delta} = \mu_0 \frac{3}{2} \frac{F_{\delta m}}{\delta}$$

so that the corresponding inductivity (cyclic) is:

$$L_3 = \frac{3}{2}L_1 = \frac{24}{\pi}\frac{\tau l}{p\delta}(k_1N_1)^2 \cdot 10^{-7} \quad [H]$$

This is the inductivity of magnetizing in asynchronous machines or the inductivity of the reaction of the induct in a synchronous machine. Multiplied with circuit frequency ω that inductivity defines the corresponding reactance X_m i.e X_a.

The total reactance of a phase is obtained when the reactance of scattering $X\gamma$ is added to the former main reactance.

It is necessary to mention that the former inductivities are defined at constant air-gap δ and sinusoidal scattering MPS.

Mutual inductivity of two phases depends on the electrical angle between the axes of these two phases α_{21} so that the flux involvement of phase 2 due to the field , created by the current of phase l:

$$\psi_{21} = \psi_{m1}\cos\alpha_{21}$$

and the mutual inductivity is then:

$$L_{21} = \frac{\psi_{21}}{i_1} = \frac{\psi_{m1}}{\sqrt{2}I_1}\cos\alpha_{21} = L_1\cos\alpha_{21} \tag{3}$$

In three-phase machines (phases 1,2 and 3) $\alpha_{21}=2\pi/3$, so that je $L_{21}=L_{31}= -L_1/2$. If identical windings of particular phases and fully symmetrical currents are involved, then $L_{21}=L_{12}=L_{23}=L_{31}=L_{32}=L_{13}$. The windings of phases can be located on the stator or a rotor or on either of them. In a general case there are one or more phases. If two phases are considered l and 2, one of which (1) is in the stator and the other (2) on the rotor and `provided they are unsymmetrical, i.e. $N_1 \neq N_2$ and $k_1 \neq k_2$ then the mutual inductivity of those two windings is calculated from the expression:

$$L_{21} = \frac{\psi_{21m}}{\sqrt{2}I_1}\cos\alpha_{21} = \frac{N_2k_2\Phi}{\sqrt{2}I_1}\cos\alpha_{21}$$

The air-gap flux Φ is created by the winding current 1 and is calculated according to (1), so that: $L_{21}=L_{21m}\cos\alpha_{21}$, where:

$$L_{21m} = \frac{4\mu_0}{p\pi^2}(N_1k_1N_2k_2)\frac{\tau l}{\delta} \tag{4}$$

the maximal value of the mutual induction existing when the axes of phases (windings) l and 2 overlap; then the angle between these two axes $\alpha_{21}=0$. Angle α_{21} is changeable because the winding 2 turns to the angular speed Ω so that $\alpha_{21}=\Omega pt=\omega t$, which means that the inductivity $l_{21}=L_{21m}\cos\omega t$ is the harmonious time function. It is not difficult to find out that $L_{21}=L_{12}$. If the stator magnetic field is cylindrical, then L_{21m} does not depend on the angle α_{21} since δ is constant.

Apart from the above described eigen and mutual inductivities of particular phases, the inductivities related to the air-gap flux, due to all phases belonging to the winding of the stator or the rotor, are defined. So formerly the so-called *cyclic inductivity* for three phases on the stator was defined. Analogously the mutual inductivity was defined, say, of all stator phases and particular phases on the rotor, and vice vesa. So we obtain for the mutual phase inductivity on the stator and the entire winding on the rotor (with q_2 phases) whose MPS is:

$$F_{2m} = \frac{q_2\sqrt{2}}{\pi}\frac{I_2N_2k_2}{p}$$

i.e. the induction $B_{2m}=\mu_0F_{2m}/\delta$, and the flux of phase 1 on the stator with the rotor field:

$$\psi_{1m} = \frac{2}{\pi}\tau l N_1k_1B_{2m}$$

so that the inductivity is:

$$L'_{12m} = \frac{\psi_{1m}}{\sqrt{2}I_2} = \frac{2q_2\mu_0}{p\pi^2}(N_1k_1N_2k_2)\frac{\tau l}{\delta}$$

This inductivity for $q_2/2$ is greater than the mutual inductivity of phases on the stator and the rotor (4), i.e. $L'_{12m}=q_2/2L_{12m}$. Also, $L'_{21m}=q_1/2L_{21m}$, which means that for $q_1 \neq q_2$ $L'_{12m} \neq L'_{21m}$.

2.1. The inductivities of synchronous machines with sailent poles

In this type of synchronous machines the inequality of the air-gap lengths is present. The smallest length is in the axis of the sailent pole, and the greatest in the space between two adjacent poles. This change provokes also the change of the magnetic resistance, so that the flux of the induct reaction in air-gap will depend considerably on the instant position of the rotor. It will vary between the greatest value obtained when the field axis of the rotor overlaps with that of the phase under observation of the stator and the smallest value at the axis passing between two poles of the rotor through the phase axis. So, in the course of the passing of an entire rotor pole beside the stator phase the magnetic resistance, and thereby the flux of it and the inductivity will have a full period of the change around some mean value. So the eigeninductivity of phase 1 of the stator can be expressed in the form:

$$l_1 = l_0 + l_2\cos 2\theta + l_4\cos 4\theta + \dots$$

The usual assumption is that the inductivity variation is l_1, if the mean value l_0 is sinusoidal so that only two first terms in the previous relation are retained, i.e.

$$l_1 = l_0 + l_2\cos 2\theta \qquad (5)$$

The mean value of inductivity lo is determined from expression: $l_0=(l_d+l_q)/2$ where l_d and l_q are the greatest and the smallest inductivities of the phase observed obtained when d i.e. q axes of the rotor overlap with its axis. They are calculated in such a way that primarily the sum of the flux of the induct reactance with respct to d and q axes is found thereby taking into consideration the unequal magnetic resistance along these two axes, so that according to (2 $l_d=l_1k_d$ and $l_q=l_1k_q$ where k_d and k_q are the co-makers of the field form of the reactance of induct d, i.e. the q axis [2]. Amplitude l_2 of the inductivity change l_1 in expression (5) is determined as $l_2=(l_d-l_q)/2$.

Mutual inductivity of the stator phases of this type of machine varies also around one mean value with the double value of angle θ of position d of the rotor axis and phase axis 1 on the stator, so that [2] : $l_{12}=l_{120}+l_{12m}\cos(2\theta-2\pi/3)$ where $l_{120}=-l_0/2$ and $l_{12m}=l_2$ i.e.:

$$l_{12}=-l_0/2+l_2\cos(2\theta-2\pi/3) \qquad (6)$$

Mutual phase inductivity of stator (1) and rotor(2) is a function of angle θ and its greatest value is determined by means of relation (4). An excitation winding (f) exists on the synchronous machine rotor whose axis overlaps with axis d of the pole; as usual two equivalent dumping windings ,one of which (D) overlaps with axis d and the other (Q) with the axis q of the rotor. The amplitudes of their mutual inductivities with the stator phases are calculated by means of expression (4) where index 1 is substituted by a, b or c, and index 2 by f, D or Q.

3. Matrices of inductivity in phase coordinates

The asynchronous machine has three phases on the stator with marks a,b,c and three equivalent phases on rotor A,B,C.

The matrix of all inductivities for phase coordinates would be:

$$[L]=\begin{bmatrix} l_{aa} & l_{ab} & l_{ac} & l_{aA} & l_{aB} & l_{aC} \\ l_{ba} & l_{bb} & l_{bc} & l_{bA} & l_{bB} & l_{bC} \\ l_{ca} & l_{cb} & l_{cc} & l_{cA} & l_{cB} & l_{cC} \\ l_{Aa} & l_{Ab} & l_{Ac} & l_{AA} & l_{AB} & l_{AC} \\ l_{Ba} & l_{Bb} & l_{Bc} & l_{BA} & l_{BB} & l_{BC} \\ l_{Ca} & l_{Cb} & l_{Cc} & l_{CA} & l_{CB} & l_{CC} \end{bmatrix} \qquad (7)$$

Here all eigeninductivities are the constants and they are calculated by means of expression (2). The mutual inductivities of the stator or rotor phases are also constant and they are determined by expression (3). The mutual inductivities of stator and rotor phases depend on angle θ and their amplitudes are calculated by expression (4).

Synchronous machines with a roller rotor where the exciting winding f is, and the dumping windings D and Q have a similar matrix of inductivity (7) of asynchronous machine:

$$[L]=\begin{bmatrix} l_{aa} & l_{ab} & l_{ac} & l_{af} & l_{aD} & l_{aQ} \\ l_{ba} & l_{bb} & l_{bc} & l_{bf} & l_{bD} & l_{bQ} \\ l_{ca} & l_{cb} & l_{cc} & l_{cf} & l_{cD} & l_{cQ} \\ l_{fa} & l_{fb} & l_{fc} & l_{ff} & l_{fD} & l_{fQ} \\ l_{Da} & l_{Db} & l_{Dc} & l_{Df} & l_{DD} & l_{DQ} \\ l_{Qa} & l_{Qb} & l_{Qc} & l_{Qf} & l_{QD} & l_{QQ} \end{bmatrix} \qquad (8)$$

Here $l_{DQ}=l_{fQ}=0$ because d and q are the axes shifted for $\pi/2$. The amplitudes of particular inductivities of this matrix are calculated analogously to that of matrix (7).

Synchronous machine with silent poles has a matrix of inductivity like matirx (8) ,but particular elements of the matrix differ considerably. There are eigen and mutual inductivities of the stator phase depending on the rotor position, i.e. on angle θ and they are calculated by means of expressions (5) and (6) respectively. As well as in matrix (8) and eigen and mutual inductivities of the rotor winding do not depend on angle θ; they are calculated in the already described manner.

4. Inductivities and reactances of machines in the transformed d,q,o system

In a majority of cases the analysis of the work of synchronous, and often of asynchrous machines, is made with transformed magnitudes and parameters instead of with their real values.Most often the so-called d,q,0 Park's coordinate system or, i.e. Blondel's systems are applied. By applying these transformations [1,3] the inductivities, i.e. reactances change. Instead of the inductivity matrix (8) for a synchronous machine with sailent poles the following matrix is arrive at:

$$[L]=\begin{bmatrix} L_0 & 0 & 0 & 0 & 0 & 0 \\ 0 & L_d & 0 & L_{df} & L_{dD} & 0 \\ 0 & 0 & L_q & 0 & 0 & L_{qQ} \\ 0 & L_{fd} & 0 & L_f & L_{fD} & 0 \\ 0 & L_{Dd} & 0 & L_{Df} & L_D & 0 \\ 0 & 0 & L_{Qq} & 0 & 0 & L_Q \end{bmatrix}$$

All the elements of this matrix are constant which is their main advantage with respect to matrix (8). Besides it is symmetrical, too, because $L_{df}=L_{fd}$, $L_{dD}=L_{Dd}$ i $L_{qQ}=L_{Qq}$. The link between the inductivity of matrices (8) and (9) is the following:

$$L_d=l_\gamma+3/2(l_0+l_2)=l_\gamma+3/2l_d=l_\gamma+L_{ad};$$

$X_d=\omega L_d$ is a well-known synchronous reactance of the machine axis d;

$$L_q=l_\gamma+3/2(l_0-l_2)=l_\gamma+L_{aq}$$

$X_q=\omega L_q$ - the synchronous reactance of transversal axis q of the machine;

$L_0=l_\gamma$ -inductivities of the zero order

$$L_{df}=\sqrt{\frac{3}{2}}L_{af}$$

(L_{af} amplitude of the mutual inductivities $l_{af}=L_{af}\cos\theta$) and analogously:

$$L_{dD}=\sqrt{\frac{3}{2}}L_{aD}$$

$$L_{qQ}=\sqrt{\frac{3}{2}}L_{aQ},\ L_{fd}=L_{df},\ L_{fD}=$$

$$=L_{Df},\ L_f=L_{f\gamma}+L_{ff}$$

($L_{f\gamma}$ the inductivity of the scattering of an excitation winding f, L_{ff}-the total inductivity of the exciting winding) and analogously: $L_D=L_{D\gamma}+L_{DD}$, $L_Q=L_{Q\gamma}+L_{QQ}$.

If the reduction of the rotor size at the stator side [4] is made then we arrive at a simple reactance matrix:

$$[X]=\begin{bmatrix} x_0 & 0 & 0 & 0 & 0 & 0 \\ 0 & x_d & 0 & x_{ad} & x_{ad} & 0 \\ 0 & 0 & x_q & 0 & 0 & x_{aq} \\ 0 & x_{ad} & 0 & x_f & x_{ad} & 0 \\ 0 & x_{ad} & 0 & x_{ad} & x_D & 0 \\ 0 & 0 & x_{aq} & 0 & 0 & x_Q \end{bmatrix} \quad (9)$$

In synchronous machines with a roller rotor as well as in asynchronous machines the length of... is constant so that we can deem that l2=0; starting therefrom their inductivities and reactances are derived and calculated. In the transmission zone we will have: xd=xq i xad=xaq.

5. Conclusion

Starting from the inductivity definition between two phases of an asynchronous or synchronous machines, whose amplitudes are calculated by means of expressions (2), (3), (4) and (5), it is possible to calculate all the reactances used in the application of phase coordiantes or transformed magnitudes.

References

1. V.Vuckovic:General theory of electrical machines, (In Serbian).Nauka, Beograd,1992
2. A,V. Ivvanov-Smolenskih, "Electrical machines" (In Russian), Moscow, 1980.
3. J. Lesenne et al. "Introduction into a deep electrotechnics "(In French), textbook in Lille
4. D.Petrovic, "On relative units in electrical machines", 9th Symposium of Energetic electronics, Novi Sad, 1997.pp. 710-715.

Definition and Calculation of Reactances in Electrical Machines

Dr Dragan Petrovic

The Control of Interior Permanent Magnet Synchronous Motor Using a gopinath Observer

Part one: The Motor Model.

Vasile COMNAC[1] Mihai CERNAT[1]
Predrag PEJOVIĆ [2] Radu-Marian CERNAT[1]

[1]Faculty of Electrical Engineering, Transilvania University of Brasov

[2]Faculty of Electrical Engineering, University of Belgrade

The State Observer

Abstract:*The application of vector control techniques in a.c. drives demands accurate position and speed feedback information for the current control and servo-control loops. The paper describes a full mechanical sensorless speed digital control system for interior permanent magnet synchronous machines (IPMSM). A Gopinath state observer [1] is used for the mechanical state estimation of the motor. The observer was developed based on non-linear model of the synchronous motor, that employs a d-q rotating reference frame attached to the rotor*

.***Key words:*** *Field oriented control, Modelling, Permanent magnet motor, Sensorless control, Vector control.*

1. INTRODUCTION

The control schemes developed for high performance variable speed drives working on synchronous machines are based on control of the current space vector in a rotor frame of reference. This solution requires knowledge of the rotor shaft position for coordinate transformations and the necessary information on speed. In many applications, the rotor position signal is obtained from a mechanical sensor, such as an optical encoder or a resolver, that may reduce system reliability and add significantly to the drive costs [2]. Consequently a strong interest arises in the alternative PMSM mechanical sensorless control, using only stator voltage and current measurement, based on state observers [3-7].

Numerous papers is available on the use of complete order observers (Luenberger) for PMSM control [3, 4]. The present paper proposes implementation of the minimum order state observer (Gopinath) [1] a new type of state observers, easily applied in large order systems, that result consequently to accurate modeling of IPMSM or asynchronous machines. The main characteristic of this state observer is that the number of estimated states is lower than the order of the observed system. The main idea when building the Gopinath observer is to reduce the number of estimated variables, that is to diminish the observer dimension by using the measured output data provided by the system.

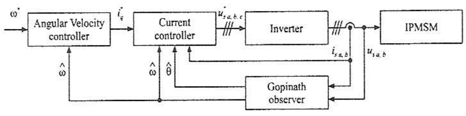

Fig. 1

Fig. 1 shows the simplified block diagram of the observer-based control system. The control system is a multi-sampled time system and consists in a fast inner loop current controller and observer, and a slower outer-loop angular velocity controller. The rotor-frame vector current controller combines feedforward compensation and a linear proportional-integral (PI) controller to control the torque of the machine. The I + PI angular velocity controller gives the reference of the quadrature component of the stator current (i_q^*). This paper considers the constant torque regime only. The state observer generates the estimated values of the actual rotor angular velocity ω and position θ, using the measured values of the currents and voltages from the motor terminals.

2. MOTOR MODEL

The studied IPMSM is supposed to have a symmetrical three-phase, wye-connected, isolated neutral winding. The model is developed according to some simplifying hypotheses.Thus, saturation and iron losses (hysteresis)are not considered. The induced electromotive force is supposed to have a sine form, while eddy currents are neglected. Since excitation is provided by permanent magnets, there is no variation of field currents and there is no rotor cage. Permanent magnets are buried in the rotor steel, so the machine is characterised by a cylindrical asymmetry causing the phase direct stator inductance L_d to be lower than the quadrature one L_q. The equations of the IPMSM dynamic model are strongly simplified when expressed in a rotating reference frame attached to the rotor, with *d*-axis oriented to the north-pole of the permanent magnet. In this case the state space model is described by the matrix equation:

$$\frac{\mathrm{d}}{\mathrm{d}t}\begin{bmatrix} i_d \\ i_q \\ \omega \\ \theta \end{bmatrix} = \begin{bmatrix} -\frac{R_s}{L_d} & 0 & 0 & 0 \\ 0 & -\frac{R_s}{L_q} & -p\frac{\Psi_e}{L_q} & 0 \\ 0 & \frac{k_m}{J} & -\frac{D}{J} & 0 \\ 0 & 0 & 1 & 0 \end{bmatrix}\begin{bmatrix} i_d \\ i_q \\ \omega \\ \theta \end{bmatrix};$$

$$++\begin{bmatrix} p\frac{L_q}{L_d}\omega i_q \\ -p\frac{L_d}{L_q}\omega i_q \\ \frac{k_{mi}}{J} i_d i_q \\ 0 \end{bmatrix} + \begin{bmatrix} \frac{1}{L_d} & 0 & 0 \\ 0 & \frac{1}{L_q} & 0 \\ 0 & 0 & -\frac{1}{J} \\ 0 & 0 & 0 \end{bmatrix}\begin{bmatrix} u_d \\ u_q \\ m_l \end{bmatrix}$$

$$k_m = \frac{3}{2} p \Psi_e; \quad k_m = \frac{3}{2} p (L_d - L_q), \qquad (1)$$

where (i_d and i_q) and (u_d and u_d) are the direct and quadrature components of the current and voltage respectively, with respect to the rotor frame; m_l - load torque; p - pole pair number; R_s - stator resistance per phase; Ψ_e - linkage flux of the PM; J - inertia; D - damping factor.

The motor parameters used in the real time simulation are: $p = 2$, $R_s = 0.98\ \Omega$, $L_d = 9.1$ mH, $L_q = 18.1$ mH, $\Psi_e = 0.174$ Wb, $J = 0.0086$ kgm^2.

The state-space model, described by equation (1), contains non-linearities in form of cross-product of two state variables such as $\omega \cdot i_d$, $\omega \cdot i_q$ and $i_d \cdot i_q$. This model cannot be described using the standard form of linear systems with state variables, so the linear observer theory cannot be applied directly. A possible procedure to control and estimate such non-linear systems could be the piece-wise linearisation, but the design would be in this case labourious and time consuming.

Considering the structure of the Gopinath observer, in the paper a model which uses measured currents in order to obtain a global linearisation is proposed. The non-linear system is at first transformed into a linear, time-varying one, in that the state variables vector is split so that the process variables to be effectively observed, are highlighted:

$$\boldsymbol{x} = [\omega \ \ \theta \mid i_d \ \ i_q]^{\mathrm{T}} = [\boldsymbol{x}_e^{\mathrm{T}} \ \ \boldsymbol{y}^{\mathrm{T}}]^{\mathrm{T}}, \qquad (2)$$

where the superior index T represents the algebraic transposition of the matrix.

Adopting the vector of the input variables:

$$\boldsymbol{u} = [u_d \ \ u_q \ \ m_l]^{\mathrm{T}}, \qquad (3)$$

the linearised model can be written in the compact form:

$$\frac{\mathrm{d}\boldsymbol{x}}{\mathrm{d}t} = \boldsymbol{A}\boldsymbol{x} + \boldsymbol{B}\boldsymbol{u}; \qquad \boldsymbol{y} = \boldsymbol{C}\boldsymbol{x}, \qquad (4)$$

with:

$$\mathbf{A} = \begin{bmatrix} -\frac{D}{J} & 0 & \frac{k_{mi}}{J}\tilde{i}_q & \frac{k_m}{J} \\ 1 & 0 & 0 & 0 \\ p\frac{L_q}{L_d}\tilde{i}_q & 0 & -\frac{R_s}{L_d} & 0 \\ -\frac{p}{L_q}\left(\Psi_e + L_d\tilde{i}_d\right) & 0 & 0 & -\frac{R_s}{L_q} \end{bmatrix};$$

$$\mathbf{B} = \begin{bmatrix} 0 & 0 & -\frac{1}{J} \\ 0 & 0 & 0 \\ \frac{1}{L_d} & 0 & 0 \\ 0 & \frac{1}{L_q} & 0 \end{bmatrix}$$

$$\boldsymbol{C} = \begin{bmatrix} 0 & 0 & 1 & 0 \\ 0 & 0 & 0 & 1 \end{bmatrix}, \qquad (5)$$

where $\tilde{i}_d$ and $\tilde{i}_q$ are the values of currents obtained by measuring and computing in dependence on angle θ.

3. STATE OBSERVER DESIGN

In order to develop the state observer structure, first auxiliary matrices:

$$\mathbf{A}_{11} = \begin{bmatrix} -\frac{D}{J} & 0 \\ 1 & 0 \end{bmatrix}; \quad \mathbf{A}_{12} = \begin{bmatrix} \frac{k_{mi}}{J}\tilde{i}_q & \frac{k_m}{J} \\ 0 & 0 \end{bmatrix}$$

$$\mathbf{A}_{21} = \begin{bmatrix} p\frac{L_q}{L_d}\tilde{i}_q & 0 \\ -\frac{p}{L_d}\left(\Psi_e + L_d\tilde{i}_d\right) & 0 \end{bmatrix};$$

$$\mathbf{A}_{22} = \begin{bmatrix} -\frac{R_s}{L_d} & 0 \\ 0 & -\frac{R_s}{L_q} \end{bmatrix}$$

$$\mathbf{B}_1 = \begin{bmatrix} 0 & 0 & -\frac{1}{J} \\ 0 & 0 & 0 \end{bmatrix}; \quad \mathbf{B}_2 = \begin{bmatrix} \frac{1}{L_d} & 0 & 0 \\ 0 & \frac{1}{L_q} & 0 \end{bmatrix} \qquad (6)$$

are written, obtained by splitting of matrices $\boldsymbol{A}$ and $\boldsymbol{B}$ of the linearised model, in the way imposed by the splitting of state variables vector $\boldsymbol{x}$.

The general equations of the Gopinath observer are [1, 5, 8]:

$$\frac{\mathrm{d}\boldsymbol{z}}{\mathrm{d}t} = \boldsymbol{F}\boldsymbol{x} + \boldsymbol{G}\boldsymbol{u} + \boldsymbol{H}\boldsymbol{y};\ \boldsymbol{x}_e = \boldsymbol{z} + \boldsymbol{L}\boldsymbol{y};$$

$$\boldsymbol{z} = [z_1 \ z_2]^{\mathrm{T}} \qquad (7)$$

where z is the state variables vector of the Gopinath observer, and

$$\boldsymbol{F} = \boldsymbol{A}_{11} - \boldsymbol{L}\cdot\boldsymbol{A}_{21};$$

$$\boldsymbol{G} = \boldsymbol{B}_1 - \boldsymbol{L}\cdot\boldsymbol{B}_2; \qquad (8)$$

$$\boldsymbol{H} = \boldsymbol{A}_{12} - \boldsymbol{L}\cdot\boldsymbol{A}_{22} + \boldsymbol{F}\cdot\boldsymbol{L}$$

$$\boldsymbol{L} = \begin{bmatrix} l_{11} & l_{12} \\ l_{21} & l_{22} \end{bmatrix} \qquad (9)$$

The unknown parameters of matrix $\boldsymbol{L}$ will be determined using the method of poles placement for matrix $\boldsymbol{F}$, that influences the dynamic behaviour of the observer.

Matrix $\boldsymbol{F}$ of the state observer is obtained by replacing relations (6 a), (6 c) and (9) in equation (8 a):

$$\mathbf{F} = \begin{bmatrix} -\frac{D}{J} - l_{11}\,p\frac{L_q}{L_d}\tilde{i}_q + l_{12}\frac{p}{L_q}\left(\Psi_e + L_d\,\tilde{i}_d\right) & 0 \\ 1 - l_{21}\,p\frac{L_q}{L_d}\tilde{i}_q + l_{22}\frac{p}{L_q}\left(\Psi_e + L_d\,\tilde{i}_d\right) & 0 \end{bmatrix} \qquad (10)$$

Observer poles allocation is extremely simple because the characteristic polynom:

$$P_0(s) = \det\left(s\,\mathbf{I}_2 - \mathbf{F}\right) =$$

$$= s\left[s + \frac{D}{J} + l_{11}\,p\frac{L_q}{L_d}\tilde{i}_q - l_{12}\frac{p}{L_q}\left(\Psi_e + L_d\,\tilde{i}_d\right)\right]$$

(11)

is a second order polynom with a nil root.

Selecting a convenient value for non-zero pole p_1 and

$$l_{11} = 0 \qquad (12)$$

there results:

$$l_{12} = -\left(p_1 - \frac{D}{J}\right)\frac{L_q}{p\,(\Psi_e + L_d\,\tilde{i}_d)}. \qquad (13)$$

and the other coefficients of matrix $\boldsymbol{L}$, were selected randomly - for example zero - because they do not influence the observer dynamics:

$$l_{21} = l_{22} \qquad (14)$$

Replacing relations (6 e), (6 f) in equation (8 b), and relations (6 b), (6 d) and (9) in equation (8 c) respectively and taking into account the relations (12), (13) and (14), are obtained:

$$\mathbf{G} = \begin{bmatrix} 0 & -\frac{l_{12}}{J} & -\frac{1}{J} \\ 0 & 0 & 0 \end{bmatrix};$$

$$\mathbf{H} = \begin{bmatrix} \frac{k_{mi}\tilde{i}_q}{J} & \frac{k_m}{J} + \frac{l_{12}R_s}{L_q} - l_{12}\left(\frac{D}{J} - l_{12}\frac{p}{L_q}\left(\Psi_e + L_d\,\tilde{i}_d\right)\right) \\ 0 & l_{12} \end{bmatrix}$$

(15)

Thus we obtain the final form of the Gopinath observer equations for estimating the angular velocity and the angular position for an IPMSM:

$$\frac{\mathrm{d}z_1}{\mathrm{d}t} = \left[-\frac{D}{J} + l_{12}\frac{p}{L_q}\left(\Psi_e + L_d\,\tilde{i}_d\right)\right]z_1 - \frac{l_{12}}{L_q}\tilde{u}_q - \frac{m_l}{J} + \frac{k_{mi}}{J}\tilde{i}_d\,\tilde{i}_q +$$
$$+\left(\frac{k_m}{J} + \frac{l_{12}R_s}{L_q}\right)\tilde{i}_q + l_{12}\left(-\frac{D}{J} + l_{12}\frac{p}{L_q}\left(\Psi_e + L_d\,\tilde{i}_d\right)\right)\tilde{i}_q;$$

(16)

$$\frac{\mathrm{d}z_2}{\mathrm{d}t} = z_1 + l_{12}\,\tilde{i}_q \qquad (17)$$

$$\hat{\omega} = z_1 + l_{12}\,\tilde{i}_q; \qquad \hat{\theta} = z_2 \qquad (18)$$

where $\tilde{u}_q$ is quadrature component of the voltage, measured and subsequently transformed in the rotor reference frame using the observed position.

4. REFERENCES

[1] B. Gopinath, "On the Control of Linear Multiple Input-Output Systems", *The Bell Journal*, vol. 50 (1971), pp. 1063-1081.

[2] P. Vas, "*Vector Control of AC Machines*", Clarendon Press, Oxford, 1980.

[3] L. A. Jones, J. H. Lang, "A State Observer for Permanent Synchronous Motor", *IEEE Transactions on Industry Applications*, No. 3, August 1989, pp. 374 –382.

[4] R.B. Sepe, J. H. Lang, "Real-Time Observer-Based (adaptive) Control of a Permanent Magnet Synchronous Motor without Mechanical Sensors", *IEEE Transactions on Industry Applications*, vol 28, No. 6, November/December 1992, pp. 1345-1352

[5] M. Voicu, "*Sisteme automate multivariabile. Metode de proiectare in frecventa. (Multivariable control systems. Frequency design methods)*", Editura Gheorghe Asachi, Iasi 1993 (in Romanian).

[6] S. Morimoto, M. Sanada, Y. Takeda, "Wide-Speed Operation of Interior Permanent Magnet Synchronous Motor with High-Performance Current Controller", *IEEE Transactions on Industry Applications*, vol 30, No. 4, July/August 1994, pp. 920-926.

[7] N. Matsui,"Sensorless Brushless d.c. Motor

Drives",*Proceedings of the 7th International Power Electronics & Motion Control Conference - PEMC '96*, Budapest, sept. 1996, vol. II, pp.9-12.

[8] V. Comnac, *"Contributii la studiul sistemelor de actionare cu miscare incrementala cu masini sincrone cu magneti permanenti (Contributions to the Study of Incremental Motion Drive Systems with Permanent Magnet Synchronous Machines)*", Doctoral thesis, *Transilvania* University of Brasov, 1998 (in Romanian).

[9] V. Comnac, M. Cernat, Fl. Moldoveanu, C. Suciu, R. M. Cernat, "The Control of an Interior Permanent Magnet Synchronous Machine Using a Gopinath Observer", *3rd International Scientific Conference ELEKTRO '99*, Zilina (Slovakia), 25-26 May, 1999, Vol I, pp. 27-32.

[10] M. Cernat, V. Comnac, P. Pejovic, R.-M. Cernat, " The Control of Interior Permanent Magnet Synchronous Motors Using a Gopinath Observer", *10th Symposium on Power Electronics-Ee '99*, Novi Sad (Yugoslavia), November 3-5, 1999.

The Control of Interior Permanent Magnet Synchronous Motor Using a gopinath Observer
Part two: The Control System.

Mihai CERNAT[1] *Vasile COMNAC*[1]
Predrag PEJOVIĆ[2] *Radu-Marian CERNAT*[1]

[1]Faculty of Electrical Engineering, *Transilvania* University of Brasov

[2]Faculty of Electrical Engineering, University of Belgrade

Abstract: *The paper describes a full mechanical sensorless speed digital control system for interior permanent magnet synchronous machines (IPMSM). A Gopinath state observer [7] is used for the mechanical state estimation of the motor. The control system includes a rotor frame vector current controller with feedforward decoupling circuit and an integral+integral proportional (I + PI) speed controller.*

Key words: Field oriented control, Modelling, Permanent magnet motor, Real time simulation, Sensorless control, Vector control.

1. CURRENT CONTROLLER

Fig. 1 show the block diagram of the control structure of stator currents. The detailed structures of the blocks labeled "MVCC" and "DCRG" are presented in fig. 2 and fig. 3, respectively. To achieve a fast response with high performances, a control strategy of the currents in the two-phase rotor frame (d-q) with feedforward decoupling was used [2, 5, 6].

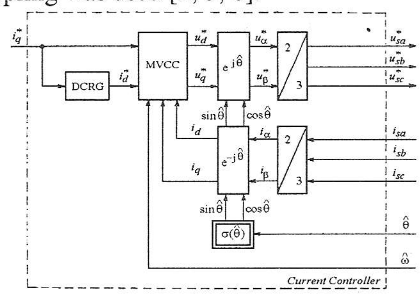

Fig. 1

Fig. 2 shows the block diagram of the multi-variable current controller, block labeled "MVCC" in fig. 1, where $G_{rd}(s)$ and $G_{rq}(s)$ are transfer functions of the PI type individual controllers. The recurrent algorithm of this control structure is obtained using the Euler's discrete integrating method:

$$\varepsilon_{id}(n+1) = i_d^*(n+1) - i_d(n+1); \quad \varepsilon_{iq}(n+1) = i_q^*(n+1) - i_q(n+1) \tag{1}$$

$$x_d(n+1) = x_d(n) + \frac{T_{ei}\,k_{rid}\,\varepsilon_{id}(n)}{T_{rid}}; \quad x_q(n+1) = x_q(n) + \frac{T_{ei}\,k_{riq}\,\varepsilon_{iq}(n)}{T_{riq}} \tag{2}$$

$$u_d^*(n+1) = x_d(n+1) + k_{rid}\,\varepsilon_{id}(n+1) - L_q\,\omega(n+1)\,i_q(n+1) \tag{3}$$

$$u_q^*(n+1) = x_q(n+1) + k_{riq}\,\varepsilon_{iq}(n+1) + \Psi_e\,\omega(n+1) + L_d\,\omega(n+1)\,i_d(n+1) \tag{4}$$

where $x_{d,q}$ are the auxiliary variables associated to the integrator, T_{ei} is the sampling period of the stator currents control loops, n - the index of the sampling period T_{ei}, $k_{rid,q}$ and $T_{rid,q}$ are the tuning parameters of the two current controllers.

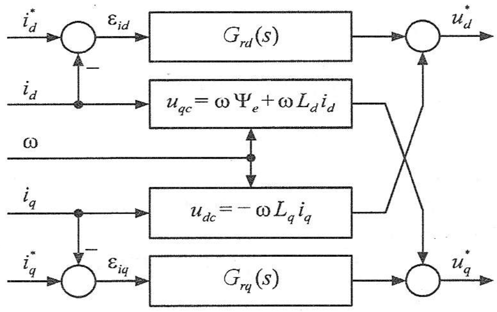

Fig. 2

The reference quantity for the quadrature component of the stator current (i_q^*) is obtained directly from the output of the rotor speed controller. The reference quantity for the direct component of the stator current (i_d^*) will be calculated such as to maximise the electromagnetic torque to absorbed current ratio. For constant torque regime, this can be obtained if the reference values of the stator direct current satisfy the relation [3, 4]:

$$i_d = \frac{i_e - \sqrt{i_e^2 + (k_L\, i_q)^2}}{k_L}; \qquad i_e = \frac{\Psi_e}{L_q};$$

$$k_L = 2\left(1 - \frac{L_d}{L_q}\right) \tag{5}$$

valid if

$$i_{sd}^2 + i_{sq}^2 = i_{stator}^2 < I_0^2 \tag{6}$$

where i_{stator} is the stator current and I_0 is the maximum admitted current of the inverter dc link.

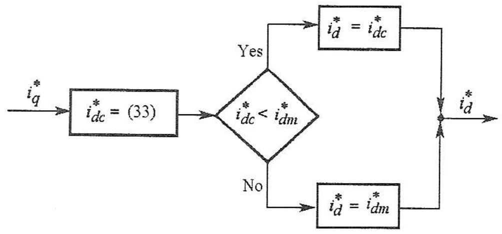

Fig.3

The direct current must be limited to the value:

$$i_{dm} = \frac{i_e - \sqrt{i_e^2 + 2\,(k_L\, I_0)^2}}{2\, k_L} \tag{7}$$

In this case, the electromagnetic torque produced is expressed by [4]:

$$m_e = \frac{3}{8} p \Psi_e \sqrt{I_0^2 - i_{dm}^2}\left[3 + \sqrt{1 + 2\left(\frac{k_L\, I_0}{i_e}\right)^2}\right] \tag{8}$$

The relations (5) -(8) are valid for actual values of the currents i_d and i_q and also for reference values i_d^* and i_q^*. The algorithm for the computing of the stator direct current reference, implemented in the block labeled "DCRG" in fig. 1, is represented in Fig. 3.

2. ANGULAR VELOCITY CONTROL

The angular velocity controller has an important influence on the performances of the entire control system during both transient and steady state regimes. Good performances could be achieved using an I type control law for the angular velocity reference quantity ω^*, and a PI control law for the angular velocity feedback ω respectively. The I + PI controller will operate with both these laws.

The main advantage of an I + PI controller is the achievement of good performances in transient regime and, at the same time, due to the unitary discrete pole, a nil stationary error with respect to the perturbation of the load torque (including the friction torque of the machine). The block diagram of this controller – using z-transfer functions is presented in fig. 4. It can be noticed that the integration used the trapeze method.

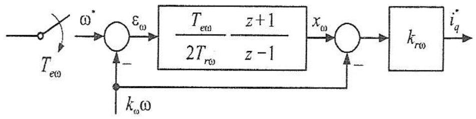

Fig. 4

The controller algorithm, obtained applying the inverse Z transform, is described by recurrent equations:

$$\varepsilon_\omega = \omega^*(n+1) - k_\omega\, \omega(n+1) \tag{9}$$

$$x_\omega(n+1) = x_\omega(n) + \frac{T_{e\omega}}{2\, T_{r\omega}}\left[\varepsilon_\omega(n+1) - \varepsilon_\omega \omega(n)\right] \tag{10}$$

$$i_q^*(n+1) = k_{r\omega}\left[x_\omega(n+1) - k_\omega\, \omega(n+1)\right] \tag{11}$$

where: $\varepsilon_\omega, x_\omega$ -the auxiliary variables associated to angular velocity loop error, and to the integrator respectively; $k_{r\omega}, T_{r\omega}$ -the tuning parameters of the angular velocity controller; k_ω - the transfer factor of the angular velocity transducer, n - the index of the sampling period, $T_{e\omega}$.

2. DESIGN OF THE OBSERVER-BASED CONTROL SYSTEM

This section integrates the observer with the current and angular velocity controller. The internal current loops and the observer use a sampling period of $T_{ei} = 0.5\,\text{ms}$, whereas the outer-loop angular velocity controller operates with a sampling period $T_{e\omega} = 3\,\text{ms}$.

The actual values of the stator current components are obtained using the measured values of the phase currents, then they are transformed from the three-phase system into a two-phase stationary reference frame, and then into a rotor two-phase frame using the estimated rotor angle $\hat{\theta}$. For this reason in equations (1), (3), and (4), i_d and i_q are replaced by $\tilde{i}_d$ and $\tilde{i}_q$.

In a similar way - but with the transformation made in reverse order - the values of the reference quantities of the phase stator voltages could be obtained. Voltages u_d^* and u_q^* are calculated with relations (3) and (4), by replacing ω by the estimated value $\hat{\omega}$. The slower outer-loop angular velocity controller requires, also replacement of ω by the estimated angular velocity $\hat{\omega}$ in its control law (9) - (11).

For a good behaviour of the control system, an optimum tuning of the current and rotor angular velocity controllers parameters is required.

The selection of the parameters for current controllers is carried out similarly to continuous systems - considering the two control loops linear and decoupled - due to the feedforward compensation and to the small sampling period of the current loops.

The model for the controlled process of the rotor angular velocity loop is obtained using the discrete form of the closed-loop quadrature current transfer function, that is approximated by a first order delay element. The selection of parameters for the angular velocity controller is achieved using the discrete version of the extended modulus criterion. The load torque and the damping factor are neglected in the controller design. The application way of this design technique and the equations for controller parameters are presented in detail in [4].

3. ANALYSIS OF THE CONTROL SYSTEM

The analysis of the control system was carried out using real time simulation in the conditions mentioned above. The angular velocity reference quantity has a trapeze variation shape specific to incremental motion servo-drives.

The load and the viscous friction torque are taken into consideration in the simulated machine model ($m_l = 1$ Nm and D = 0.002 Nms/rad). The synchronous machine is supplied from a 12 kHz PWM converter. The mechanical and electrical waveforms are presented in fig. 5 a, b.

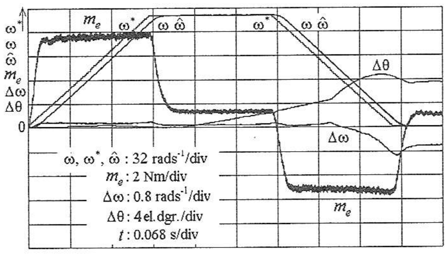

Fig. 5a

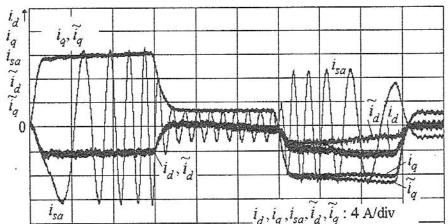

Fig. 5b

They were obtained assuming the mechanical and electrical parameters of the electrical drive known and constant. Also, an exact initialisation of the observer position is considered. Under these circumstances, it is noticed that the estimation errors of the rotor angular velocity $\Delta\omega = \omega - \hat{\omega}$ and rotor position $\Delta\theta = \theta - \hat{\theta}$ are acceptable.

The variation of the machine electrical parameters influences only in a relatively small proportion the performances of the observer-based control system. This aspect can be noticed in fig. 6 a, b, that present the same waveforms as in fig. 5 a, b but in this situation stator resistance is twice as big as the rated ($R_s = 2R_{sN}$) and inductance 40% smaller than the rated values. The observer-based system is very sensitive to mechanical parameters variations. In these situations the observer-based control system becomes unstable.

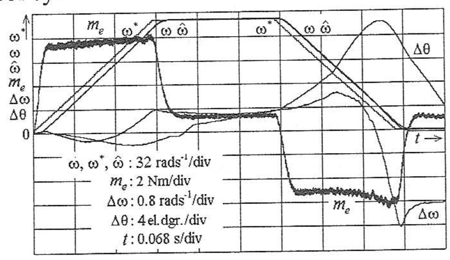

Fig. 6a

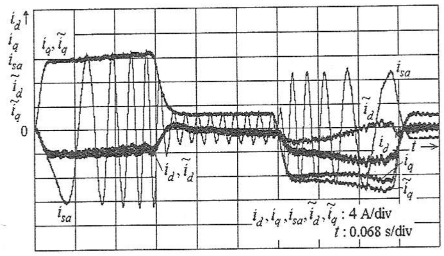

Fig.6b

The simulations show that the proposed structure is not capable of eliminating the incorrect position initialisations, even at small values of the initial estimation error. For this reason it is necessary to determine the initial rotor position with an alternative method, like the one presented in [1].

4. CONCLUSIONS

The paper develops a mechanical sensorless digital control system of the rotor speed for a IPMSM. Mechanical state estimation is achieved by using a minimum order observer (Gopinath). The paper studies the interaction between the observer and the closed loop control system.

The validation of the proposed control system is achieved by real time simulation in C++, under the natural operation circumstances, using the estimated quantities as feedback signals for the control system.

The simulation shows that the dynamic behaviour of the observer based control system is acceptable, even if the electrical parameters of the machine are different from the rated values used for the design of the controllers and observer.

The control system is very sensitive to the incorrect initialisation of the estimated position and to mechanical parameter variation (inertia, load torque).

5. REFERENCES

[1] M. Schrödl, "Control of aPermanent Magnet SynchronousMachine Using a New Position Estimator", *International Conference on Electric Machine*, Cambridge, Massachusetts, USA, 1990, pp. 1281-1284.

[2] M. Voicu, "*Sisteme automate multivariabile. Metode de proiectare in frecventa. (Multi-variable control systems. Frequency design methods)*", Editura Gheorghe Asachi, Iasi 1993 (in Romanian).

[3] S. Morimoto, M. Sanada, Y. Takeda, "Wide-Speed Operation of Interior Permanent Magnet Synchronous Motor with High-Performance Current Controller", *IEEE Transactions on Industry Applications*, vol 30, No. 4, July/August 1994, pp. 920- 926.

[4] V. Comnac, "*Contributii la studiul sistemelor de actionare cu miscare incrementala cu masini sincrone cu magneti permanenti (Contributions to the Study of Incremental Motion Drive Systems with Permanent Magnet Synchronous Machines)*", Doctoral thesis, *Transilvania* University of Brasov, 1998 (in Romanian).

[5] V. Comnac, M. Cernat, Fl. Moldoveanu, C. Suciu, R. M. Cernat, "The Control of an Interior Permanent Magnet Synchronous Machine Using a Gopinath Observer", *3rd International Scientific Conference ELEKTRO '99*, Zilina (Slovakia), 25-26 May, 1999, Vol I, pp. 27-32.

[6] V. Comnac, M. Cernat, Fl. Moldoveanu, I. Draghici, R. M. Cernat, R. Ungar, "The Control of Interior Permanent Magnet Synchronous Machine Using a Non-Linear Minimum Order Observer", *20tth International Conference"Power Electronics,Drives and Motion"- PCIM '99,* Nürnberg (Germany), 22-24 June,1999, vol II, pp

[7] V. Comnac, M. Cernat, P. Pejovic, R.-M. Cernat, " The Control of Interior Permanent Magnet Synchronous Motors Using a Gopinath Observer", *10th Symposium on Power Electronics-Ee '99,* Novi Sad (Yugoslavia), November 3-5, 1999.

A NOVEL HYSTERESIS CURRENT REGULATOR IN POWER FACTOR CORRECTION CIRCUITS

Predrag Ninković, EE Institute Nikola Tesla, Belgrade, Yugoslavia

Abstract: *This paper investigates two methods of improving the hysteretic current control of the single-phase power factor correction (PFC) circuits. New controllers achieve reduced switching frequency range, while preserving excellent dynamics. Theoretical analysis is performed and verified by experiment on the 700W boost-type single-phase circuit.*

Keywords: *Power factor / Current regulation / Boost converter / Hysteresis current controller.*

1. INTRODUCTION

In recent years, nonlinear loads are extensively used in industry and home appliances [1,2]. Utilization of such consumers started when it was recognized that switching power converters significantly improve energy efficiency of power supply for every device used. As a consequence, input current drawn from the utility line is distorted in a high degree. Then, problems associated with harmonic currents arise. Any action toward group compensation has limited success, due to the undeterministic positioning of these loads. Therefore, the only positive solution is to apply utility interfaces that can achieve the primary task: sinusoidal input current in phase with the line voltage. As a final result, the unity power factor is achieved and those interface circuits are called power factor correction (PFC) circuits.

The majority of nonlinear consumers are single-phase devices, with power levels of 50W up to 3kW. That is why it is very important to prevent problems caused by harmonic currents. For power levels of 600W and higher, it is a common practice to use PFC circuits consisting of the full-bridge diode rectifier followed by one single-switch nonisolated boost converter operating in continuous conduction mode (CCM) [3]. The schematic of the converter is shown in Fig.1. Input current of the circuit is regulated by inductor current regulation loop, and at the final stage the current tracks the reference value. The current-loop is usually implemented as average current-mode or hysteretic regulation [4,5].

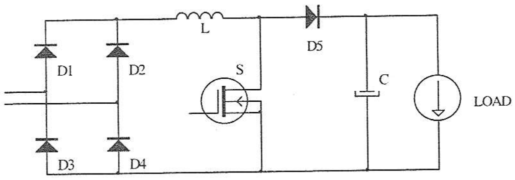

Fig.1: *The conventional single-phase PFC circuit*

Average current-mode [4,6] operates at constant switching frequency. Tuning the regulator is not an easy process, and if the switching frequency is not high enough, the regulation error appears, because of the problems in AC component tracking. On the other hand, fast switching at high voltage (typically 400V) and high power increases losses and problems related to noise.

Hysteretic regulation [2, 7] is inherently fast and stable. Regulation is quite simple and easy to implement. However, switching frequency is not constant and, what is more important, it can vary in a very wide range, depending on power and voltage level. The input current harmonic content becomes unpredictable, so good filtering is hard to achieve. Also, thermal calculations are made very difficult.

This paper presents a study of possibility to modify the hysteretic current regulation so the switching frequency range is significantly reduced. Moreover, it should be made independent of load power level. Two practical solutions are proposed: one is very simple with moderate improvements, and the other gives excellent results but with somewhat complex regulation circuitry.

2. THEORETICAL BACKGROUND

Hysteretic regulation is based on the principle of limiting the excursion of the regulated value from the reference value [2, 7]. Fig.2 illustrates the principle in the case of inductor current regulation. The solid line represents the inductor current moving around the reference value I_{ref}. It is quite common that the level of excursion is symmetrical in both positive and negative side, and this level is called hysteresis window H.

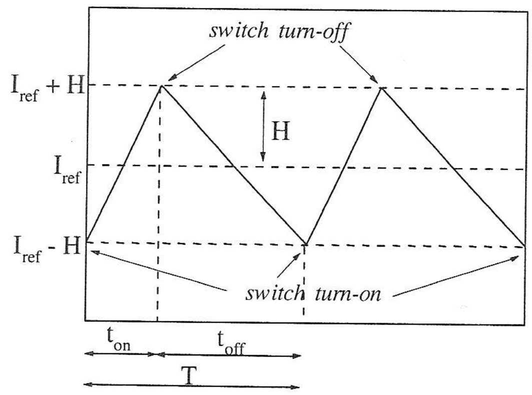

Fig.2: *Hysteretic inductor current regulation principle*

By inspection, it is easy to conclude that:

$$L \cdot \frac{2H}{t_{on}} = V_{on}(t), \quad L \cdot \frac{2H}{t_{off}} = V_{off}(t), \quad (1)$$

where:
L is the inductance value
t_{on} is the switch-on time
t_{off} is the switch-off time
V_{on} is the inductor voltage during t_{on}
V_{off} is the inductor voltage during t_{off}

In the case of ideal components, the following expressions are valid:

$$V_{on}(t) = V_{in}(t) = |V_m \sin \omega t|$$
$$V_{off}(t) = V_{out}(t) - V_{in}(t) = V_{out}(t) - |V_m \sin \omega t| \quad (2)$$

where:

$V_{in}(t)$ is the input (rectified line) voltage
V_m is the line voltage amplitude, and
V_{out} is the output (DC) voltage.

When the switching frequency is at least an order of magnitude higher than the line and output voltage frequency, then H can be considered constant during the switching frequency period T. Rearranging (1) and (2) gives the expression for the switching frequency change in time $f_{sw}(t)$ as:

$$f_{sw}(t) = \frac{1}{T} = \frac{1}{t_{on} + t_{off}}$$
$$= \frac{|V_m \sin(\omega t)| \cdot \left(1 - \frac{|V_m \sin(\omega t)|}{V_{out}(t)}\right)}{2LH}. \quad (3)$$

For the analysing purposes, the output voltage will be considered constant despite the presence of ripple at twice the line frequency. This ripple will cause some inaccuracy, yet in well designed converters the ripple magnitude is small and neglecting it can be quite reasonable.

Traditionally, the constant value of hysteresis window H was the most commonly used, but it caused very high switching frequency range. An improvement was made with the use of variable window $H=H(t)=H\cdot \sin(\omega t)$ [7], but the frequency range remained high. A great number of adaptive hysteresis regulators were reported in literature, but they were commited to applications which are different from PFC subject. Therefore, to modify the hysteretic regulation for PFC purposes, it is necessary to thoroughly analyse the equation (3).

3. MODIFICATION

Equation (3) implies that, if the window H is load independent, then the switching frequency will be independent of load, too [8]. Since there are two variable parts, three possible solutions for variable H can be derived:

a) $H=H(t)=K\cdot V_{in}(t)$, (4)

b) $H=H(t)=K\cdot(1-V_{in}(t)/V_{ref})$, (5)

c) $H=H(t)=K\cdot V_{in}(t)\cdot(1-V_{in}(t)/V_{ref})$. (6)

In the continuation of this section each of these methods will be analyzed.

3.1 Analysis of method a

When (4) is substituted in (3), the following expression is obtained:

$$f_{sw}(t) = \frac{1 - \frac{|V_m \sin(\omega t)|}{V_{out}}}{2LK}. \quad (7)$$

Then, the switching frequency range K_f can be derived from (7) as:

$$K_f = \frac{f_{sw,\max}}{f_{sw,\min}} = \frac{1}{1 - \frac{V_m}{V_{out}}}, \quad f_{sw,\max} = \frac{1}{2LK}. \quad (8)$$

From (7), it is obvious that the maximum frequency is constant for given K, but the minimum frequency depends on the line voltage. K_f increases as the line voltage increases. For typical output voltage of 400V and line voltage of 220V RMS, K_f is equal to 4.5, which is very acceptable.

3.2 Analysis of method b

When (5) is substituted in (3), it turns out that the switching frequency variation in time can be expressed as:

$$f_{sw}(t) = \frac{1}{2LK} \cdot \left| V_m \sin(\omega t) \right| \quad . \tag{9}$$

It is obvious that this solution is unacceptable because very low frequency content is present, which is extremely hard to filter without affecting the fundamental. Therefore, this method will be considered impractical and will not be discussed any more.

3.3 Analysis of method c

When (6) is substituted in (3), the following expression is obtained:

$$f_{sw}(t) = \frac{1}{2LK} = const \quad , \tag{10}$$

meaning that constant switching frequency is achieved. In practice, the output voltage ripple causes some deviation from the constant, but the smaller the ripple the less variable frequency is. Including the ripple effect, the switching frequency will be:

$$f_{sw}(t) = \frac{1}{2LK} \cdot \frac{1 - \dfrac{\left| V_m \sin(\omega t) \right|}{V_{out}(t)}}{1 - \dfrac{\left| V_m \sin(\omega t) \right|}{V_{ref}}} \quad . \tag{11}$$

The frequency range K_f is then equal to:

$$K_f = \frac{1 - \dfrac{V_m}{V_{ref} + \Delta V}}{1 - \dfrac{V_m}{V_{ref} - \Delta V}} \quad , \tag{12}$$

For example, if the line voltage is of nominal value of 220V RMS, the output voltage of 400V and output voltage ripple of 20V (ΔV=10V), K_f is equal to 1.19. The switching frequency range is significantly reduced so the filtering and thermal calculations are made easy.

4. EXPERIMENTAL RESULTS

In order to verify the conclusions from the previous section, an experimental converter was built with the following parameters:

- line voltage 105.7V/50Hz (autotransformer output),
- output voltage 220V,
- resistive load of approximately 700W (electric heater),
- hall-effect current sensor with overall transfer ratio R_s=0.5,
- inductance value L=2mH,
- output capacitor value C=1000μF.

Regulation circuit was completely made in analog technique. For the regulation purposes, a signal transformer was connected to the line voltage and its output was used for hysteresis window generation. All data were recorded by 8-bit digital storage oscilloscope. The switching frequency was measured using 8-bit microcontroller. The microcontroller was measuring the time duration between two succeeding switch-on signals, and then converting it into a switching frequency. Finally, the frequency value was converted into an analog signal using 8-bit D/A converter. The switching frequency was chosen low in order to avoid the influence of measurement resolution and electronic circuitry delay. The analog signal of switching frequency was limited by software to 25.5kHz.

4.1 Experiment with method a

In this case, K was taken as K=1/38. Then, using (7), the maximum switching frequency is equal to 9.5kHz and frequency range equals K_f=3.12.

Fig.3 shows the hysteresis window analytical and experimental waveform. Fig.4 shows the inductor current waveform together with its reference value. The symmetrical hysteretic action is clearly observed.

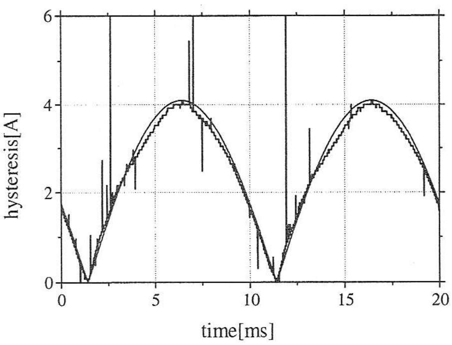

Fig.3: *Hysteresis window waveform, analytical and experimental*

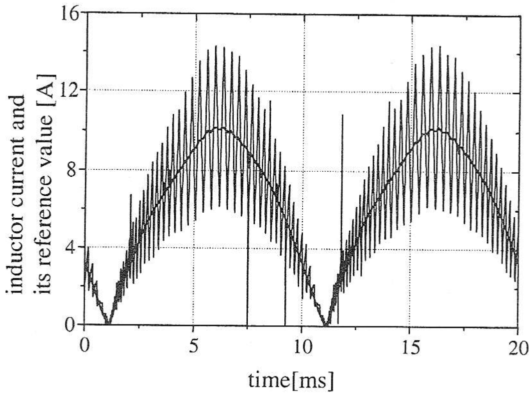

Fig.4: *Inductor current and its reference value waveforms*

Fig.5 shows analytical and experimental results for the switching frequency variation in time. Results are in close agreement except at the input voltage zero-crossing region. As the current approaches zero, its downslope is determined by the inductance and decreasing is slow, so the switch is turned-off for extended period of time and the switching frequency gets smaller. As the current and the window H value go bellow the sensor and electronics sensitivity level (due to the offset), the switching frequency is determined by internal oscillation of the control circuit until the current comes out of that region. The minimum switching frequency in this experiment was 2.9kHz, which is close to the theoretical value of 3.04kHz.

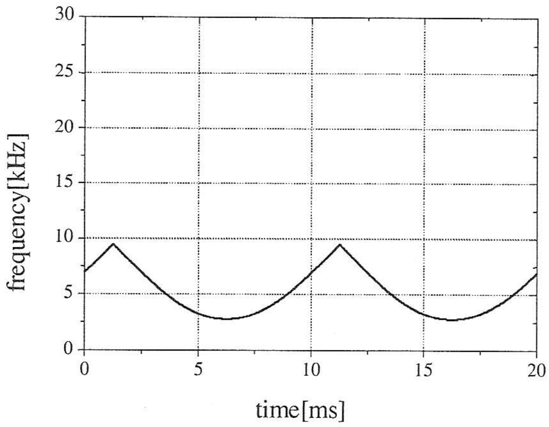

a)

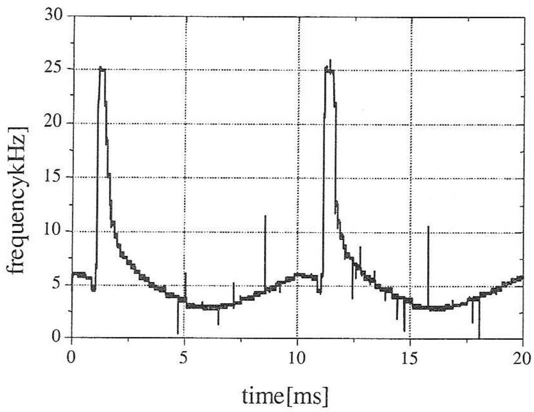

b)

Fig.5: *Analytical (a) and experimental (b) switching frequency variations in time*

4.2 Experiment with method c

The final hysteresis value in time is equal to:

$$H(t) = K \cdot V_{in}(t) \cdot \left[1 - \frac{V_{in}(t)}{V_{ref}}\right] \quad . \qquad (13)$$

This expression implies the use of a one-quadrant multiplier. It increases the complexity and the cost of the regulation circuitry. For his experiment, and old analog multiplier MC1594L [9] was used which is hard to accurately compensate, so the offset compensation was performed only approximately. Also, the same scaling factor was chosen K=1/38. Theoretically, the switching frequency should be constant f_{sw}=9.5kHz. Fig.6 shows both the analytical and experimental values of hysteresis window H. The difference between them is due to the non-ideal compensation of the multiplier. Fig.7 shows inductor current waveform and its reference value. Fig.8 shows analytical and experimentally determined switching frequency. As expected, the frequency is moving around its average value due to the non-zero output voltage ripple and hysteresis window deviation from the analytical value. The minimum switching frequency is equal to $f_{sw,min}$=8.8kHz and the maximum is $f_{sw,max}$=9.72kHz resulting in the switching frequency range of K_f=1.1. Experimental results agree with the analytical except at the zero-current region where the effect described in section 4.1 occurs.

It can be concluded that this method gives very effective solution because the switching frequency variation is decreased to 5% of the average value. Also, the average value is independent of load and input voltage, and can be easily controlled by only one variable K. This significantly improves the filtering and thermal design. Considering other good features (stability, accuracy and speed), this method presents an excellent choice for the high power load, since high switching frequency is not required.

5. CONCLUSION

In this paper, a methodology is presented how to modify the hysteretic current regulation in single-phase PFC circuits in order to decrease the switching frequency variation. Two methods are presented and the following improvements are made: in the first case, very small investment in control circuitry gives the switching frequency range of 6:1 in worst case operation; in the second case, the frequency range is reduced down to 1.2:1, but at the price of more complex control circuit. In addition to the well-known superior characteristics of the hysteresis current control, these new solutions can be alternative to the conventional control.

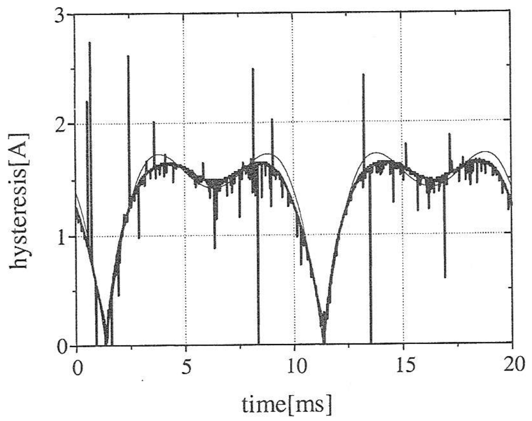

Fig.6: *Analytical and experimental waveforms for hysteresis window H*

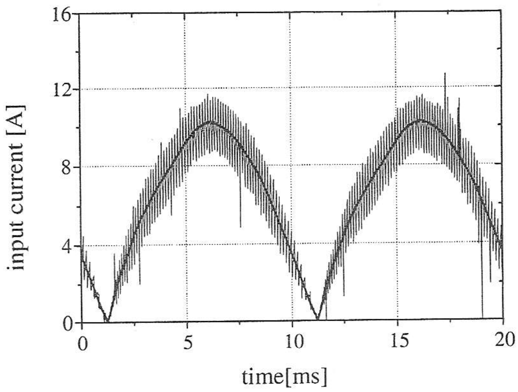

Fig.7: *Inductor current and its reference value waveforms*

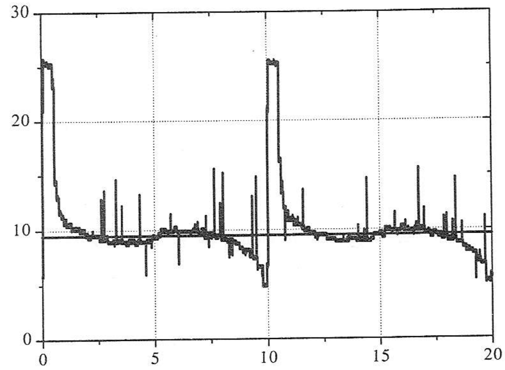

Fig.8: *Switching frequency waveform: analytical (straight line) and experimental*

The proposed methods can be applied in three-phase PFC circuits, and due to the duality principle, they can be applied in DC/AC converter circuits with appropriate modifications.

6. REFERENCES

[1] R.Redl, P.Tenti, J.D.Van Wyk, "Power Electronics' polluting effects", IEEE Spectrum, May 1997, pp.33-39.

[2] N.Mohan, T.M. Undeland, W.P. Robbins, "Power Electronics, Converters, Applications and Design", John Wiley and Sons, New York, 1995.

[3] P.Pejović,V.Božović, "Active Power Factor Correction By Boost Converter", Elektroprivreda, No.2, april-june 1997, pp. 28-33.

[4] L.Dixon, "Average Current Mode Control of Switching Power Supplies", Unitrode application note U-140.

[5] R.B.Ridley, "Average Small-Signal Analysis of the Boost Power Factor Correction Circuit", Proceedings of the Virginia Power Electronics Center Seminar, Blacksbutgh, VA, September 25-27, 1989, pp.108-120.

[6] P.C.Todd, "UC3854 Controlled Power Factor Correction Circuit Design", U-134 Unitrode Application Note.

[7] M.A.Rahman et al, "Analysis of Current Controllers for Voltage-Source Inverter", IEEE Trans. On Industrial Electronics, Vol.44, No.4, August 1997, pp.477-485.

[8] P.Ninkovic, "A New Hysteresis Current Regulator in Power Factor Correction Circuits", Proceedings of the 10th Power Electronics Symposium EE'99, October 14-16 1999, Novi Sad, Yugoslavia, pp.446-452 (in Serbian).

[9] Motorola Linear Integrated Circuits Data Book, 1973

ADAPTIVE ALGORITHM FOR DISTRIBUTION NETWORK ELECTRIC VALUES MEASUREMENT

Predrag Petrović, Technical Faculty Cacak, Yugoslavia
Slavoljub Marjanović, Faculty of Electrical Engineering, Belgrade, Yugoslavia

Abstract: *This paper present a novel design of a high accuracy watthourmeter based on use of very slow, high precision and cheap dual slope A/D converters. Measurements of voltage and current are made in successive periods and the output reconstructed by a stroboscopic technique (synchronous undersampling). The assumed stationary of the electric utilities is validated by measurements with an experimental setup, consisting of a fast high precision sigma-delta ADC. The necessary synchronization is reached by software measurements of the frequency of the measured signal. Measurements performed on the electric utilities in Yugoslavia indicate that the voltage and current waveform remains unchanged while the required accuracy is maintained, so the error made when sampling during several periods is below the value required for class 01 instruments.*

I INTRODUCTION

Abundant literature bears witness to the significance of electric utilities parameters (current, voltage, phase, power, energy, frequency). Even in 1974 Turgel [1] designed a digital wattmeter based on simultaneous sampling of current values of power and current in precisely defined time intervals. In [2] basic principles of digital signal processing, filtering, convolution processing, FFT processing and decimation are given. Srinvasan [3] described the sensitivity of a measuring system to variations of the system's frequency, while in [4] an original model was described as an analog system performing calculations on discrete values of voltage and current based on digital approximations of the analog scheme. Toivonen and Morsky [5] suggested a new multrate algorithm which required a periodic input signal and sampling synchronization and used a digital low pass filter implemented into a decimator instead of integration or summation used in conventional measuring methods. In [6] a new algorithm suggested, based on multifunction correlators, while Xi and Chichapo [7] investigate the influence of inaccuracy in the sampling period on the correctness of active power measurements in electric utilities.

The measuring method suggested in this paper is based on selecting samples of input variable in a large number of periods in which the electric utilities is considered to be inertial, which has been proved by values obtained from measurements of RMS values of system voltage (results presented in table 1). The current makes this system nonlinear due to the fact that one cannot predict in advance the type of load which will be used and when it will be connected to the investigated system. However, after a certain number of periods the current can be considered a slowly chaining variable during processing. This has been proved by simulation.

Considering all the stated facts it is clear that the interval needed to perform correct processing of alternating variables becomes very short from the viewpoint of inertia of such a large system as the electric utilities. This has been completely proved by measurements and experiments performed later. Measuring time is about 1 minute. Different from the technique of synchronous sampling this is done with much less frequency of sampling compared to the one from Nyquist criteria.

II THE PROPOSED ALGORITHM

The analyzed system is by its nature inert so it enables sampling during several periods of the observed system variables. This is why slow, low cost, but very accurate A/D converters, such as a "dual slope" type, were used in the proposed measuring system. Dual slope is integrating A/D converter, uses an integrator connected to a reference voltage to generate an analogue value, which is compared with the input analogue value by a comparator. The time taken for the output ramp of the integrator to reach the input signal level than gives the binary solution. Only the accuracy of the reference voltage influences the conversion accuracy of this converter. A standard dual slope A/D converter operates with a sampling frequency between 4 and 96 Hz, depending on the input amplitude. Voltage and current from real electric utilities were used as input variables. In the described system, voltage and current samples were taken in arbitrarily defined moments:

$$t_{delay} = NT + \Delta t$$

Where N is the number of periods between sampling, T is the period of the input voltage and Δt is the delay determined by the delay of elements in the processing circuit. Δt depends of harmonic content of input signal. For that reason it can not be arbitrary.

Average power is measured according to the following equation:

$$P = \frac{1}{n}\sum_{k=1}^{n} u(k)i(k) \qquad (1)$$

where n is an arbitrary number determined by the number of samples needed for a precise reconstruction of the measured value. The obtained value for average power is compared during the simulation with the average power determined using the definition for mean average power:

$$P = \frac{1}{T}\int_{0}^{T} u\,i\,dt \qquad (2)$$

where T is the period of the input voltage.

The problem of noise that can occur in a real system, as averaging is performed to determine the average power is not considered important as the average noise value is zero. The possible nonlinear distortions in transition processes do not last very long, so they can be avoided when the functioning of this wattmeter designed for measuring periodic variables is considered.

III RESULTS OF MEASURING IN REAL ENVIRONMENT

The suggested concept for measuring RMS values of current, voltage and power can be classified as a synchronous method. The required synchronization is obtained by software measurements of the frequency of the measuring signal and generation of a sampling signal using a microprocessor. A null detector is connected to one input of the micro-controller and the frequency of the input signal is measured. All this is performed using counting resources of the micro-controller. The micro-controller generates sampling intervals and based on sampling values of the measured signal calculates the mean power or RMS value. An accuracy of 0.01% was reached for the measured range (0-1 kHz) in relation to the measured output value (table 1).

Analyses with described comparator, which was carried out to detect zero crossing, gave satisfactory accuracy when measuring in electric utilities. Even more accurate detection can be achieved in this procedure by introducing algorithm given in papers [7, 8]. A number of undesirable effects such as the spectral leakage associated with the discrete Fourier transform (DFT), and the truncation errors in digital wattmeter's arise and degrade system performance. The basic idea of the proposed method [7] is to modify the actual sampled sequence such that it becomes an ideal sample sequence, which is synchronized with the signal subjected to sampling. A simple algorithm for modifying the sampled sequence on-line is derived based on interpolation. The proposed approach requires quite modest additional computational burden, which makes it suitable for real-time signal processing. Results [7], show that the proposed algorithm is capable of reducing both the leakage effect in DFT analysis and truncation errors in digital wattmeter's. In paper [8] describes a digital null detector which is able to detect sinusoidal signal in presence of correlated noise, which is based on the implementation of nonlinear algorithm. It is shown that the apparatus is suitable for separating the glitch pulses in a measuring system

A measuring board was specially designed for measuring voltage and current (and thus active power) in an electric power system with the purpose of testing the suggested concept of measuring active power based on the use of slow, but very precise dual slope A/D converters. The experimental board contains fast, very precise sigma-delta ADC. The block scheme of the suggested model is given in Fig. 1.

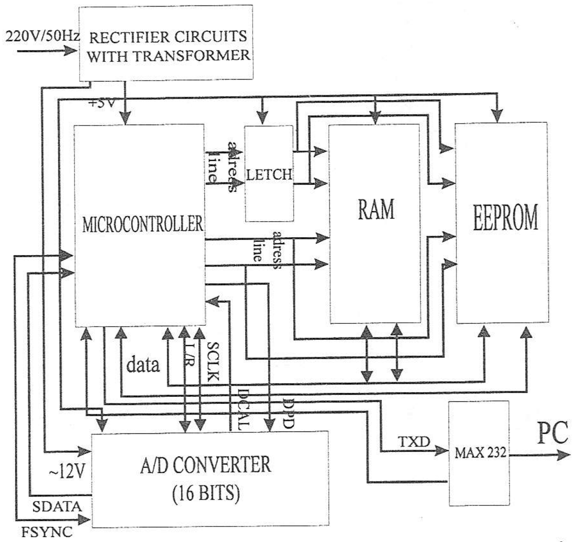

Fig.1. *Block scheme of the suggested model*

The basic board contains a 16-bit sigma-delta A/D converter. It enables sampling, analog-to-digital conversion and anti-aliasing, generating 16 bit values in a serial form for both right and left input signals. Words can appear at the output with a speed higher than 50 kHz per channel.

At the given sampling frequency, samples are taken every 86 ms and are proceeded in series form to the microcontroller, which collects them and stores 16-bite data into external RAM. That microcontroller works by the program, which is stored in EEPROM. After collecting 896 samples, microcontroller informs superior PC that is able to perform necessary calculations.

As this converter is primarily used for measuring continual signals in real conditions (as in electric utilities) it certainly cannot provide the required 16-bit accuracy. One can expect an accuracy of 14 bit (perhaps only 12 bits) due to reasons that will be further described.

The deviation of the effective voltage value from period to period was tested experimentally with the purpose of estimating voltage variation and also the values of active power which were calculated for several different samples (i.e. periods of input alternating voltage). Such measurements can confirm inertia of the electric power system which is by nature very slow (it is well known that in our system the hydroelectric power stations (hydroelectric plants) Djerdap and Bajina Basta have the fastest response and they need at least 15 minutes to change their working regime, so it is clear what type of system is analyzed).

The results obtained by measuring the RMS value of voltage from period to period are given in table 1. It should be mentioned that data from two consecutive periods of input voltage are stored in the internal RAM of the experimental board and then the collected data set is transferred using a serial connection to a PC. Communication between the experimental board and the PC is controlled by a micro-controller (68HC11, MOTOROLA).

A low pass filter with band frequency of 450-500Hz was added to the already developed board for measuring RMS values of system voltage to increase the measuring accuracy by the noise attenuation. The filters active and was checked using the SPICE programming packet before installation. Measurements were performed using 40 consecutive periods of system voltage.

Table 1. *Results obtained by measuring the RMS value of network voltage*

Period	Measured RMS value V_{RMS}	Period	Measured RMS value V_{RMS}	Period	Measured RMS value V_{RMS}	Period	Measured RMS value V_{RMS}
1	208,137987	11	208,158745	21	208,139998	31	208,153442
2	208,138487	12	208,158744	22	208,140087	32	208,154432
3	208,142232	13	208,150076	23	208,140004	33	208,150078
4	208,143454	14	208,148988	24	208,142377	34	208,152300
5	208,123884	15	208,148876	25	208,144221	35	208,150234
6	208,134556	16	208,147688	26	208,145987	36	208,151288
7	208,144621	17	208,148756	27	208,149856	37	208,149888
8	208,150003	18	208,143326	28	208,147632	38	208,151117
9	208,149987	19	208,143124	29	208,149003	39	208,152134
10	208,152134	20	208,147844	30	208,152315	40	208,152366

Analysis of obtained results shows that the largest variation during data collection is 0.01%, so the observed system justifiable be considered inertial. For this reason the suggested measuring concept using slow A/D converters enables the development of very precise instruments.

Further investigation of electric utilities stability was established in laboratory for electroenergy systems on Faculty of Electrical Engineering Belgrade, because they poses adequate equipment for necessary measurements. We take down shape of net current using current transformer, some as we plan to install on final instrument. Results of measuring over special (very precise and accurate) akvization board we transferred to a PC for further calculation. We can espy that exits high DC component by reason of inaccuracy of akvization board. However, generally we can clearly see that shape of measured current signal not alter very much in observed interval of the time. The results obtained by this measuring of current are given in Fig.2.

In order to test accuracy of developed measuring system, parallel measuring with extremely precise multimeter HP 3475A, Hewlett Packard. HP 3457 by yours construction give results processed on more period of observed net voltage. This is the reason why we can't divide results of measurements on only one period as we can with results obtained using experimental board with 16-bits ADC. In observed interval of time, this instrument shows 208,149V as RMS value of net voltage, and they shoved the same results as in above table, up to the third decimal. All this gave us the right to use the suggested measuring concept at extremely precise reference and laboratory measuring.

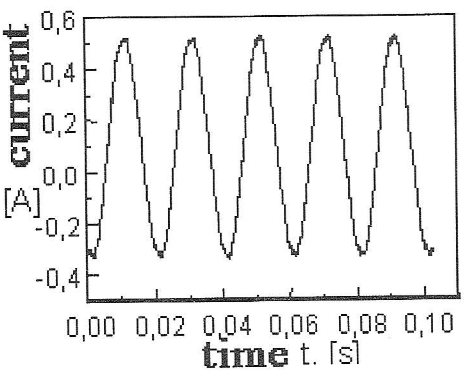

Fig.2: *Time diagram of net current, measuring using current transformer*

In order to satisfied (1) and (2), and after some mathematical manipulation we can define the number of harmonics [12], needed for accurate processing of average power according to suggested algorithm, as well as the number of samples, both of voltage and current, needed to satisfy equality of (1) and (2).

Measurements in Yugoslavia electric utilities during few minutes showed no significant changes in the value of processed signal. Analyses described in this paper show that required inertia of the system could be limited at 1 minute only.

Presented processing demands can be satisfied using a great range of low cost microprocessors. They are also capable of carrying out DFT to detect harmonic content of an input signal automatically adjusting the algorithm to the real conditions in electric utilities.

In above discussion we confirmed stationarity of the observed system, and finally we approached to realization of the real instrument. After being adjusted to measuring range of a converter, both a voltage and current signals are brought onto the dual slope A/D converter with two channels. The voltage signal has been adopted over precise resistance network. The current signal over accurate current transformer has been taken to one of the inputs of 16-bits dual slope A/D converter. A special circuit detects passing of the signal through zero with a comparator, in this way achieving synchronization of measuring cycle with electric utility frequency. The microcontroller generates sampling intervals and based on sampling values of measured signals is able to perform necessary calculations. Complete control of measuring process and all necessary calculations are done by microcontroller (PIC 16C74). The PIC 16C74 is low-cost, high-performance, RISC microcontroller. Installed keyboard, which is used to set up measuring range and start of measuring, is not presented in the Fig. 1. This watthourmeter can also be used for measuring of RMS values of voltage and current, as well as average and reactive power.

IV CONCLUSION

A new design of a digital measuring system for measuring basic parameters of electric utilities (voltage, current, power, energy, and frequency...) has been described. The proposed algorithm is suitable for on-line measurements and is characterized by a low computational burden, in comparison with described algorithms in [2, 6]. Voltage measurements on the system show that it is inertial, so the error made when sampling during several periods (rather than in one period) is below the value required for class 0.1 instruments. A dual slope A/D converter meets all price and accuracy requirements of the design of the measuring system. This gives an opportunity for developing a measuring system with very simple and cheap hardware, contrary to highly sophisticated and expensive hardware described in [5]. The necessary synchronization is reached by software measurements of the frequency of the measured signal. Algorithm is of an adaptable type and depends on harmonic content of the input signal and network frequency (50 or 60Hz). An accuracy of 0.01% was attained in relation to the measured output value.

V REFERENCE

[1]. R.S. Turgel, "Digital wattmeter using a sampling method", IEEE Trans. on I&M, Vol. IM-23, pp. 337-341, December 1974.

[2]. Marganitz, A., "Power Measurement of Periodic Current and Voltage by Digital Signal Processing", European Trans. on Electrical Power Engineering, Vol. 2, No. 2, March/April 1992, pp. 117-123.

[3]. Srinivasan, K., "Errors in Digital Measurement of Voltage, Active and Reactive Powers and an On-Line Correction for Frequency Drift", IEEE Trans. Power Delivery, Vol. PWRD-2, No. 1, Jan. 1987, pp. 72-75.

[4]. G.S. Hope, O.P. Malik, J. Chang, "Microprocessor-based active and reactive power measurement" Journal of Electric Power and Energy Systems, Vol. 3, No. 2, pp. 75-83, April 1981.

[5]. L. Toivonen, J. Morsky, "Digital Multirate Algorithms for Measurement of Voltage, Current, Power and Flicker", IEEE Trans. on Power Delivery, Vol. 10, No. 1, January 1995.

[6]. M. Kezunovic, E. Soljanin, B. Perunicic, S. Levi, "New approach to the design of digital algorithms for Electric Power Measurements", IEEE Trans. on Power Delivery, Vol.6, No. 2, pp. 516-523, April 1991.

[7]. J.Xi and J.F.Chicharo, "A New Algorithm for Improving the Accuracy of Periodic Signal Analysis", IEEE Trans. on I&M, Vol.45, pp.827-831, August 1996.

[8]. D. Tarach, G. Trenkler, "A Noise-Adaptive Digital Null Detector", IEEE Transactions on Instrumentation and Measurement, Vol. 46, No. 2, pp.435-438, April 1997.

[9]. P. Petrovic, S. Marjanovic, "SIMULATION OF REAL ELECTRIC UTILITIES AND MEASURING ITS BASIC PARAMETERS USING SLOW A/D CONVERTERS", International Conference on Systems, Signals, Control, Computers SSCC'98, Vol.III, pp.291-295, ISBN -620-23136-X, 22-24 September 1998, Durban, South Africa.

[10]. P. Petrovic, "ONE SOLUTION OF THE ANALOGUE-DIGITAL CONVERSION IN INDUSTRIAL ENVIRONMENT", VI International SAUM Conference on Systems Automatic Control and Measurements SAUM'98, Vol.I, pp.74-77, September 28-30, Ni{, Yugoslavia.

[11]. P.Petrovic, S. Marjanovic, M. Stevanovic,"Measuring Active Power, Voltage and Current Using Slow A/D Converters", 15th Annual IEEE Instrumentation and Measurement Technology Conference, Volume II, pp.732-737, St. Paul, Minnesota, USA, 18-21 May 1998.

[12]. P. Petrovic, S. Marjanovic, M. Stevanovic, "A DIGITAL METHOD FOR POWER FREQUENCY MEASUREMENT USING SYNCHRONOUS SAMPLING", IEE Proceedings, Electric Power Applications, (prihva}en rad za julsku publikaciju 1999).

INSTRUCTION FOR AUTHORS

Name of the author

In the review "Electronics", we publish the scientific and professional works from different fields of electronics in the broadest sense like: automatics, telecommunications, computer techniques, energetic, nuclear and medical electronics, analysis and synthesis of electronic circuits and systems, new technologies and materials in electronics etc. In addition to the scientific, reviewal and professional works, we present new products, new books, M. A. and D. Sc. theses.

In order to enable the unification of the technical arrangement of the works, to simplify the printing of the review "ELECTRONICS", we are giving this instruction for the authors of the works to be published in this professional paper.

The works are to be delivered to the editor of the review by the E-mail (elektronika@etf-bl.rstel.net) or to the address of the Electrical Engineering Faculty (Elektrotehnicki fakultet, Patre5, 78000 Banja Luka) on a floppy and printed in three folds.

All of the three folds are to be printed on one side of the paper A4 format, 210x297 mm, i.e., 8.27" width and 11.69" height, upper and lower margins of 1", left and right margins of 1" and the header and footer are 0,5". The work has to be written in English language. Our suggestion to the authors is to make their works on a PC using the word processor WORD FOR WINDOWS, and for the figures to use the graphic program CORELDRAW. The graphs are going from the original programs, i.e., from the programs received. The works should not be finished at the beginning of a page. If the last manuscript page is not full, the columns on that page should be made even.

The title of the work shall be written on the first page, in bold and 12 pts size. Also, on the first page, moved for one line spacing from title, the author's name together with the name of his institution shall be printed in the letter size of the remaining parts of the text. The remaining parts of the manuscript shall be done in two columns with 0.5" interspace. The work shall be typed with line spacing 1 (Single) and size not less than 10 pts. After the title of the work and the name of the author, a short content in English language follows, written in italics. The subtitles in the text shall be written in bold, capital letters of the size as in the text (not less than 10 pts). Each work shall, at the beginning, comprise a subtitle INTRODUCTION, and, at the end, the subtitles CONCLUSION and BIBLIOGRAPHY. At the end of the work, there shall be a short abstract and the title in English accompanied with the names of authors.

The operators and size marks that do not use numerical values, shall be written in common letters. The size marks that can use numerical values shall be written in italics. The equations shall be written in one column with right edge numeration. If the breaking of equations or figures is not desired, those may be placed over both columns.

Illustrations (tables, figures, graphs etc.) may be wider than one column if necessary. Above a table there shall be a title for instance: Table 2. *The experimental measuring results.* The same applies to figures and graphs but the accompanying text comes underneath the figure of graphs.

At the end of each work, the used literature shall be listed in order as used in the text. The literature in the text, shall be enclosed in square brackets, for instance: ...in [2] shown is...

ELECTRONICS

VOL. 3, NO. 1, NOVEMBER 2000.